



THE HONG KONG
POLYTECHNIC UNIVERSITY

香港理工大學

Pao Yue-kong Library

包玉剛圖書館

Copyright Undertaking

This thesis is protected by copyright, with all rights reserved.

By reading and using the thesis, the reader understands and agrees to the following terms:

1. The reader will abide by the rules and legal ordinances governing copyright regarding the use of the thesis.
2. The reader will use the thesis for the purpose of research or private study only and not for distribution or further reproduction or any other purpose.
3. The reader agrees to indemnify and hold the University harmless from and against any loss, damage, cost, liability or expenses arising from copyright infringement or unauthorized usage.

IMPORTANT

If you have reasons to believe that any materials in this thesis are deemed not suitable to be distributed in this form, or a copyright owner having difficulty with the material being included in our database, please contact lbsys@polyu.edu.hk providing details. The Library will look into your claim and consider taking remedial action upon receipt of the written requests.

NUMERICAL AND EXPERIMENTAL
STUDY OF DUCTED TURBINES IN
BI-DIRECTIONAL TIDAL FLOWS

MADUKA MADUKA
PhD

The Hong Kong Polytechnic University
2022

The Hong Kong Polytechnic University
Department of Civil and Environmental Engineering

Numerical and Experimental Study of Ducted Turbines in Bi-Directional Tidal Flows

Maduka Maduka

A thesis submitted in partial fulfilment of the requirements for the
degree of Doctor of Philosophy

May 2021

Certificate of Originality

I hereby declare that this thesis is my work and that, to the best of my knowledge and belief, it reproduces no material previously published or written, nor material that has been accepted for the award of any other degree or diploma, except where due acknowledgement has been made in the text.

MADUKA Maduka

Dedication

I would like to dedicate this PhD thesis to my beloved father, Mr. Maduka Alugwo and mother, Mrs. Maduka Joy.

Abstract

Installing a turbine in a duct generally will increase the flow through the rotor. If there is flow confinement due to limited water depth, the presence of lateral boundaries, or the presence of adjacent turbines, a further flow enhancement through the rotor will be achieved. It appears there are no or limited studies on ducted turbines in a tidal farm. In recent times, a duct equipped with a flange (referred to as a wind-lens) has attracted extensive attention. Unlike the traditional early designs of ducted turbines that rely on increasing the area ratio between the inlet and duct exit diameters, it depends on creating a low backpressure region through a strong vortex formation behind its broad flange and hence, a substantial increase in the wind speed. Although wind-lens has demonstrated significant power augmentation, a vast majority of investigations on wind-lens designs are mainly based on several existing typical shapes. Therefore, the wind-lens design is still far from optimal. In addition, the power performance of ducted turbines in a tidal farm, as well as the interaction effects between adjacent ducted turbines, have not been investigated in detail before.

The present study carried out a thorough analysis of the hydrodynamics of different flanged duct shapes (symmetric and asymmetric) for both uni-directional flow and bi-directional flows and hence proposed an optimum wind-lens design. The analysis was performed using data obtained from numerical and experimental modelling of flanged duct tidal turbines which were isolated or within an array. The numerical assessment employed an actuator disk representation of the rotor that provides an axial resistance to the flow, and thus models the extraction of linear momentum. And based on the proposed optimum flanged duct type (i.e., duct Type C) obtained from the numerical simulation, physical experiments were carried out in an open-channel recirculating water flume with a 1:200th scaled flanged duct tidal stream model representing a turbine of diameter 20m in a water depth of 44.4m. Raw data sets were obtained using a Prony brake and a side-looking ADV. Analysis was presented in terms of power performance, wake velocity ratios and turbulence intensities. Conclusions were drawn from the comparisons of the power performance and interaction effects between flanged duct tidal turbines or the bare (non-duct) turbine in isolation or an array.

The numerical results showed that a flanged duct turbine with an inlet-arc flap and a curved flange can achieve a maximum value of C_p^* (duct area-based power coefficient) close to the Betz-

Joukowski limit (BJL) for flow from either direction while the symmetric duct turbine showed a maximum C_p^* of about 60% of the BJL. The effect of flow confinement on C_p^* showed C_p^* increases with blockage ratio, ϵ and the ratio of the peak power coefficient of ducted turbine over the peak power coefficient of bare turbine varies slightly with the blockage ratio.

The experimental results showed that ducted turbines generate higher power per rotor unit area instead of duct area. The power coefficient obtained for the flanged duct turbines was within the range of a 200 kW OpenHydro demonstrator device i.e., about 0.3 with a 2.5m/s rated flow speed. Results were qualitatively similar to the numerical results. The results further revealed that a second turbine axially installed 10 rotor diameters from an upstream turbine underperformed for each of the individual devices. A reduction of about 20% for the bare turbine and about 25% for the ducted turbines compared to the corresponding upstream turbine. The ducted turbines still performed better than the bare turbine in terms of the peak power coefficient. The power reduction implies that the performance of the second turbine mainly depends on the axial distance between the turbines for the in-line configuration considered. Therefore, power reduction in this region can be improved if the turbines are placed apart such that they are minimally affected by the wakes from the turbines directly upstream.

For all devices, the experimental investigation showed that the velocity of incoming flow decreases while the corresponding streamwise turbulence intensity increases as the flow passes through the turbine. The decreasing range of wake velocities and the increasing range of turbulence intensities were both the largest for the ducted turbines and the lowest for the bare turbine. However, all devices showed monotonically increasing and decreasing trends for the variations of wake velocities and turbulence intensities with increasing axial distance. Across the axial distance downstream, the bare turbine absorbed lesser energy from flow and exerted smaller effects on its wake than the ducted turbines.

For all devices, the wake gradually recovered up until the recovery of flow was detected at about 13 and 20 rotor diameters downstream for bare and ducted turbines respectively. The turbulence intensities at those respective axial distances were slightly smaller than that at the inflow boundary. This finding is comparable to previous studies that downstream spacing could be in the order of 15-20 rotor diameters. The velocity ratio profile in the bare rotor wake compared well with published data from a recirculating water flume/channel and the spread in data was

identified to be due to the differences in the range of turbulence intensities, blockage ratio (thus, variations in the thrust) and turbine model.

For the two in-line turbines, the downstream bare turbine recovered faster than the downstream ducted turbines. At 24 rotor diameters downstream and beyond, the velocity ratio of the downstream bare turbine was very close to that of the isolated one (correspondingly at 15 rotor diameters downstream and beyond). At these distances, the second downstream turbine operated as if it was in isolation. For the ducted turbines, unlike in the isolated case, the wake flow ratio persisted beyond 30 rotor diameters downstream for the two ducted turbine arrangements with the turbulence intensity slightly less than the upstream conditions. However, the peak power coefficients of the downstream ducted turbines were still higher than that of the downstream bare turbine. Therefore, the deployment of additional ducted turbines in a tidal farm may have an advantage. Although, the precise economic estimates of energy cost are unavailable at the present state of development.

The originality of this study is that it is the first to experimentally explore duct performance and far wake characteristics of flanged duct turbines with the in-line arrangement, and with the optimal shape of the duct determined by numerical simulations. Thus, this study has provided a comprehensive set of experimental data to the research community that will guide the course of future marine current turbine research and for validating theoretical and numerical methods. It is envisioned that the efficient and cost-effective deployment of full-scale tidal farms solely depends on the progress in finding optimum duct shape (or size), blade design, and turbine array layout.

List of Publications

Maduka, M., & Li, C. W. (2021). Numerical study of ducted turbines in bi-directional tidal flows. *Engineering Applications of Computational Fluid Mechanics*, 15(1), 194-209. <https://doi.org/10.1080/19942060.2021.1872706>

Maduka, M., & Li, C. W. (2021). Experimental Evaluation of Power Performance and Wake Characteristics of Twin Flanged Duct Turbines in Tandem under Bi-directional Tidal Flows. (under review in *Applied Energy*).

Maduka, M., Adewole, M. O., & Li, C. W. Analytical and Empirical Analysis of Ducted Turbine in a Tidal Channel. (in preparation).

Acknowledgements

Just as one's life is influenced by others, most times by our parents, one's professional life can be influenced by certain individuals. In some cases, the influence can be profound, so I am deeply grateful to my supervisor, Prof. C.W. Li, for his influence on my professional career so far, unreserved support and technical guidance throughout this work. More so, to the Hydraulic laboratory technician, Mr. Leung Kwok-hing, I am indebted to you for your profound technical support in this project and otherwise.

I would like to thank all my professors and non-academic staff at CEE, The Hong Kong Polytechnic University for their teachings and support during my PhD.

More so, this project was not performed in isolation. Thanks are due to the following people for their help and advice: My parents, Mr./Mrs. Maduka Alugwo, my siblings – Mr. Maduka Augustine, Mrs. Maduka Ngozi, Mr. Maduka Ifeanyi and Mr. Maduka Stephen and my friends – Dr Matthew Adewole, Dr Eze Chika, Dr Tony-Chuan Che, Mr. Udoka Nwakwo, Mr. Anosike Abuchi, and Ms. Fung Nim Yu.

Table of Contents

Certificate of Originality.....	i
Dedication.....	ii
Abstract.....	iii
List of Publications.....	vi
Acknowledgements.....	vii
Table of Contents.....	viii
List of Figures.....	xiii
List of Tables.....	xvi
List of Abbreviations.....	xvii
CHAPTER ONE.....	1
Introduction.....	1
1.1 Background.....	1
1.2 Tidal Turbine Concepts.....	4
1.2.1 Extraction Methods.....	4
1.2.2 Tidal Stream Generation.....	5
1.3 Thesis Objectives and Scope.....	8

1.4	Significance and Value of the Study	9
1.5	Thesis Outline	10
1.6	Chapter Summary.....	11
CHAPTER TWO		12
Literature Review.....		12
2.1	Ducted Turbines	12
2.2	Diffuser Augmentation Mechanism	13
2.3	Industrial Ducted Tidal Turbines	14
2.3.1	<i>Rotech Tidal Turbine (RTT)</i>	15
2.3.2	<i>Solon Tidal Turbine</i>	15
2.3.3	<i>Open-Center Tidal Turbine</i>	16
2.3.4	<i>Clean Current Tidal Turbine</i>	17
2.3.5	<i>Hydro Helix Tidal Turbine</i>	17
2.3.6	<i>SeaUrchin Vortex Reaction Turbine</i>	18
2.3.7	<i>MEGAWATTBlue</i>	19
2.3.8	<i>Underwater Electric Kite</i>	19
2.4	Research Studies on Ducted Turbine	21
2.4.1	<i>Analytical Framework</i>	21
2.4.2	<i>Analyses of Diffuser Augmented Wind Turbines</i>	22
2.4.3	<i>Analyses of Diffuser Augmented Tidal Turbines</i>	24
2.5	Chapter Summary.....	32

CHAPTER THREE	35
Numerical Method	35
3.1 Numerical Approach	35
3.1.1 <i>Governing Equations</i>	35
3.1.2 <i>Actuator Disk Model</i>	36
3.1.3 <i>CFD Software</i>	40
3.1.4 <i>Turbulence Modelling</i>	41
3.1.4.1 <i>URANS Model with $k - \omega$ SST Turbulence Closure</i>	46
3.1.5 <i>Open Channel Flow</i>	48
3.1.6 <i>Modelling Free Surface Effect for Tidal Turbines</i>	49
3.2 Chapter Summary.....	50
CHAPTER FOUR.....	52
Numerical Results and Discussion.....	52
4.1 Simulation Domain and Boundary Conditions	52
4.2 Actuator Disk Implementation and Model Set-up	54
4.3 Choice of Duct Shapes	56
4.4 Mesh Definition and Grid Convergences.....	57
4.5 Initial Validation Studies.....	59
4.6 Numerical Analyses	61
4.7 Performance of Ducted Turbines with Ideal Rotor	61

4.7.1	<i>Performance of Turbines with Equal Frontal Area</i>	62
4.7.2	<i>Performance of Turbines with Equal Rotor Area</i>	64
4.8	Flow Field Distributions of Turbines	65
4.9	Effect of Blockage Ratio	69
CHAPTER FIVE		72
Experimental Method.....		72
5.1	Experimental Approach.....	72
5.1.1	<i>Model Design</i>	73
5.1.1.1	<i>Blade Section Details</i>	73
5.1.1.2	<i>Duct Design</i>	77
5.1.2	<i>Test Facility</i>	78
5.1.2.1	<i>Hydrodynamic Performance</i>	80
5.1.2.2	<i>Flow Velocity Measurement</i>	82
5.1.2.3	<i>Limitations of Scaled Model Testing and Measurement Uncertainty</i>	84
5.1.3	<i>Turbine Layout Configurations</i>	88
5.1.3.1	<i>Single Row of Turbines</i>	88
5.1.3.2	<i>Two-inline Turbines</i>	91
5.2	Chapter Summary.....	92
CHAPTER SIX.....		94
Experimental Results and Discussion.....		94
6.1	Experimental Analyses.....	94

6.2	Performances of Ducted Turbines with Real Rotors.....	95
6.2.1	<i>Performances of Isolated Turbines in Single Row Arrangement.....</i>	<i>95</i>
6.2.2	<i>Performances of Downstream Turbines in Two-axially-aligned Turbine Arrangement.....</i>	<i>99</i>
6.3	Wake Field Analyses.....	101
6.3.1	<i>Wake Characteristics of Isolated Turbines</i>	<i>101</i>
6.3.2	<i>Wake Characteristics for Two In-line Turbines</i>	<i>108</i>
CHAPTER SEVEN		115
Conclusions and Future Work		115
7.1	Conclusions	115
7.2	Recommendations for Future Study.....	120
7.3	Contributions of Thesis	121
References.....		123

List of Figures

Figure 1.1. Global greenhouse emission by gas (IPCC, 2014).....	2
Figure 1.2. Global greenhouse emission by economic sector (IPCC, 2014).	2
Figure 1.3. 2016 world gross electricity production by source (IEA, 2018).	3
Figure 1.4. Tidal turbine configurations (a) vertical crossflow turbine (b) horizontal axial- flow turbine (c) oscillating hydrofoil (Entec UK Ltd, 2007).	6
Figure 1.5. R&D effort for tidal technologies tested at full-scale (Magagna et al., 2016).	7
Figure 1.6. Overall flowchart of the thesis.	11
Figure 2.1. (a) Traditional wind energy extraction process (b) diffuser augmentation wind energy extraction process (Van Bussel, 1998).....	13
Figure 2.2. Rotech Tidal Turbine (Lunar Energy Tidal Power, 2006).	15
Figure 2.3. Solon Tidal Turbine (Atlantis Resources Corporation, 2018).....	16
Figure 2.4. Open-center Tidal Turbine (OpenHydro Ltd, 2018).	17
Figure 2.5. Clean Current Tidal Turbine (Clean Current Power Systems Incorporation, 2013)..	17
Figure 2.6. Hydro Helix Tidal Turbine (HydroHelix Energies, 2014).	18
Figure 2.7. SeaUrchin Vortex Reaction Turbine (Elemental Energy Technologies, 2017).	18
Figure 2.8. MEGAWATTBlue (Guinard Energies, 2017).	19
Figure 2.9. Underwater Electric Kite (UEK Corporation, 2014).....	19
Figure 2.11. Schematic cross-sectional view of increasing wind flow speed mechanism around a	

flanged diffuser (Ohya et al., 2008).....	24
Figure 2.12. Velocity profile in the wake of a wind turbine (Sanderse, 2009).....	28
Figure 3.1. The Actuator Disk Model within a streamtube.	37
Figure 3.2. Theoretical plot of C_t and C_P against a	39
Figure 3.3. Overview of OpenFOAM structure (Greenshields & OpenFOAM, 2016).....	41
Figure 4.1. Computational conditions and boundary conditions.	53
Figure 4.2. Blockage ratio, ϵ definition for (a) bare (b) ducted turbines.	54
Figure 4.4. Typical grid layout (a) around the duct and turbine (b) before and beyond the duct and turbine.	58
Figure 4.5. Sensitivity of C_p with grid size.	59
Figure 4.6. Effect of freestream turbulence on C_p with (a) a (b) C_t for a bare turbine with $\epsilon = 0.108$	59
Figure 4.7. Axial distributions of streamwise velocity ratio (a) $C_t = 0.2$ (b) $C_t = 0.9$ and pressure coefficient (c) $C_t = 0.2$ (d) $C_t = 0.9$	60
Figure 4.8. Variation of $C_P *$ with (a) a (b) C_t (C_t ranges from 0 to 2).	63
Figure 4.9. Variation of C_p with (a) a (b) C_t (C_t ranges from 0 to 2).	65
Figure 4.10. Flow streamlines for (a) Bare (b) Type A (c) Type B (d) Type C (e) Type C Reversed (f) Type D. Flow direction is from left to right.	66
Figure 4.11. Pressure fields for (a) Bare (b) Type A (c) Type B (d) Type C (e) Type C Reversed (f) Type D. Flow direction is from left to right.	68
Figure 4.12. Axial distributions of streamwise (a) velocity ratio (b) pressure coefficient for bare and Type C ducted turbine.	69

Figure 4.13. Variation of CP^* with blockage ratio for bare, Type C, and Type D turbines.....	70
Figure 5.1. Cross-section of NACA 4412 airfoil.....	73
Figure 5.2. C_l and C_d vs AoA plots for NACA 4412 at $Re = 1 \times 10^6$	75
Figure 5.3. The sketch of blade and rotor (measurement is shown in m).	76
Figure 5.4. Typical blade (a) profile sections (b) twist along the blade span.	77
Figure 6.2. Centerline velocity distribution.	96
Figure 6.13. Streamwise vertical and lateral profiles (a) velocity ratio (b) turbulence intensity downstream of the second turbine at $x = 20Dt - 30Dt$	114

List of Tables

Table 2.1. Summary of ducted tidal turbines from developers.....	20
Table 2.2. Maximum values of C_p and CP^* for various ducted turbines.....	26
Table 4.1. Details of numerical simulation.....	54
Table 4.2. Grid convergence tests for Type C ducted turbine (with $C_t = 1.05, L = 0.25Dt, h = 0.1125Dt, f = 0.05Dt, S = 0.125Dt$ & $\epsilon = 0.131$).....	58
Table 5.1. Geometric distribution of the base design blade sections.....	77

List of Abbreviations

a	Induction factor [–]
A	Rotor area [m^2]
A_c	Channel cross-sectional area [m^2]
A_{duct}	The total projected frontal area of the duct device [m^2]
AoA	Angle of attack [°]
BJL	Betz- Joukowsky Limit [–]
c	Chord length [m]
COR	Correlation coefficient [–]
C_d	Drag coefficient [–]
$CD_{k\omega}$	The positive portion of the cross-diffusion term [–]
C_l	Lift coefficient [–]
C_p	Power coefficient normalized with A [–]
$C_{p_{max}}^{single}, C_{p_{max}}$	Maximum power coefficient normalized with A for the single row turbine [–]
C_p^{down}	Power coefficient normalized with A for downstream turbine [–]
C_p^*	Power coefficient normalized with A_{ref} [–]
C_{ps}	Pressure coefficient [–]
C_t	Rotor thrust coefficient/loading coefficient/pressure coefficient [–]
D_t	Turbine rotor diameter [m]
f	Arc-flap inlet length [m]
$f_{M,i}$	momentum source in the $i - th$ direction [N]
f_q	Frequency [Hz]
F_r	Froude number [–]
F_1, F_2	Blending functions accounting for switch formulation of the SST model between $k - \omega$ and $k - \varepsilon$ at the wall [–]
F_3	Blending function accounting for roughness layer in rough wall flows [–]
g	Acceleration due to gravity [m/s^2]
h	Flange height [m]
h_f	Arc-flap inlet height [m]
h_0	Static head [m]

H	Total head [m]
I	Turbulence intensity [%]
I_x	Longitudinal turbulence intensity [%]
k	Turbulence specific kinetic energy [m^2/s^2]
l	Turbulent length scale [m]
L	Duct/diffuser length [m]
L	Characteristic length of the flow [m]
\dot{m}	Mass flow rate [Kg/s]
m_w	Attached weight at one end of the rope [Kg]
m_s	Counterweight attached to a spring balance [Kg]
n	Number of blades [–]
N	Number of recorded velocity samples [–]
p	Pressure [Pa]
\bar{p}_t	Mean pressure [Pa]
\bar{p}'_t	Mean pressure fluctuating component [Pa]
p_0	Reference pressure of the approaching flow [Pa]
P	Produced power [W]
P_E	Extracted power [W]
P_k	Production term in k [m^2/s^2]
P_ω	Production term in ω [s^{-1}]
R	Duct radius [m]
r	Rotor radius [m]
r_d	Rim radius [m]
r_h	Blade height [m]
Re	Reynolds number [–]
S	Duct exit expanding length [m]
S	Invariant measure of the strain rate [s^{-1}]
SNR	Signal to noise ratio [–]
\bar{S}_{ij}	Mean rate of the strain tensor [s^{-1}]
T	Thrust force [N]
t	Time [s]
t	Duct thickness [m]

TSR	Tip-speed-ratio [–]
$TSR_{max}^{single}, TSR_{max}$	Maximum tip-speed-ratio for the single row turbine [–]
TSR^{down}	Tip-speed-ratio of downstream turbine [–]
u	Axial streamwise velocity [m/s]
\bar{u}_i	Mean velocity [m/s]
\bar{u}'_i	Mean velocity fluctuating component [m/s]
$\overline{u'_i u'_j}$	Reynolds stress tensor [m^2/s^2]
u_x	Mean longitudinal velocity [m/s]
u_τ	Friction velocity [m/s]
X	Axial distance [m]
Y	Lateral distance [m]
y_w	Normal distance to the wall [m]
y_w^+	Dimensionless wall distance [–]
Z	Vertical distance [m]
ε	Dissipation rate of the turbulent kinetic energy [m^2/s^3]
ϵ	Blockage ratio [–]
μ	Dynamic viscosity [$Kg/m.s$]
η	Efficiency [–]
Δ	Relates to change [–]
δ_{ij}	Kronecker delta [–]
ν	Kinematic viscosity [m^2]
ν_t	Turbulence viscosity [m^2/s]
ρ	Fluid density [kg/m^2]
σ	Solidity [–]
θ	Duct inlet angle [$^\circ$]
Ω	Rotor angular speed [$rads^{-1}$]
ω	Turbulence specific dissipation rate [s^{-1}]

Subscripts

max	Maximum
i, j	Spatial dimension
x, y, z	Instream, cross-stream and vertical cartesian directions

0	Relates to the flow far upstream of the rotor/disk
2	Upstream of the rotor/disk
3	Downstream just after the rotor/disk
4	Far downstream of the rotor/disk

Acronyms

1D	One-dimensional
2D	Two-dimensional
3D	Three-dimensional
ABL	Atmospheric boundary layer
ADV	Acoustic Doppler Velocimeter
BEM	Blade Element Momentum
CECEP	China Energy Conservation and Environmental Protection
CFD	Computational fluid dynamics
DES	Detached Eddy Simulation
EMEC	European Marine Energy Center
FST	Freestream turbulence
GHG	Greenhouse gas
IEA	International Energy Agency
LDV	Laser Doppler Velocimeter
LES	Large Eddy Simulation
MCT	Marine current turbine
n.a	Not applicable
NACA	National Advisory Committee for Aeronautics
NDC	Nationally determined contribution
OpenFOAM	Open-source Field Operation and Manipulation
PIV	Particle-Image-Velocimetry
<i>SST</i>	Shear-stress transport
URANS	Unsteady Reynolds-average Navier-Stokes
Vs	versus

CHAPTER ONE

Introduction

This chapter gives an insight into the purpose of undergoing this research by presenting the background of this study, existing tidal turbine concepts, significance, and values of this study alongside the research objectives and scope. Also presented is the outline of the flow structure of the thesis followed by a summary of the keynotes of this chapter.

1.1 Background

Humanity and its environment are endangered by extreme weather events such as droughts, typhoons, and hurricanes, resulting from rapidly changing climatic conditions. These drastic changes in climatic conditions are because of man-made influences leading to an increase in the level of emissions of greenhouse gas (GHG) such as carbon dioxide, methane, and nitrogen oxides.

In 2015, a landmark agreement was reached among 194 countries in Paris on efforts to combat climate change. The agreement aims to provide finance, technology, and capacity-building support to all parties. It also proscribed that parties shall submit periodic updates of their nationally determined contribution (NDC) to know their progress and support needs and future plans. Although to this date, only 189 parties have ratified this convention (UNFCCC, 2020). Among the GHGs, CO₂ has the largest global portion of contributions to the greenhouse effect with 65 per cent originating from fossil fuel and industrial processes as seen in Figure 1.1 and one of the main targets of the Paris agreement is long-term CO₂ emission reduction. Figures 1.1 and 1.2 show GHG emissions by gas and economic sector based on global emissions from 2010 respectively.

The electricity and heat production sector represents the largest sole source contributor to GHG emissions contributing to about one-quarter of the global GHG emissions (Figure 1.2) and primarily involves the burning of fossil fuels.

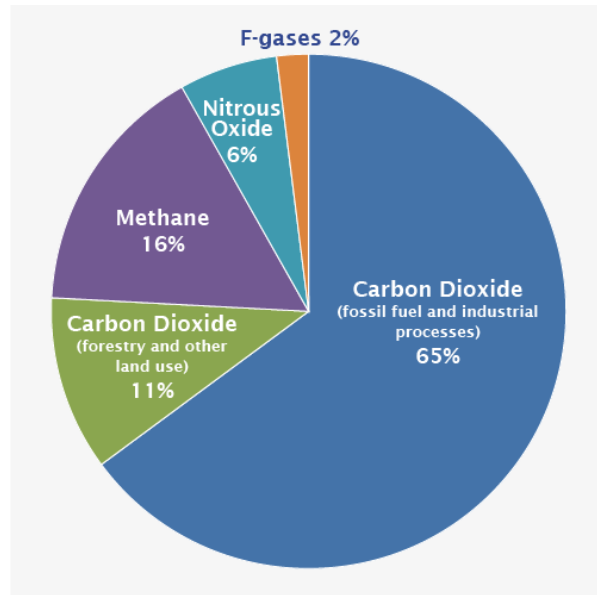


Figure 1.1. Global greenhouse emission by gas (IPCC, 2014).

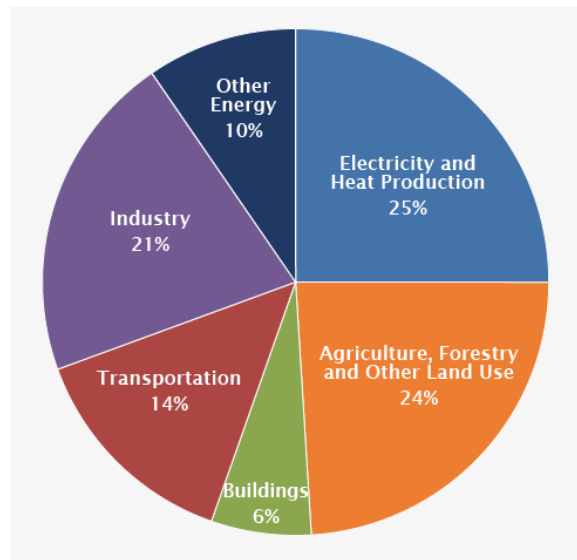


Figure 1.2. Global greenhouse emission by economic sector (IPCC, 2014).

On the other hand, the fuel energy price rose by 2 per cent in 2017 compared to the previous year according to International Energy Agency, IEA (2018) with a 1.4 per cent increase in global energy-related carbon dioxide emissions in 2017 (REN21, 2018). This is worrying news for the climate goal of 2030. Therefore, to eliminate the dependency on fossil fuels, future climatic changes and associated nasty environmental impacts, a global zero-carbon solution (clean

energy) is sought for. Thus, research motivations are high for exploring the future economy of clean energy production and to provide a clean and sustainable system. This has led to a significant global investment in renewable power amounting to USD279.8billion in 2017, a 2 per cent increment over the previous year (REN21, 2018).

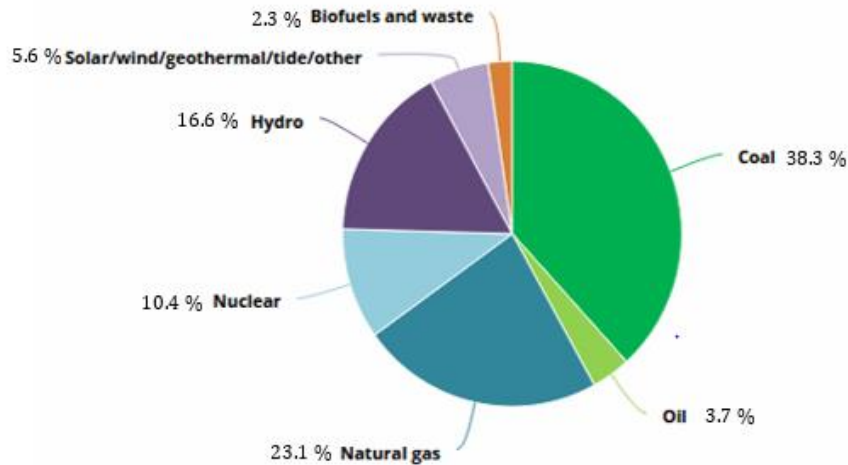


Figure 1.3. 2016 world gross electricity production by source (IEA, 2018).

In terms of renewable capacity additions in 2017, solar Photovoltaics (PV) accounted for nearly 55 per cent followed by 29 per cent wind power and 11 per cent hydropower. These capacity additions grew most notably in Asia accounting for about three-quarters of the global solar PV additions and slightly less than half of global wind power additions, with China leading the race (REN21, 2018). But investment in the first half of 2018 saw wind power go up by 33 per cent at USD57.2billion while solar PV went down 19 per cent compared to the first half of the previous year (Bloomberg, 2018a).

Despite the rapid expansion in renewable energy capacity and output, especially in solar PV, wind and hydropower, combustible fuels still account for 67.4 per cent of world gross electricity generation (Fig. 1.3) as reported by IEA (2018). In Hong Kong, the total GHG emission accrued to 40.6 million tonnes of carbon dioxide in 2018 which is about 0.5 per cent increment over the previous year, while population growth over the same period amounts to about 0.8 per cent (Environmental Protection Department, 2020). The primary reason for significant fossil fuel reliance in global electricity generation is the modest rise in the continued growth in global energy demand that is, continuous economic and population growth, thus poses a threat to meeting our daily thirst for energy in a clean and sustainable system.

Among the resources of clean energy, wind resource seems to be the central player at present in the transition to a cleaner future as it has received a greater portion of investments over the decades and to hasten the need to meet energy supply security and international emission targets of 2030, alternative clean energy resources such as solar, hydropower, tidal, geothermal etc. must play an intermittent role. As a result, there has been an increased interest in the exploitation of the future economic and predictability of renewable resources for the generation of power. One of the highly predictable, notwithstanding variable intensity, renewable resources that have attracted immense attention is tidal power which is a consequence of the gravitational effects of the rotational motion of the moon and the sun with respect to the earth (Bahaj, 2013). According to REN21(2018) report, the year 2017 saw optimism prevailed in the industry and developmental efforts channelled towards ocean energy especially tidal stream and wave energy in a bid to bringing it closer to commercialization with a promise of greater production scale and cost reduction.

1.2 Tidal Turbine Concepts

In the following sections, methods of harvesting tidal energy are discussed followed by the classification of tidal turbine configurations with examples.

1.2.1 Extraction Methods

The existing methods of extracting tidal energy are classified into two: by harvesting the energy from a tidal reservoir built behind a barrage or by direct extraction from a tidal stream. The former method involves the construction of a low dam across a bay or estuary such as the La Ranch scheme (Frau, 1993). The potential energy generated behind this dam as a result of tidal variations of the ebb and flood is converted into electricity as the flow exit the barrage. This method is the same as the conventional hydropower plant except that tidal currents flow is bidirectional. However, the cost of construction of dams, the environmental and ecological impacts remain major developmental mitigating factors to be resolved in tidal barrage technology (Rourke et al., 2010; REN21, 2018). Nevertheless, its availability and reliability with excellent potential give it a notch over other renewable energy technologies.

The latter method mimics the wind turbine technology except that water currents flow across hydrofoils to generate a torque that drives the generator from where power is transmitted to the land through cables. Although water is much denser than air with a relatively low flow rate, a typical water flow speed of 2-3m/s is considered practically significant and economically viable for tidal energy extraction. Tidal stream turbine also referred to as the marine current turbine (MCT) is still in an early stage of development compared to other renewable sources and as mentioned earlier, its working principle is like those developed for converting wind energy, with the three-bladed horizontal-axis turbine (ducted or non-ducted) predominantly adopted. It is envisioned that the rapid maturity gained in wind technology can make a significant impact in a marine application and maybe design ideas that failed in the wind market may be better suited in the marine application too. Thus, developers continue to investigate a broad range of different technologies to achieve successful deployment of full-scale tidal farms (Rourke et al., 2010).

According to IEA, tidal energy is theoretically estimated to be up to 1200 terawatt-hours (TWh) of electricity potential while Eurobarometer (2006) reported an estimate of 300GW (excluding offshore wind) by 2050 saving 500million tonnes of CO₂ emissions with the creation of 680,000 direct jobs. Today, there is almost 4.3MW of commercialized tidal stream installed capacity with the largest two plants located in South Korea – the Uldolmok Tidal Power Station and Northern Ireland– MCT’s SeaGen (Council, 2016). In early 2017, Scotland’s MeyGen Tidal Stream Energy completed the first phase of her 6MW horizontal-axis turbine. Also, Nova Innovation installed a third 100KW direct-driven turbine in Shetland, Scotland claimed to be the world’s first grid-connected tidal array (REN21, 2018).

1.2.2 Tidal Stream Generation

Marine energy technology developers are exploiting different types of tidal turbine configurations. There are 94 tidal device developers listed by the European Marine Energy Center (2017a) (EMEC) as the time of writing this report. The United Kingdom continues to lead the pathway in researching generation technologies and developing conceptual tidal project designs. The tidal stream devices are akin to underwater wind farms and at present, the European Marine Energy Center (2017b) has identified six main configurations; namely: horizontal axis turbine, vertical axis turbine, oscillating (or reciprocating) hydrofoil, enclosed tips (venture),

Archimedes screw and tidal kite. Among these configurations, the first three are more well-developed types of technology and are illustrated in Fig. 1.4.

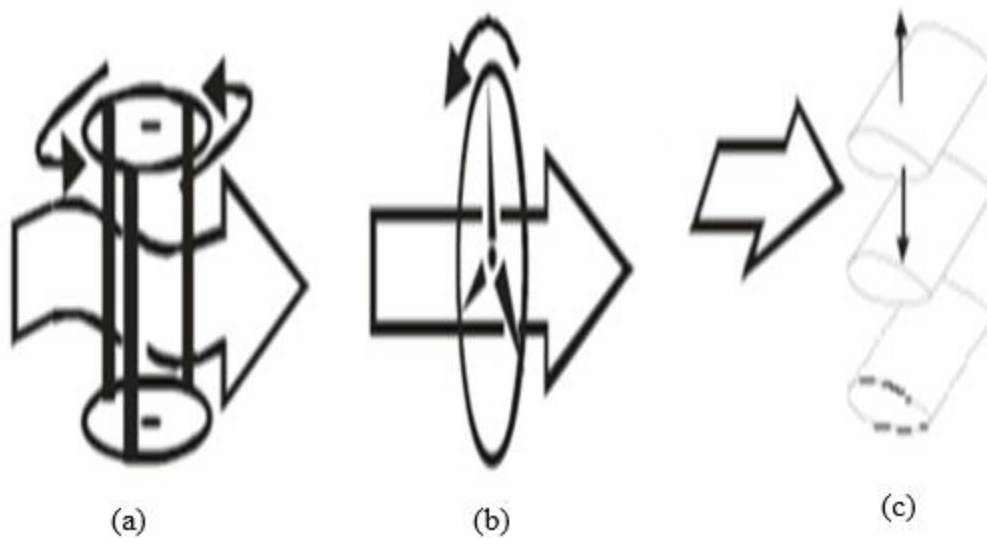


Figure 1.4. Tidal turbine configurations (a) vertical crossflow turbine (b) horizontal axial-flow turbine (c) oscillating hydrofoil (Entec UK Ltd, 2007).

The reciprocating hydrofoil uses a hydrofoil attached to a lever arm to cause a lift on either side of the lever as the tidal current flows over the hydrofoil. This resulting up and down movement is then used to drive a rotating shaft, either mechanically or by using hydraulics to generate electricity. Examples include an oscillating hydrofoil operated by Pulse Tidal in the Humber estuary (Don, 2009) and a Stingray project by Engineering Business Ltd (2005).

In the case of crossflow turbines, energy is extracted from water flows perpendicular to their axis and can be deployed vertically or horizontally depending on the position of the turbine axial plane relative to the flow direction. It is also referred to as the Darrius turbine concept. Examples include a ducted vertical turbine developed by Blue Energy International (2018), Kobold turbine (vertical axis) by Ponte di Archimedes International S.P.A (2018), vertical axis turbine (floating) by Edinburgh Design Ltd (Entec UK Ltd, 2007), Gorlov turbine by GCK technology (Gorlov, 1995) and the horizontal axis device developed by Ocean Renewable Power Company (2018) called TidGen.

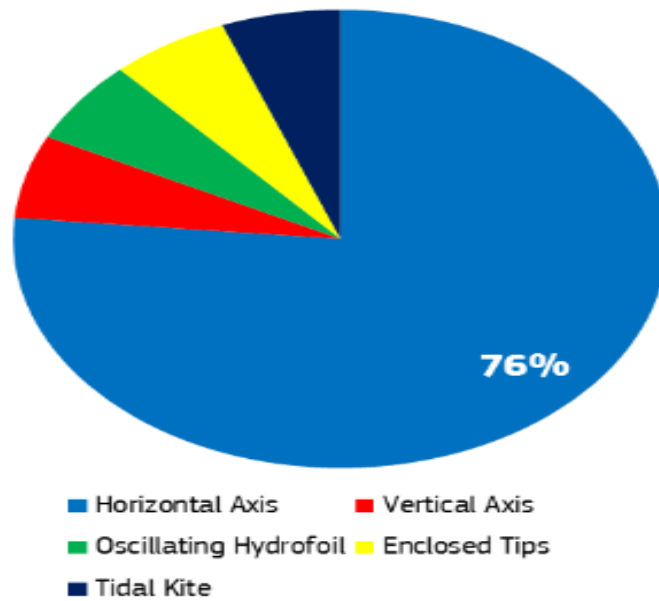


Figure 1.5. R&D effort for tidal technologies tested at full-scale (Magagna et al., 2016).

The axial-flow turbines mimic wind turbines to extract energy, but this time from moving water. The tidal stream forces the turbine mounted on a horizontal axis to rotate thereby generating power and in the year 2016, it accounted for about three-quarters of the tidal turbine devices tested (Fig. 1.5). Examples include the world’s largest tidal stream turbine (1.2MW) developed in 2008 by Marine Current Turbine Ltd (2018) in Strangford Lough, Northern Ireland, Atlantis Resources Cooperation AR 1000 tidal turbine tested at European Marine Energy Center (2018c) between 2011 and 2012, and Voith hydro’s 1MW plant (Voith Hydropower, 2018).

The freestream axial-flow devices, where the rotor is placed directly in the tidal stream, are this far reminded in the forefront of marine energy technology development. Water being 800 times the density of air means that the blades will turn at a slower rate in water relative to the air, a similar power is generated as it is proportional to the density of the fluid and the cube of velocity. Therefore, to augment flow and power output in axial-flow turbines ducted turbines have been proposed and have since gained support from tidal device developers. This support is most likely stemming from the significant improvement in the performance of ducted horizontal axis turbines in wind technology (Van Bussel, 2007). Also, the question of justification of balance in the cost of additional material relative to performance improvement for ducted tidal stream devices remains unravelled. Nevertheless, owing to uncommon advantages associated with such device: directionality of flow, blade-tip protection, and deployable in low-speed sites,

to quantify the effect of the duct on the power production of uni-directional and bi-directional turbine concepts as it relates to tidal streams forms the basis of this present study.

1.3 Thesis Objectives and Scope

Mitigation (2011) reported that horizontal axis tidal turbines are likely to follow a similar development path to wind turbines, where larger capacity turbines will be deployed depending on the progress in finding optimum duct shape (or size), blade design, and turbine array layout. In recent times, a duct equipped with a flange (referred to as a wind-lens) has attracted extensive attention. Unlike the traditional early designs of ducted turbines that rely on increasing the area ratio between the inlet and duct exit diameters, it depends on creating a low backpressure region through a strong vortex formation behind its broad flange and hence, a substantial increase in the wind speed. Although wind-lens has demonstrated significant power augmentation, a vast majority of investigations on wind-lens designs are mainly based on several existing conventional shapes. Therefore, the wind-lens design is still far from optimal. Many numerical and experimental data exist for wake characteristics of a single tidal stream rotor (non-ducted), however, it appears that the power performance of ducted turbines in a tidal farm, as well as the interaction effects between adjacent ducted turbines, have not been investigated in detail before. Hence, there are no or limited data available concerning the performance and wake characteristics of ducted tidal turbines within an array. It has also been demonstrated for a bare turbine that the performance of downstream turbines declines if it is subjected to the wake of the upstream turbine (Myers & Bahaj, 2012) and a higher upstream ambient turbulence tends to reduce the wake influence length (Maganga et al., 2010; Mycek et al., 2014). Thus, this study places emphasis on flanged duct turbines in bi-directional tidal flows. The main objective of this research is to investigate the hydrodynamics and wake structure of single row and two axially aligned flanged duct turbines in a bi-directional flow numerically and experimentally.

For the numerical aspect, several carefully designed flanged duct tidal turbines with different duct shapes (symmetric and asymmetric) for both uni-directional flow and bi-directional flow will be investigated for power augmentation and hence propose an optimum design. The assessment is carried out using the computational fluid dynamics (CFD) tool- Open-Source Field Operation and Manipulation (OpenFOAM). Further analysis to address the influence of blockage

ratio (ϵ), where $\epsilon = A/A_c$ (A and A_c are the rotor area and the approaching flow cross-sectional area respectively) on the performance of the ducted tidal turbine would be explored.

In the experimental investigations, we note that the wake characteristics associated with ducted tidal stream devices are seldom investigated. Here, we aim to experimentally examine in detail the interaction effects between the flanged duct and non-ducted marine current turbines in terms of performance and wake characterisation using the optimum duct design obtained from the numerical aspect of this research. Wake mapping is represented in terms of the centerline, lateral (crossflow), and vertical profiles of flow ratios and streamwise turbulence intensity. The wake measurements include downstream locations up to 20 and 30 rotor diameters for the single row and two in-line turbine arrays respectively since a thorough understanding of wake evolution is essential in developing efficient and robust tidal farm design. The first part of the experiment was dedicated to investigating the performance and wake characterisation of single (non-ducted) and flanged duct turbines. The performance and wake characterisation in reversed flow is also examined. In the second part, we considered two axially aligned configurations for each of the cases considered in the first part with a longitudinal spacing of 10 times the diameter (D_t) from the upstream turbine. Conclusions are drawn from the performance and interaction effects between two in-line marine current turbines compared to the results obtained from the cases of isolated turbines.

1.4 Significance and Value of the Study

Marine energy technology designs and development approaches are still in early-stage and the need to devise efficient and cost-effective tidal stream converters that will cope with the varying flow conditions of ocean energy remains a challenge to tidal developers. Computational fluid dynamics (CFD) validated with experimental data remains a very useful tool to help predict and provide vital information for community-scale tidal project design search and optimisation that will be used in the future by developers (Blanco Ilzarbe & Teixeira, 2009). Thus, this study will not only boost knowledge and confidence in tidal ducted turbine designs and performance but also contribute to global warming. Also, the novelty of this research is that it is the first to experimentally examine ducted tidal stream converters in isolation and within an array in terms of power augmentation and wake characterisation as it has been identified to be critical to

trimming cost down (Goltenbott et al., 2017; Marine Renewables Canada, 2018). Overall, a valuable set of experimental data set is produced for the research community which provide useful design information that will guide the course of future marine current turbine research and for validating theoretical and numerical methods.

1.5 Thesis Outline

This section presents the flow structure (Fig. 1.6) of this thesis report:

Chapter two introduces the ducted turbine and its mechanism. This is followed by a discussion of industrial proposed ducted tidal devices and a compressive review on ducted axial flow for both wind and tidal currents.

Chapter three presents a detailed numerical methodology employed in turbine modelling and an overview of the CFD tool used in this present study- OpenFOAM. Also, the descriptions of open channel flow and assumptions for modelling free surface effect for tidal turbine are discussed.

Chapters four discusses numerical model setup and validations followed by analysing all numerical data generated for several flange duct devices considered in the present study.

Chapters five introduces the experimental design and set-up of the model turbines used across all experiments. Test facility characteristics and array configurations tested as well as the flow measurement equipment, ADV and analysis procedure are outlined. Wake mapping is represented in terms of velocity ratios and turbulence intensity.

Chapter six analyzes and discusses experimental results following the procedures previously outlined in chapter four.

Chapter seven outlines conclusions on information gained from the findings, and recommendations for future work.

1.6 Chapter Summary

This chapter elaborated on the threat posed by greenhouse gases (GHG) emissions and efforts made so far to combat climate change since the Paris agreement in 2015 to foster the exploration of clean energy productions and technologies among member states. The optimism and industrial developmental efforts gained since 2017 were highlighted as tidal and wave energy show promising signs to come in on commercialization. It is followed by providing detailed tidal turbine concepts and innovations in marine energy technology embarked by developers. The ducted tidal turbine was then introduced as the focus of this present study owing to its availability and predictability. Also, the significance of the study, key research objective and thesis scoped were emphasized. The next chapter provides a comprehensive review of ducted turbines as proposed by developers and analyses of relevant research on axial flow ducted turbines both unidirectional and bidirectional in the wind and tidal technologies.

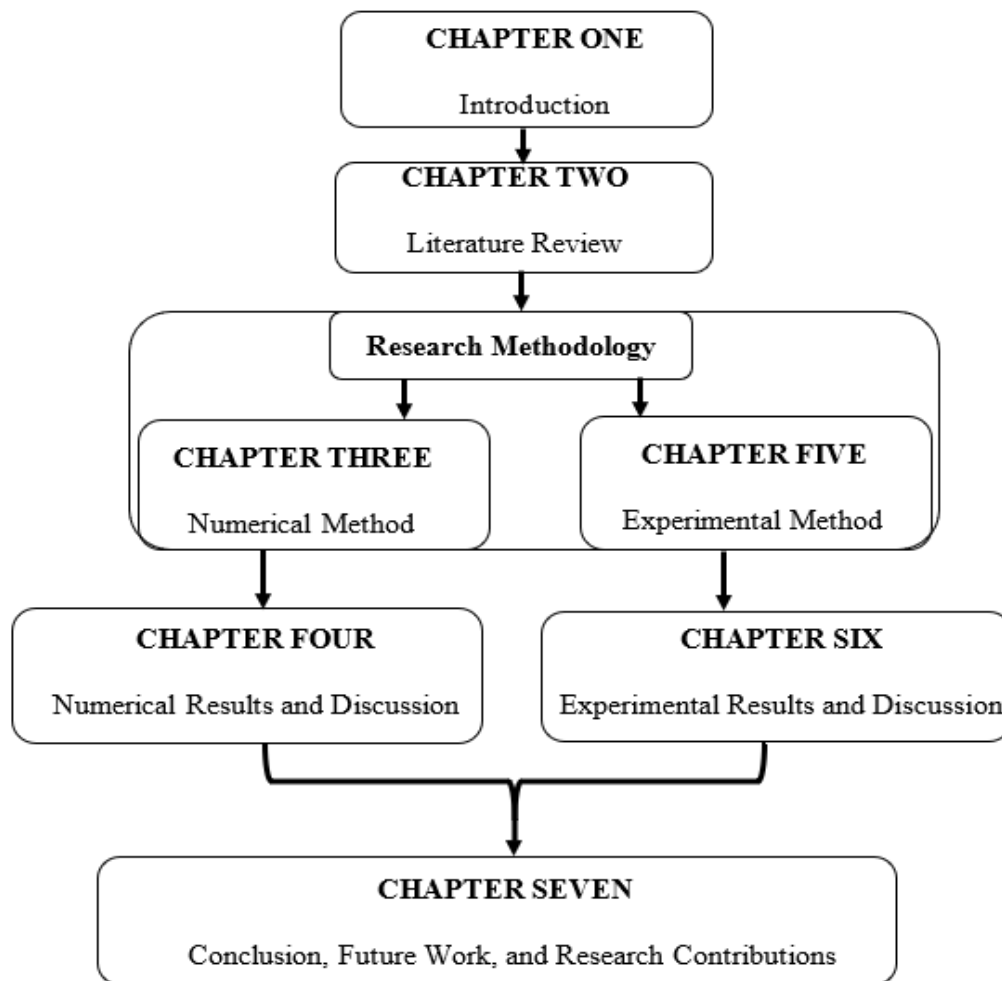


Figure 1.6. Overall flowchart of the thesis.

CHAPTER TWO

Literature Review

With the aim to reduce the human-induced climate change effect and the consideration of a rapid increase in energy price, research on clean energy production is actively promoted. As previously stated, global investment in renewable energy in 2017 was USD279.8 billion, a 2 per cent increase over the previous year (REN21, 2018). Although wind energy is still the major source of clean energy, water flow energy (tidal energy and wave energy) has received attention, and efforts have been put into its commercialization (REN21, 2018). Turbines have been developed a long time ago and are mainly used to extract wind energy. According to Okulov and Van Kuik (2012), the analytical study of turbine performance can be traced to Betz and Joukowsky in 1920. One remarkable solution of Betz-Joukowsky limit (BJL) theory is that the maximum amount of power that can be extracted from the fluid flowing through the turbine is $C_p = 16/27$ of the total available flow power, where C_p is called the power coefficient. To increase the value of C_p , the concept of a ducted turbine has emerged in the past several decades.

2.1 Ducted Turbines

The concept of ducted turbines (or diffuser-augmented) is the most commercially viable approach to increasing power output from a smaller diameter turbine. In this design, the turbine is placed inside a duct and the rationale behind consolidating a duct is to compel a convergence of fluid flow into the duct thereby creating strong vortices behind the duct resulting in a low-pressure locale and consequently more stream into the duct. This concept has been studied for many decades, even though no commercially successful designs have been developed to date (Sivasegaram, 1986; Van Bussel, 2007). Ducts proposed for wind and tidal turbines are basically of two types: unidirectional and bidirectional ducts (diffusers). Both induce increased mass flow rate either at the duct's inlet (unidirectional) or at the throat of the duct where the rotor is positioned (bidirectional).

2.2 Diffuser Augmentation Mechanism

Power augmentation well-developed devices can be categorized into ducted augmentation, tip-vane, and vortex augmentation systems. Others include obstruction type, wind deflection and vortex screw augmentation systems. The axial-flow turbines are well suited to all these power augmentation systems.

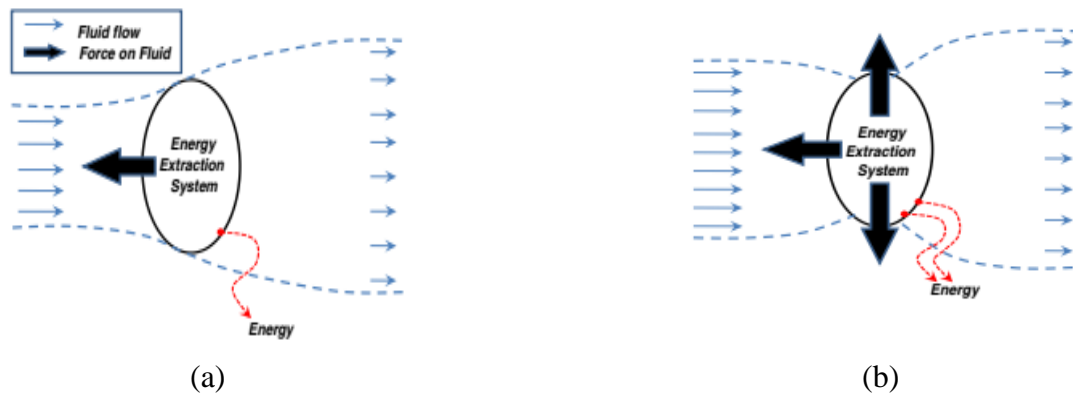


Figure 2.1. (a) Traditional wind energy extraction process (b) diffuser augmentation wind energy extraction process (Van Bussel, 1998).

The basic mechanism for power augmentation is to achieve mass flow enhancement. This is triggered either by increasing the mass flux through the wind turbine or by promoting wake interaction behind the rotor. Figure 2.1a depicts the mechanism for an increase in mass flux resulting from the exertion of a perpendicular force on the approaching fluid due to the presence of a duct around the rotor but absent in the energy harness process in the traditional bare turbine (Fig. 2.1a). By virtue of Newton's third law, an opposite force will be exerted by the fluid in an attempt to establish equilibrium, which is only possible if more fluid is forced through the duct. Consequently, the outward radial forces widen the streamtube downstream of the rotor with an increase in mass flow through the turbine. This implies a greater power output as power is proportional to the cube of flow velocity than that of traditional bare turbines with the same rotor diameter.

On the other hand, an explanation has been provided from the perspective of vorticity bound (Vries, 1979). Here the duct generates inward radial forces as the fluid inside it accelerates. These inward radial forces correspond to a ring of vortex distribution around the rotor plane. As

the bound vorticity confined within the vicinity of the rotor increases, it causes a higher mass flow through the turbine.

In the wake interaction with the external flow, a greatly reduced pressure region compared to the undisturbed free stream flow is created behind the rotor called the wake region. On recovering the exhausted kinetic energy behind the rotor by the mixing of the wake flow with the undisturbed free stream flow, more mass flow is caused to flow through the ducted augmented turbine (Fig. 2.1b). Diffuser horizontal axis wind turbine inherited these dual benefits in enhancing mass flow rate (hence, power augmentation) and remains the most actively investigated concept over the past decades (Van Bussel, 2007). However, the BJT curbs the theoretical maximum power extracted from the fluid to about 60 per cent for a single actuator disk. The BJT, nevertheless, has been demonstrated by some researchers (Igra, 1976 & 1981; Hansen et al., 2000; Abe et al., 2005) to be exceeded with the introduction of duct to generate significant suction at the duct exit as long as a significant sub-atmospheric pressure at the duct exit and a large pressure recovery within the diffuser is maintained (Gilbert et al., 1978); implying prevention of flow separation in the diffuser (or diffuser stall) due to adverse pressure gradients. The demonstrations of performance gain in relation to that of a bare turbine have been questioned as the vast majority of the works used rotor area as the reference area instead of the outer area of the duct as the reference area, as well as the neglect of the effect of the blockage ratio(ϵ), specifically in tidal turbines.

Therefore, the optimal geometric shape for ducted turbine performance and their economic benefit remains unclear. As a result, ducts of different geometries are continued to be investigated in the search for a suitable duct shape that may prove to be competitive to the cost of energy thereby making them commercially viable (Van Bussel, 2007).

2.3 Industrial Ducted Tidal Turbines

As previously stated, the idea of ducted turbines has been extended in the context of tidal power generation probably inspired by the significant innovations in the performance of ducted horizontal axis turbines in wind turbine technology (Van Bussel, 2007). Detailed information on these devices from developers is not readily made available to the public domain while some

information is released through other channels. In what follows, a brief overview of some bidirectional and unidirectional ducted tidal devices developed in the industry is presented.

2.3.1 Rotech Tidal Turbine (RTT)

Rotech Tidal Turbine (RTT) is a 1MW horizontal axial-flow tidal turbine developed by Lunar Energy Tidal Power (2006) located in the United Kingdom. The key feature is the bidirectional duct that encloses the rotor which accelerates tidal flows thereby increasing energy extracted from the rotor. Developers claim that this key feature helps it to avert the need for a pitch or yaw control making it simple to design and less expensive. Structurally, it comprises a gravity foundation, hydraulic motor, generator with the duct length and diameter 19.2m and 15m respectively (Fig. 2.2). In 2004, a one-twentieth model was tested, but installation methodology was redesign in 2011 with a target of 2.4MW turbine.

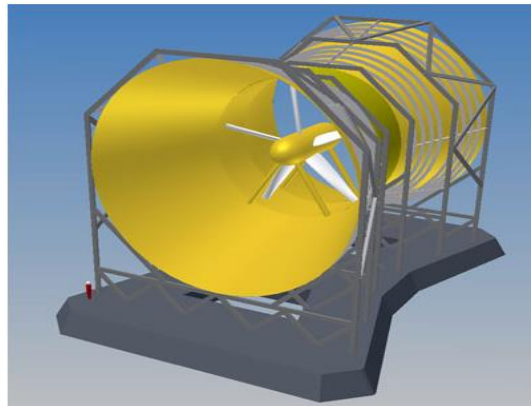


Figure 2.2. Rotech Tidal Turbine (Lunar Energy Tidal Power, 2006).

2.3.2 Solon Tidal Turbine

This is a 500KW rated horizontal-axis bidirectional device developed in 2006 by Atlantis Resources Corporation(2018) based in Singapore. It is similar to the device developed by Lunar Energy Tidal Power but without an aperture at its centre (Fig. 2.3). It was successfully tested in August 2008, and in the early 2010s, the company discontinued the Solon Tidal Turbine project to focus on freestream (non-ducted) tidal turbines citing financial crisis as their reason.



Figure 2.3. Solon Tidal Turbine (Atlantis Resources Corporation, 2018).

Atlantis Resources Corporation recent projects include: a successful deployment of AR1000, a 1MW freestream horizontal axial-flow turbine with fixed pitch blades and commissioned at European Marine Energy Center(2018d) in 2011, installation of AR1000 on (China Energy Conservation and Environmental Protection) CECEP’s Daishan demonstration site in China in 2014 and according to World Energy Council (2016) report, Atlantis Resources Corporation acquired MCT and SeaGen Ltd in 2015, and in collaboration with Lockheed Martin, started and installed AR1500 project in Pentland Firth, Scotland and the Bay of Fundy, Canada in Summer of 2016.

2.3.3 Open-Center Tidal Turbine

The Ireland based OpenHydro Ltd (2018) developed the 250KW-1MW Open-Center Tidal Turbine and installed it at EMEC in 2006. The center section of the rotor is open and fixed to the seabed with a tripod gravity foundation, but the enclosure was designed to house the generator parts unlike RTT (Fig. 2.4). It is the first tidal current energy company to connect to the United Kingdom national grid and start electricity generation. In 2013, it was acquired by DCNS and ongoing installations include a 4MW Cape Sharp project in the Bay of Fundy, Canada that will incorporate two 2MW OpenHydro turbines and the Raz Blanchard 5.6MW 4 device project (World Energy Council, 2016). However, in July 2018, EMEC announced the decision by Naval Energies to liquidate OpenHydro.

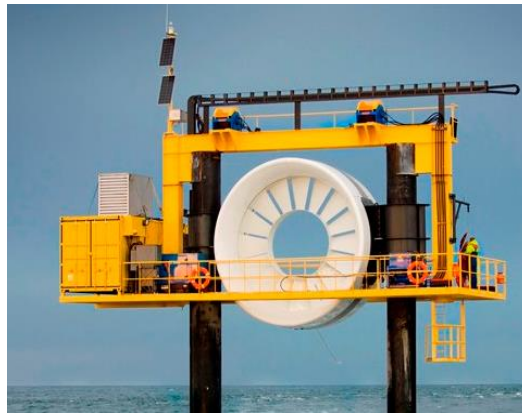


Figure 2.4. Open-center Tidal Turbine (OpenHydro Ltd, 2018).

2.3.4 Clean Current Tidal Turbine

In 2006, Clean Current Power Systems Incorporation (2013) installed a 65KW bidirectional horizontal axis rotor enclosed by a diffusing duct similar to an OpenHydro device at the Race Rocks ecological station, British Columbia, Canada (Fig. 2.5). And with the combination of solar and battery systems, it became the first completed marine renewable energy system to displace diesel on the island. However, due to the poor performance of its water-lubricated bearing system, it was removed and reinstalled in 2008. Then, in June 2015 it exited the hydrokinetic industry (Bloomberg, 2018b).



Figure 2.5. Clean Current Tidal Turbine (Clean Current Power Systems Incorporation, 2013).

2.3.5 Hydro Helix Tidal Turbine

This project was developed by the French-based company-HydroHelix Energies (2014) and designed like Lunar RTT except that it is pre-oriented to face the tidal currents (unidirectional).

It consists of a 200KW turbine while the expected tidal energy unit is an average of 1MW (Fig. 2.6).



Figure 2.6. Hydro Helix Tidal Turbine (HydroHelix Energies, 2014).

2.3.6 SeaUrchin Vortex Reaction Turbine

This is a scalable ocean, tidal or river turbine (2KW-1MW), designed dissimilar to the conventional wind turbine designs by Elemental Energy Technologies (2017) in conjunction with RPC Technology (Fig. 2.7). The developers claim that it is a 3rd generation self-aligning turbine that can be optimized to operate at a low flow rate (about 1.5m/s) making it deployable in the greatest range of locations around the world. Between 2011 and 2012, 2KW micro SeaUrchin was successfully tested in Australia, Pune and India. A feasibility study has also been completed for the 1MW utility-scale turbine. Elemental Energy Technologies is now pursuing a completely new turbine design, the Maco.



Figure 2.7. SeaUrchin Vortex Reaction Turbine (Elemental Energy Technologies, 2017).

2.3.7 MEGAWATTBlue

Guinard Energies (2017) are developing river and tidal ducted unidirectional hydrokinetic turbines. MEGAWATTBlue technology is declined in a range of turbines from 66 cm (2.5KW) to 8 m (1MW) rotor diameter. It carried out demonstrations of its P66 (3.5KW) tidal turbine (Fig. 2.8) in Brest harbour in 2017. The provider claimed that with the hybrid renewable production system- P66, photovoltaic and battery electricity will be provided to the non-interconnected areas (islands). P66 was recently exhibited at the International Conference on Ocean Energy held in June 2018 at Cherbourg. At present, the construction of the P154 (20KW) turbine is underway and is planned to be installed at the end of 2018 in French Brittany.



Figure 2.8. MEGAWATTBlue (Guinard Energies, 2017).

2.3.8 Underwater Electric Kite

This unidirectional hydrokinetic turbine (Fig. 2.9) is developed by UEK Corporation (2014). No further information is released to the public domain.



Figure 2.9. Underwater Electric Kite (UEK Corporation, 2014).

Table 2.1. Summary of ducted tidal turbines from developers.

Country	Project	Developer	Rotor Configuration	Capacity	Status	Other News
United Kingdom	Rotech Tidal Turbine	Lunar Energy Ltd	Horizontal Axis (Bidirectional)	1MW	<ul style="list-style-type: none"> 1/20th model tested in 2004 2.4MW planned for 2011 	<ul style="list-style-type: none"> No updates
Singapore	Solon Tidal Turbine	Atlantis Corporation	Horizontal Axis (Bidirectional)	500KW	<ul style="list-style-type: none"> 500KW tested in 2008 	<ul style="list-style-type: none"> Solon project suspended in the early 2010s Now developing free stream tidal turbines AR1000 commissioned in 2011 at EMEC and demonstration in CECEP's Daishan, China in 2014 Acquired MCT and SeaGen Ltd in 2015 AR1500 installed in Pentland Firth and the Bay of Fundy in 2016
United Kingdom	Open-Center Tidal Turbine	OpenHydro Ltd	Horizontal Axis (Bidirectional)	250KW – 1MW	<ul style="list-style-type: none"> 250KW tested and installed at EMEC in 2006/2007 	<ul style="list-style-type: none"> Acquired by DCNS in 2013 4MW Cape Sharp and 5.6MW 4 device Raz Blanchard projects (underway) Liquidated in 2018 as announced by EMEC
Canada	Clean Current Tidal Turbine	Clean Current Power Systems Incorporation	Horizontal Axis (Bidirectional)	65KW	<ul style="list-style-type: none"> Installed in 2006 Removed and later reinstalled in 2008 	<ul style="list-style-type: none"> Exited hydrokinetic industry in 2015
France	Hydro Helix	HydroHelix Energies Ltd	Horizontal Axis (unidirectional)	250KW – 1MW	<ul style="list-style-type: none"> No information 	<ul style="list-style-type: none"> No update
Australia	SeaUrchin Vortex Reaction Turbine	Elementary Energy Technologies Ltd	Horizontal Axis (unidirectional)	2KW – 1MW	<ul style="list-style-type: none"> 2KW tested in Australia, Pune and India between 2011 and 2012 1MW feasibility study completed 	<ul style="list-style-type: none"> Now developing a new turbine design called Maco from 2013
France	MEGAWA TTblue	Guinard Energies Ltd	Horizontal Axis (unidirectional)	<ul style="list-style-type: none"> 3.5KW (P66) 20KW (P154) 	<ul style="list-style-type: none"> 3.5 KW tested in 2017 20 KW underway 	<ul style="list-style-type: none"> 20KW demonstration planned for the end of 2018
United Kingdom	Underwater Electric Kite	UEK Corporation	Horizontal Axis (unidirectional)	<ul style="list-style-type: none"> Not known 	<ul style="list-style-type: none"> Not known 	<ul style="list-style-type: none"> Not known

2.4 Research Studies on Ducted Turbine

Many studies have investigated the claimed superiority of diffuser-augmented turbines to extract an increased amount of power over bare turbines by developers. Although some research demonstrated diffuser enhancement in turbine performance especially for unidirectional ducted turbines (unlike bidirectional ducts), no diffuser-augmented turbine has been proven to be commercially viable to this present date.

In the next three sections, analytical frame, analyses of diffuser-augmented turbines of wind and tidal studies are presented.

2.4.1 Analytical Framework

One of the pioneers to acknowledge the potentials associated with diffuser-augmented wind turbines was Betz and Joukowsky in 1920. These authors formulated the diffuser-augmented axial wind turbine theory, in which the upper bound to the maximum amount of energy that can be extracted from the air stream flowing through an idealized actuator disk (no energy loss) was described and referred to as Betz-Joukowsky limit (BJL). BJL, $C_p = 16/27$ (where C_p is called the power coefficient) implies that no ducted turbine can extract energy more than a bare turbine even if an additional wind flow is directed into the turbine by the diffuser.

Research interest in ducted turbines was abandoned because of the assertion from Betz-Joukowsky theory. However, in the 1950s, a one-dimensional (1D) analytical study on ducted windmills by Lilley and Rainbird (1956) suggested otherwise. Their findings showed that a duct could provide at least a 65 per cent increment in power over a bare turbine with the same diameter and a direct function of the viscous loss, diffuser exit ratio and the external shape of the duct.

Lawn (2003) used a 1D theory to analyze the performance of a shrouded turbine by treating the ducts upstream and downstream of the turbine as contractions or expansions having specified diffuser efficiencies. Lawn deduced that by choosing a more lightly loaded design a 33 per cent enhancement in the power coefficient over a bare turbine of the same diameter can be achieved. In other words, for a given diffuser efficiency, there is an optimum turbine resistance for

generating maximum power, because the swallowing capacity of the duct is increased as the resistance decreases.

Due to lack of theoretical insight into optimising the performance of ducted axial wind turbine, van Bussel (2007) adopted a modified version of the standard actuator disk momentum theory and showed that power augmentation in a duct system is reliant on the increase in the duct exit ratio and/or back-pressure drop at the exit. The theory predicted an upper bound of $8/9$ for pressure drop similar to that for a bare wind turbine. This however neglected viscous loss and flow separation effects.

Jamieson (2008) developed a generalized Blade Element Momentum (BEM) theory to deduce the limit for energy extraction from ducted devices. This new limit places the BJL as a special case of energy extraction in open flow. For a confined environment like the tidal system, Garrett and Cummins (2007) carried out a 1D analytical study for a bare tidal turbine and found that the maximum power coefficient, $C_{p,max}$ of a bare turbine is proportional to the blockage ratio (ϵ) i.e. $C_{p,max} \propto 1/(1 - \epsilon)^2$. This implies that for a bare turbine, the BJL caps the theoretical maximum power extracted from the fluid at about 60 per cent for a single actuator disc in an unconfined environment and $0.6(1 - \epsilon)^{-2}$ for a confined environment.

2.4.2 Analyses of Diffuser Augmented Wind Turbines

Gilbert and Foreman (1979) succeeded in increasing the fluid flow inside the duct by utilizing several flow slots to control the boundary layer but failed to prevent pressure loss by flow separation. To improve this design, a group in New Zealand in the 1990s developed a multi-slotted duct diffuser to prevent flow separation within the duct (Phillips et al.,1999). This device was called Vortec 7, but it failed to be commercialized due to an additional requirement of a yawing mechanism and the high cost incurred. Igra (1981) introduced the use of a ring-shaped flap to improve ducted turbine performance. His result showed that using an appropriate ring-shaped flap an 80 per cent power augmentation could be obtained while about 25 per cent power augmentation was achieved in its inner rear part.

Hansen et al. (2000) used an actuator disk CFD model to show that the BJL can be exceeded by a ratio relative to the increase in mass flow through the rotor. The author concluded that the actuator disk approach is sufficient for modelling the rotor. However, this conclusion is false as the actuator disk model assumes no flow swirl.

Philips et al. (2003, 2008) carried out Vortec 7 design optimization using CFD and was validated with a series of wind tunnel tests. The CFD model successfully predicted the flow behaviour with the diffuser, but the power prediction from the wind tunnel show deficiencies to that of the CFD model. This, they attributed to the poor performance of the $k - \omega$ turbulence model in capturing boundary layer separation in the CFD model.

A new concept of the ducted turbine was developed with a flange attached at the exit of the duct (Fig. 2.11) called wind-lens (Abe & Ohya, 2004; Abe et al., 2005; Ohya et al., 2008). Abe and Ohya (2004) computational and experimental results based on another kind of diffuser-augmented system equipped with a large flanged attached at the exit of the shroud showed that loading coefficient has a strong relationship with flow separation and that the best performance of a flanged diffuser is considerably smaller than that for a bare wind turbine. Abe et al. (2005) carried out a numerical and experimental investigation of the flow fields of a small wind turbine with a flanged diffuser. The result indicated a power coefficient increment by a factor of 4 compared to the bare wind turbine. Ohya et al. (2008) demonstrated that the flanged-diffuser plays the role of a device for accelerating and collecting airflow and automatically controls the yawing motion. Parameters investigated were diffuser opening angle, flange height, hub ratio, centre-body length and inlet shroud. Results from the wind tunnel and field experiments were in good agreement with power augmentation of about 4-5 times that of the bare wind turbine of the same rotor diameter and speed.

Kardous et al. (2013) carried out a numerical simulation, Particle-Image-Velocimetry (PIV) visualization and wind tunnel experiments to investigate the effect of the flanged height on wind velocity increase at the inlet section of an empty flanged diffuser. The result showed that the presence of the flange alone is responsible for the additional acceleration of the wind between 13 per cent to 23 per cent. The authors further identified a critical ratio (flange height/inlet section diffuser diameter = 0.1) beyond which the flange height seems insignificant to wind velocity increase. The study however neglected the effect of turbine resistance in the airflow and duct interaction.

El-Zahaby et al. (2017) studied the effect of the flange angle of a diffuser turbine and found that flow acceleration at the entrance of the diffuser is optimized at an angle 15° with a 5 per cent power coefficient increment compared to the diffuser with a normal flange.

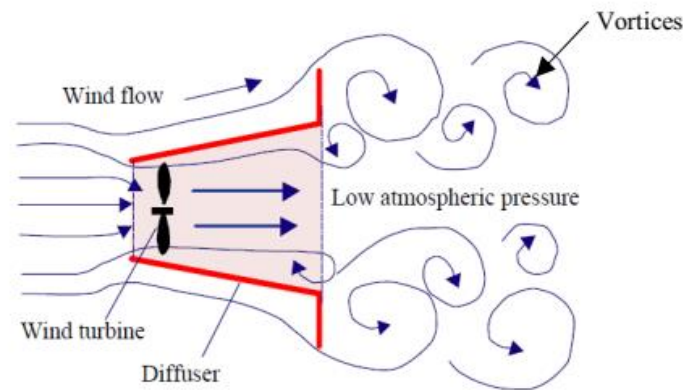


Figure 2.11. Schematic cross-sectional view of increasing wind flow speed mechanism around a flanged diffuser (Ohya et al., 2008).

2.4.3 Analyses of Diffuser Augmented Tidal Turbines

The study of ducted tidal stream devices has been examined by several researchers. Setoguchi et al. (2004) investigated the performance of a bidirectional diffuser for a tidal stream in a wind tunnel. The diffuser consists of a diffuser-straight part-diffuser and brims mounted at both ends of the diffuser system. The straight case with a brim height to rotor diameter ratio of 2.0 showed the best performance with an increased flow velocity of about 1.3 times the freestream flow velocity. The authors did not consider a case with a turbine present.

As part of the MegaWattForce project from Guinard Energies, Munch et al. (2009) and Luquest et al. (2011) carried out turbine performance assessment using BEM theory. Calculations showed flow velocity augmentation inside the diffuser. However, simulations were performed in open flow conditions. Gaden and Bibeau (2010) performed a parametric study of diffuser augmented tidal turbine using a momentum source model. Investigations involved varying diffuser size and angle with a result indicating that there are an optimum size and angle beyond which power

augmentation becomes insignificant. On rescaling the power coefficient with the device outer diameter, the authors found that the power increment was twice that of a bare turbine.

Shives and Crawford (2010) characterised the efficiency of a tidal turbine by defining efficiency (η) as the ratio of power produced (P) by the device to the power extracted (P_E) from the flow (*i. e.* $\eta = P/P_E$). The authors concluded that there is a trade-off between power and efficiency for a given turbine design in the tidal stream turbine. This study, however, neglected the effect of drag, discrete number of blades, blade tip loss and wake swirl. Shives (2011) used analytical and numerical modelling to study the unidirectional duct of the aerofoil cross-section. The author's results acknowledged that the non-ducted turbine can produce more power per installed device frontal area. Shives and Crawford (2011) further implemented a validated CFD modelling approach on several duct designs to gain insight into the effects of viscous loss, flow separation and base pressure on mass flow increment provided by the duct. The author found that viscous loss in the inlet is negligible for the cases considered, flow separation and increase in diffuser expansion, inlet contraction and inner exit angle led to a significant diminish in diffuser efficiency. They concluded that it is worthwhile to pursue a flanged diffuser that creates a large base pressure effect.

Sun and Kyojuka (2012) combined the CFD method, BEM theory and circulating water channel (CWC) experiment to investigate the performance of a bare turbine and a unidirectional brimmed diffuser from wind-lens technology. The presence of a diffuser proved to effectively improve the performance of the tidal turbine by a factor of 2.5 compared to the bare turbine. Calculated results from both CFD and BEM were in good agreement with the experimental result for tip speed ratio (TSR) of about 3.0 but CFD failed to capture the experimental results for the TRS more than 3.0. This shortfall in the CFD result was attributed to the omission of the turbine resistance in the simulation. Fleming (2011) introduced tip loss correction into the CFD-BEM model developed by McIntosh et al. (2011). The authors found that the tip vortex generated by the rotor is absent in a ducted turbine. Belloni (2013), carried out a numerical investigation of a bi-directional tidal turbine. Actuator disk and CFD-BEM models were employed in the analysis of ducted, open-centre and bare turbines. Belloni (2013) study showed that the performance of devices are greatly affected by increasing blockage and power output from ducted turbines is not more than that from a conventional turbine relative to the outer diameters of the devices. Fleming et al. (2016) analysis on a series of bidirectional duct geometries and showed that absolute power augmentation by a duct is a consequence of the increase in blockage.

Table 2.2. Maximum values of C_p and C_p^* for various ducted turbines.

Investigators	Type of Ducted Turbine	Blockage ratio, ϵ , and Corresponding B JL	C_p	C_p^*	C_p (bare)
Fleming and Willden (2016)	Bi-directional:	$\epsilon=0.131$	0.82	0.46	0.85
	B	B JL=0.784	0.85	0.48	
	C		0.63	0.483	
	D		0.48	0.43	
	E		0.60	0.45	
Belloni (2013)	Bi-directional	$\epsilon=0.035$ B JL=0.644	0.63	0.42	0.63
	Bi-directional	$\epsilon=0.2$ B JL=0.938	0.94	0.62	0.90
	Open-center	$\epsilon=0.035$ B JL=0.644	0.59	0.39	0.63
Shives and Crawford (2011)	Scaled NaCA0015 aerofoil (D7)	$\epsilon=0.03$ B JL=0.638	1.10	0.38	0.58
Ohya et al. (2008)	Flanged diffuser ($L/D = 1.25$; $h/D = 0.5$; $\theta = 4^\circ$)	n.a (open-type test section)	1.38	0.21	0.26
Abe and Ohya (2004)	Flanged diffuser ($L/D = 1.25$; $h/D = 0.35$; $\theta = 15^\circ$)	$\epsilon=0.011$ B JL=0.606	1.30	0.32	0.60
Hansen et al. (2000)	NaCA0015 aerofoil(deformed)	$\epsilon=0.0041$ B JL=0.605	0.94	0.51	0.59
Igra (1981)	Shroud with ring-shaped flap (NACA 1412)	n.a (pilot-plant exposed to the atmosphere)	1.79	0.45	0.74

The authors concluded that normalising with the outer diameter of any device, ducted turbines yielded a low power coefficient compared to bare turbines. In continuation, Allsop et al. (2017) developed a numerical BEM theory model to analyse flow through a duct in interaction with a high-solidity embedded rotor. The rotor power and thrust predicted by the ducted BEM theory model show almost to be identical to the CFD-BEM study, for TSRs up to the optimal operating condition while overestimation was observed at higher TSRs. Borg et al. (2020) also utilised blade-resolved CFD to analyse the hydrodynamic performance of a ducted, high-solidity tidal

turbine, particularly within the presence of duct-rotor influence. The resultant hydrodynamic performance characteristics highlighted a peak power coefficient and thrust coefficient of 0.34 and 0.97 respectively at a nominal TSR of 1.75.

However, the demonstrations of performance gain in relation to that of a bare turbine have been questioned as the vast majority of the works used rotor area as the reference area instead of the outer area of the duct as the reference area, as well as the neglect of the effect of the blockage ratio. The maximum values of C_p (rotor area is used as the reference area) and C_p^* (maximum duct cross-sectional area is used as the reference area) for various ducted turbines reported in some selected literature are listed in Table 2.2. It shows that only the maximum C_p s are nearly equal to or greater than the BJL while the maximum C_p^* s are all below the BJL. Therefore, this further affirms that the geometric shape of a duct for a turbine with optimum power performance remains unclear.

Section 2.3 presented several full-scale marine current energy converters undergoing demonstrations towards achieving commercial viability of marine current energy technology. The development of arrays composed of multiple turbines has been identified as the future marine energy industry (Funke et al., 2016; Goltenbott et al., 2017; Marine Renewables Canada, 2018). To date, array design has focused on grids of turbines with identical power coefficients (Vennell et al., 2015). The layout of such arrays is site-specific as several factors determine inter-device spacing; flow field generated by the MCT devices, water-depth constraints, turbulent mixing, lack of field data and environmental impacts (Blunden & Bahaj, 2007; Myers & Bahaj, 2012). A turbine array layout is mainly classified into (1) regular or staggered (2) inter-spacing (lateral or longitudinal) between generators. We recall that kinetic energy extraction of any turbine causes a reduction in the momentum of the downstream wake flow. Hence, for multiple configurations of tidal turbine array, some turbines might be in the wake of the upstream turbines. As a consequence, may lower power performance. Therefore, it is crucial to understand the flow characteristics of the wake as it is directly related to the overall turbine array performance and wake effect on the performance of downstream turbines to determine the appropriate spacing between turbines. The wake structure and its dissipation are simplified by considering the wake as two distinct regions: near and far wake. According to the description by Bahaj et al. (2007b), the near wake is where the flow field is significantly influenced by the rotor specific geometry, device support structure and performance of the turbine. This region is

typically characterized by slow-moving fluid, high turbulence and vortices shedding from the blade tips and the device support structure. Typically, the near wake extends up to 4 rotor diameters downstream, in which time the ambient turbulence of the freestream flows breaks down the bounding vortices while the far wake is characterized by wake dissipation and expansion. The far wake is largely influenced by convection and turbulent mixing with the ambient flow and extends up to the point far downstream where the velocity profile approaches the existed velocity upstream of the rotor. The velocity profile in the wake of a wind turbine is presented in Fig. 2.12.

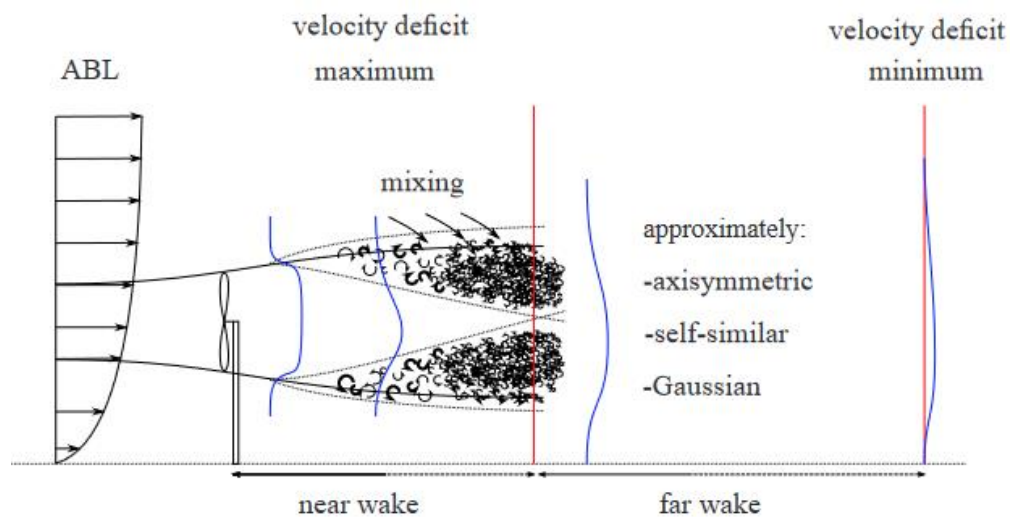


Figure 2.12. Velocity profile in the wake of a wind turbine (Sanderse, 2009).

Experimental array studies have been conducted on the interaction of a relatively small number of turbine arrays due to the high costs and complex measurement arrangements for detailed flow representation. Myers and Bahaj (2009) studied the influence of the device structure and the rotor on the near wake mapping of a tidal current turbine. Upstream inflow measurements were acquired using both Acoustic Doppler Velocimeter (ADV) and a Laser Doppler Velocimeter (LDV). Results showed that the support structure has a large influence up to 5 rotor diameters downstream of the rotor and at 10 rotor diameters the velocity recover to about 80% of the freestream velocity. Maganga et al. (2010) combined LDV and PIV to investigate the efficiency of a tri-bladed horizontal axis turbine quantified by the measurement of the thrust and the amount of power generated by the rotor for various inflow conditions and characterise both near and far wake generated by the turbine. Higher turbulence flows showed to recover more rapidly,

as did flows with a lower thrust. Their experiment also shows that misalignment of a fixed turbine would result in a significant loss of thrust and power. Myers and Bahaj (2012) experiment using several multiple actuator disks arrangement to quantify the flow field around a 2-row array, device/device interaction as well as a study of the structure of the far wake region where subsequent devices could be installed. Their results highlighted that for a single row array a close lateral separation increases the thrust force acting upon adjacent rotor disks while optimum lateral separation leads to an accelerated jet flow passing between adjacent rotor disks. This flow possessed 22% more kinetic energy than the flow far upstream with no measurable negative effect upon the 2 actuator disks paving way for a synergistic effect whereby an array of devices can generate more power than an equivalent number of isolated machines. Javaherchi et al. (2013) utilized the ADV and PIV system to characterize the flow upstream from the turbine and in the wake of the turbine at the blockage ratio of 20%. Four turbine spacing configurations were tested. They considered axially aligned configurations and configurations with the upstream and downstream turbines at a lateral offset from the middle turbine by 0.5 rotor diameter. Their results showed that for the axially aligned configurations, the downstream turbine extracted more power than the middle turbine, which indicates that the combined wake of the upstream and middle turbines recovers velocity more quickly than the wake of the upstream turbine alone. For the turbines at a lateral offset, the turbine configuration with 5 rotor diameters separation resulted in more power extraction than the middle turbines in the axially aligned configurations. High turbulence intensity from the tips of the rotor was observed at 3 rotor diameters downstream of the rotor plane and diffuses towards the centerline at 5 rotor diameters downstream. Stallard et al. (2013) conducted an experimental study investigating the influence of bounding surfaces on the structure of the wake of tidal stream turbines. They considered both staggered and axially aligned configurations. The result presented showed that the mean velocity deficit along the centerline of the wake of a single rotor reduces by 80% at 2 rotor diameters downstream and subsequently recovers to within 20% and 8% of the incident flow at 10 rotor diameters and 20 rotor diameters downstream respectively. The normalized turbulence intensity is between 10% and 15%, with the maximum occurring 3 rotor diameters downstream. For lateral spacing of three rotor diameters between adjacent rotor centers, the wake of each rotor is very similar to that of an isolated rotor while lateral profiles at distances greater than six-rotor diameters indicate a nearly constant velocity deficit and little variation of turbulence intensity between the centers of the outermost rotors of the array for rows of two, three and five rotors. Mycek et al. (2014) used LDV to investigate the performance and interaction effects of two-device systems compared to

that of a single device. Results demonstrated that increasing the inter-device spacing to retrieve higher individual power can only be done to the detriment of the total number of turbine rows in a given space when considering an array of devices. It was also observed that going from 3% to 15% turbulence intensity decreases the power coefficient by a maximum of 10% while the wake recovery is reduced by more than 5 rotor diameters. A more recent experimental study by Chen et al. (2017) on a detailed investigation of wake evolution behind a horizontal axis turbine with three blades was conducted in a recirculating water flume employing ADV. Their result indicated that velocity reduction in the wake was a result of the kinetic energy extraction and blockage effects of the tidal stream turbine rotor and stanchion, and due to a low TSR and blockage of the hub, the maximum velocity deficit was located at the wake core. The result further showed that in the near wake, the stanchion has a significant influence on the wake structure while in the far wake, the wake turbulence is strong and anisotropic and would affect the performance of turbines located downstream when considering turbines in an array. Chen et al. (2019) confirmed that the attenuation processes of near wake hydrodynamics were dependent on rotor characteristics while the far wake recovery was mainly influenced by ambient turbulence intensity. Su et al. (2018) carried out numerical and experimental investigations on the hydrodynamic performance of a horizontal tidal current turbine showed that maximum power conversion efficiency could reach up to 47.6% while all the power efficiencies are over 40% for TSRs ranging from 3.5 to 6. It also revealed that the yaw angle does not affect its efficiency significantly when it is less than 10° while the flow patterns and pressure distributions in the wake region are found to be indeed 3D and turbulent.

Several CFD studies have also been reported with a more detailed representation of tidal turbine rotors to further investigate the wake characteristics of single turbines and small arrays. Lee et al. (2010) used a steady incompressible 3D flow simulation to investigate the optimal layout for ocean generators. The authors assumed that wake interference is the dominant factor in determining minimum inter-row spacing and found that the appropriate turbine spacing is three (3) times the turbine diameter. Turnock et al. (2011) suggested from their CFD analysis that placing turbines in regular pattern outperformed staggered configuration. The authors' deduction was based on flow velocity recovering from one rotor simulation. Malki et al. (2014) used CFD-BEM to examine wake recovering and turbine performance for different turbine array layouts. Staggered configuration resulted in 10% turbine performance improvement contrary to Turnock et al. (2011) hypothesis. Nash et al. (2015) used a numerical approach to investigate tidal turbine

layout optimization. The authors recommended spacing of 3-4 rotor diameters across-stream and 1-4 rotor diameters along a stream with the downstream rows staggered to avoid wake effects of the upstream turbines. A detailed review by Vennell et al. (2015) suggested that there is still much to learn about inter-row spacing in optimizing array layout. Lin et al. (2015) developed a 3D shallow water equations (SWE) model for predicting distributions of velocity deficit and tidal energy density. The model revealed for a prospective tidal energy farm that the velocity deficit areas are in strip shapes with the maximum velocity attenuation around the hub height and due to blockage ratio, the velocity values increased at the bottom and surface of the turbine similar to the work by Chen et al. (2017). Additionally, the recovery of the wake is slower in the turbine array case than in the single turbine case. Liu et al. (2016) carried out a fully resolved numerical simulation with two inline tidal turbines with the second turbine located 8 rotor diameters downstream of the first. Their results showed that the downstream turbine can only produce less than 50% of the upstream one in terms of power at such a distance. The velocity contours show the downstream turbine working in the flow containing significantly reduced wake flow speed and a further reduction in the wake of the downstream turbine. Also, a significant increase in turbulence intensity is observed at about 4 rotor diameters downstream of the second turbine due to the accumulation of turbulence induced by rotating behaviours of both turbines and a faster velocity downstream recovery.

The wake of a ducted turbine has received little attention except for a few recent experimental and numerical studies on the flow within the cavity and around the periphery of duct exit of a flanged diffuser structure of a wind turbine (Abe et al., 2005; Ohya et al., 2012) and an experimental study of a model diffuser augmented tidal stream turbine on the impact of the diffuser upon the turbine's performance in yawed flows (Cresswell et al., 2015). Cresswell et al. (2015) examined the effects of diffuser augmentation on wake propagation and recovery. Their findings showed that the performance characteristics of an individual turbine are significantly improved by diffuser augmentation under yawed flow, but its wake recovery was found to be poor, recording a wake recovery rate that is less than half that of a bare rotor at 9 rotor radii downstream. This reduced wake recovery implies that array spacing would need to be greater for diffuser augmented turbines coupled with additional measures to promote wake mixing for array deployment. Shives and Crawford (2010) argued that less aggressive duct designs seem more appropriate, and efficiency becomes more critical as the tidal farm grows.

The literature review on tidal flows shows that studies published have either focused on computational or experimental investigations examining power performance and wake characterisations of mostly non-ducted tidal turbine systems. Some other computational studies focused on the power performance of ducted tidal turbines while one experimental study on wake characterisations of a single ducted tidal turbine to our best knowledge. As most tidal current sites are bi-directional and with bathymetry constraints, array layouts will necessarily take the form of highly optimized geometric configurations with reduced lateral inter-device spacing (Myers & Bahaj, 2012). This study is the first to place emphasis on the array of flanged duct turbines in bi-directional tidal flows. In this study, several carefully designed flanged duct tidal turbines with different duct shapes (symmetric and asymmetric) for both uni-directional flow and bi-directional flow are investigated for power augmentation and hence propose an optimum design. This assessment is carried out using CFD. As at present, there are limited experimental data available on duct performance and wake characterisation of ducted tidal turbines. Due to power augmentation associated with the ducted turbine, there exists an acute need for more experimental data to provide valuable information on the performance and wake characterisation of ducted tidal turbines. The novelty of this study is that it is the first to experimentally explore duct performance and far wake characterisations of flange-ducted turbines in isolation and within an array. Using the proposed optimum design from Maduka and Li (2021), the performance of each turbine and flow characteristics of the wake of flange-ducted turbines are experimentally examined for a single row turbine and two tidal turbines arranged in tandem with the second turbine located at 10 rotor diameters downstream of the first.

2.5 Chapter Summary

The concept of diffuser-augmentation turbines is the most commercially viable approach studied due to the inherent power augmentation potential even though no commercially successful designs have been developed to date. The literature surveyed showed there is an upper bound to the amount of power that can be extracted from fluid and according to BJL, this amounts to about 60 per cent. However, authors working on unidirectional diffuser-augmented turbines seem to disagree on this limit value. Some argued that the increase in mass flow caused by the presence of the diffuser results in an increased power coefficient. These researchers have based their analyses on the area of the rotor diameter other than on the area of the outer diameter. The

demonstrations of performance gain in relation to bare turbines have been questioned by some researchers. They argue that renormalizing the power coefficient with the device outer diameter reduces it below the BJL. Hence, the upper bound to the amount of power augmentation possible is yet unknown as of to date which is part of what this research will try to answer.

Studies on bi-directional diffuser tidal turbines showed that no research outcome on turbine performance has outperformed conventional turbines. However, tidal devices developers have claimed that duct devices have hydrodynamic superiority, better yawed flow condition and a low cost of maintenance relative to the bare turbines. As a result, the duct concept has emerged as the preferred design in tidal stream technology with different geometries continued to be investigated in the search for a suitable duct shape that may prove to be competitive to cost of energy thereby making them commercially viable.

Although developers detailed data are usually commercially confidential and therefore are not made available to the public domain. However, the provision of funding to tidal industries poses a threat to development and commercialization relative to another renewable resource despite its uncommon potential. Recently, EMEC announced the decision by Naval Energies to liquidate OpenHydro.

The literature surveyed further revealed that the actuator disk approach and CFD-BEM model are the most frequently employed in turbine performance analysis with little experimental studies on the ducted tidal device available in the literature. However, It was identified for tidal energy study, the performance of devices are greatly affected by increasing blockage, turbulence, drag, discrete number of blades, blade tip loss and wake swirl.

A new type of duct (wind-lens) equipped with a flange at the periphery of the diffuser exit has shown that an average of about 18% additional wind speed increment resulted inside the duct compared to a diffuser without a flange. It was also shown that the presence of a diffuser proved to effectively improve the performance of the tidal turbine by a factor of 2.5 compared to the bare turbine. There is no study on the hydrodynamic and wake nature of diffuser with a flange to quantify the effect of such a system on power production in marine current energy studies. Thus the novelty of the present research is to quantify the effect of a duct equipped with a flange in tidal power production.

The year 2017 has highlighted a promising sign to the optimism and industrial developmental efforts gained in the commercialisation of tidal and wave energy technology. Multiple tidal stream converters in arrays have been identified to be critical to trimming costs down and commercialisation. The layout of such arrays is site-specific as several factors determine inter-device spacing: flow field generated by the MCT devices, water-depth constraints, turbulent mixing, lack of field data and environmental impacts. Turbine layout configuration approach in either regular or staggered configuration and inter-spacing between generators remains an active research focus as there is still much to learn about inter-row spacing in optimizing array layout. Although some experimental data exists for the wake of a single tidal stream rotor, limited data is available concerning the performance and wakes of multiple ducted tidal turbines. The key research focus of this study is to assess flanged ducted tidal power augmentation and wake characterisation of single row and in-line configurations numerically and experimentally.

CHAPTER THREE

Numerical Method

In this chapter, the fundamental governing equations of fluid dynamics are presented followed by a detailed description of the numerical development.

3.1 Numerical Approach

In the subsequent sections, the fluid dynamics fundamental governing equations were stated followed by the explanation of the Actuator Disk theory. The Reynolds-average Navier-Stokes equations were derived and discussed with respect to turbulence modelling. Overview of the CFD tool is presented and finally, descriptions of open channel flow and assumptions for modelling free surface effect for tidal turbine

3.1.1 Governing Equations

The properties and motion of fluid dynamics are describable with the fundamental governing equations of fluid dynamics. They are represented with three mathematical statements of conservation laws of physics:

- Mass conservation (i.e., what flows in must flow out)
- Momentum conservation (i.e. Newton's second law applied to a continuum)
- Energy conservation

The derivation of these equations and their explanations can be seen in many texts, an example is Davidson (2015). These equations are summarised as the Navier-Stokes equations and the continuity equation. The former is derived from the principle of conservation of momentum applied to a fluid particle that is subjected to inertial effects, while the latter arises from the principle of conservation of mass, Newton's second law and energy conservation. The ratio of the inertial effects on the fluid to the viscous effects (flow friction) is characterized by the dimensionless quantity called Reynolds number, Re . In the present study, heat transfer is

negligible and the flow is an incompressible fluid. Thus, the problem reduces to continuity and momentum equations, eqs. (3.1) and (3.2) respectively and are written in the tensorial form:

$$\frac{\partial u_i}{\partial x_i} = 0 \quad (3.1)$$

$$\frac{\partial u_i}{\partial t} + \frac{\partial(u_i u_j)}{\partial x_j} = -\frac{1}{\rho} \frac{\partial p}{\partial x_i} + \nu \left(\frac{\partial^2 u_i}{\partial x_j^2} + \frac{\partial^2 u_j}{\partial x_j \partial x_i} \right) + \frac{1}{\rho} f_{M,i} \quad (3.2)$$

where x_i is the i – th spatial dimension, u_i is the i – th component of velocity, ρ is the fluid density, t is time, ν ($= \mu/\rho$) is the kinematic viscosity (μ is the dynamic viscosity) and $f_{M,i}$ is the momentum source in the i – th direction. In steady flow cases, the first term in the momentum equation is identically equal to zero. The equations are for laminar flows. For turbulent flows, Reynolds-averaging is conducted, and the resulting equations will be closed in many forms. These equations are a system of dependent non-linear partial differential equations in which no analytical solutions exist (Wendt, 2009) and thus, they must be solved numerically. Details about the Reynolds-averaging and turbulence modelling is described in section 3.1.4.

3.1.2 Actuator Disk Model

Linear actuator disk theory has been the basic theory for the analysis of rotors and propellers. Its development can be traced back to Betz and Joukowsky in 1920. It is developed from Bernoulli's principle for a steady, inviscid, incompressible and irrotational flow and the turbine modelled by a disk with a streamtube flow in an axial direction. The flow within the streamtube does not interact with fluid around it and its direction is along one dimension (say x-axis as indicated in Figure 3.1) perpendicular to the boundary. Thus, there is a conservation of mass rate flow at any position along the streamtube. While there is a pressure difference just before and after the disk, the pressure far upstream and far downstream is considered equal to the static pressure of the freestream. The pressure difference is caused by the rotor disk as it extracts kinetic energy from the fluid flow. Considering that the fluid is incompressible, the energy extraction results in a decrease in the velocity of the fluid creating a decelerating velocity gradient in the fluid flow

within the streamtube, the streamtube expands giving rise to the static pressure increase. The static pressure drops below the ambient atmospheric pressure as the fluid flows across the disk.

The axial points indicated in Figure 3.1 are explained below as:

- Point 1 represents the far upstream region. The flow is not affected by the presence of the disk and the flow parameters are said to be at the freestream and are defined as u_0, p_0, A_0
- Points 2 and 3 are the regions just before and after the disk respectively. The flow velocity at these points is continuous and the cross-sectional area is equal to the area of the disk but there is a discontinuity in pressures across the disk. Thus, the flow parameters at these points are defined as $u_2 = u_3$ denoted as u_t , $A_2 = A_3 = A$; p_2 and p_3 .
- Point 4 is the region far downstream of the turbine and has ambient or freestream pressure as point 1. The velocity of flow and cross-sectional area of the turbine are defined as u_4 and A_4 .

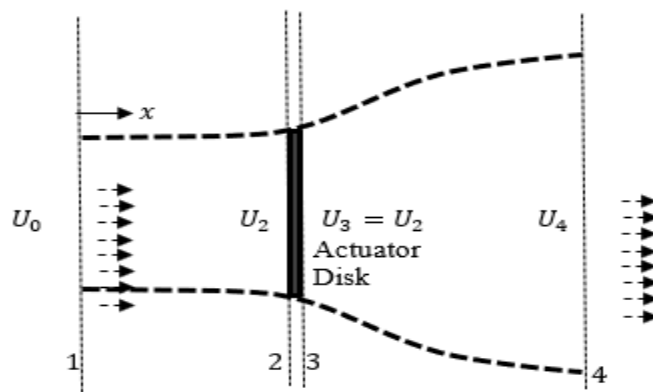


Figure 3.1. The Actuator Disk Model within a streamtube.

The discontinuity of the pressure at the actuator disk acts as an external force to extract axial momentum as well as energy. However, the declaration of continuous flow along the streamtube demands an increase in pressure following Bernoulli's equation. The mass flow rate, \dot{m} along the streamtube must remain invariant according to Betz is given by

$$\dot{m} = \rho u_0 A_0 = \rho u_t A = \rho u_4 A_4 \quad (3.3)$$

The axial velocity attenuation at the entrance of the streamtube and across the turbine disk, where a is the axial flow induction factor, is given by

$$u_t = u_0(1 - a) \quad (3.4)$$

The thrust force, T of the turbine disk is also given in terms of momentum flux and in terms of the pressure difference Δp at the actuator disk that produces the force as

$$-T = \dot{m}(u_4 - u_0) \quad (3.5a)$$

$$T = \Delta p A = \rho A(u_0 - u_4)u_0(1 - a) \quad (3.5b)$$

The Bernoulli equation for the upstream, using the definitions of the flow parameters at various points, is

$$p_0 + \frac{1}{2}\rho u_0^2 = p_2 + \frac{1}{2}\rho u_t^2 \quad (3.6)$$

And for the downstream, the Bernoulli equation is

$$p_3 + \frac{1}{2}\rho u_t^2 = p_0 + \frac{1}{2}\rho u_4^2 \quad (3.7)$$

Subtracting the upstream and downstream Bernoulli equations will result in

$$\Delta p = p_2 - p_3 = \frac{1}{2}\rho(u_0^2 - u_4^2) \quad (3.8)$$

Substituting Eq. (3.8) into Eq. (3.5b) gives

$$u_4 = u_0(1 - 2a) \quad (3.9)$$

Equations (3.4) and (3.9) show a proportionate attenuation in the axial velocity at the upstream and downstream. These equations are useful in the definition of the two dimensionless factors, the thrust, C_t and the power C_p coefficients that serve as measures of the turbine force and power extracted from the disk respectively. They are solely dependent on the induction factor and are given as

$$C_t = \frac{\text{force acting on the turbine}}{\text{upstream kinetic pressure force}} = \frac{T}{\frac{1}{2}\rho Au_0^2} = 4a(1 - a) \quad (3.10)$$

$$C_p = \frac{\text{power extracted from fluid}}{\text{power available for extraction}} = \frac{Tu_t}{\frac{1}{2}\rho Au_0^3} = 4a(1 - a)^2 \quad (3.11)$$

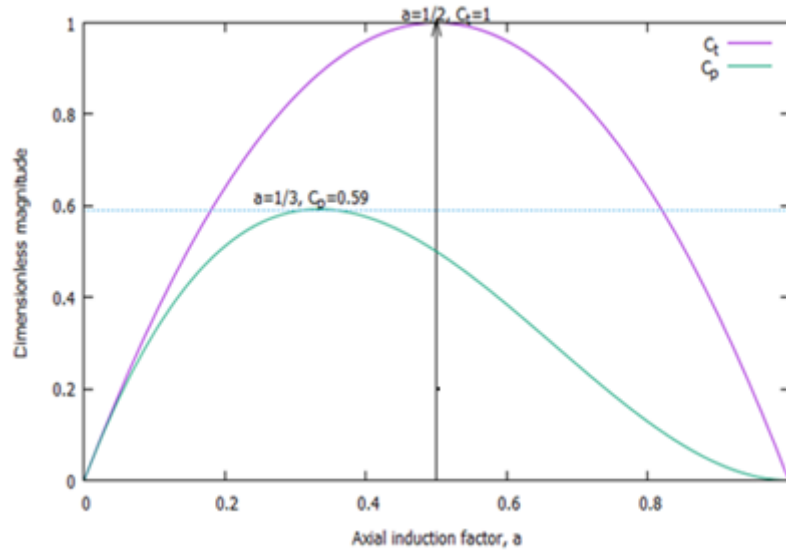


Figure 3.2. Theoretical plot of C_t and C_p against a .

Figure 3.2 indicates the BJL, the maximum thrust and power coefficients for an unconfined system. The thrust coefficient C_t has a parabolically symmetric at about $a = 0.5$, corresponding to a maximum $C_t = 1$, which enables the rotor thrust to gain equality with the dynamic pressure force of the disk. The power coefficient, C_p peaks at about 0.59 for axial induction factor of $a = 1/3$ contributing to a harvest of about 59 per cent of the kinetic energy of the fluid flowing along the streamtube.

It is pertinent to recall that the streamtube is an idealization that enabled the application of mass, momentum, and energy conservation laws for the description of actuator disk theory modelled as a porous disk within the assumptions made. This simplification is different from reality where flows around discrete blades are more swirled, complex, and decelerated creating streamwise velocity discontinuity inside and outside the streamtube. The actuator disk has the characteristics of attenuating the linear momentum which has been shown numerically and physically through

the actuator disk, making it possible to extract linear momentum as well energy from the flow like a physical rotor would do. Thus, it finds application in modelling wind turbines (Abe & Ohya, 2004), in tidal energy research (Shives & Crawford, 2011; Belloni et al., 2013; Fleming & Willden, 2016) and numerical investigation rotors with discrete blades (Gaden & Bibeau, 2010). Furthermore, the actuator disk model has the further edge in terms of device design over a discrete blade in that, irrespective of the complexities of flow, the dynamics can be well represented via actuator disk with negligible cognizance to the discrete blade and angular momentum effects but takes a harvest of the linear momentum.

3.1.3 CFD Software

The solver employed for this study is the non-commercial CFD tool- OpenFOAM (Open-Source Field Operation and Manipulation) window version 17.06. The uniqueness of OpenFOAM is that it offers users the possibility to easily create and extend the existing functionality. The overview of the OpenFOAM structure is described in Figure 3.3. OpenFOAM operates in 3D by default but can be instructed to solve a 2D problem by specifying an empty boundary condition on boundaries normal to the third dimension for which no solution is needed. The pre-processing data (mesh, fields, properties, control parameters, etc.) needed to start a simulation are stored in a set of files within a case directory, unlike other CFD packages. The basic OpenFOAM directory structure is described below.

- Zero directory

In this folder, the initial values and boundary conditions are specified for velocity, U , pressure, p , turbulent viscosity, ν_t , specific kinetic energy, k , turbulent specific dissipation, ω etc.

- Constant directory

This directory stores the polyMesh from the mesh generated. It also contains files specifying properties like transportProperties (kinematic viscosity) and turbulenceProperties.

- System directory

This folder contains setting parameters associated with the solution procedure and includes: controlDict where run control parameters are set e.g., start/end time, time step and parameters for data output; fvScheme where discretization schemes are specified; fvSolution where equation

solvers, tolerances and other algorithm controls are set; createBaffles contains the command that makes internal faces into boundary faces without duplicating any point etc.

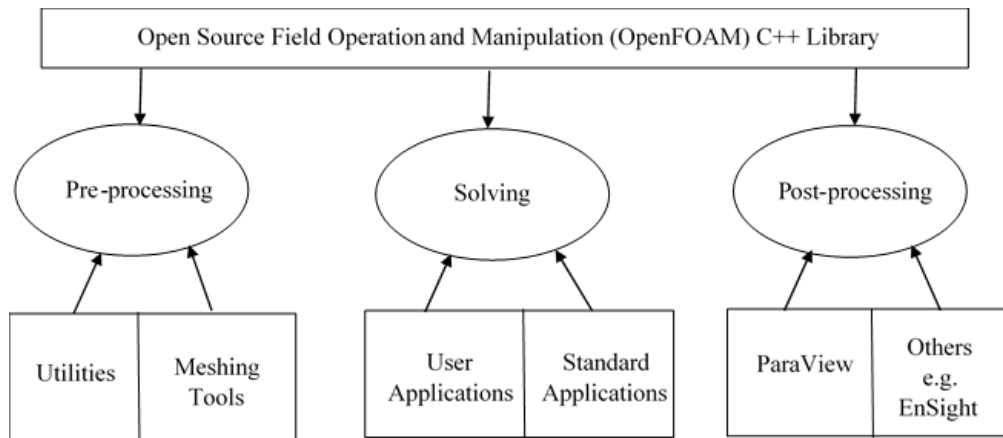


Figure 3.3. Overview of OpenFOAM structure (Greenshields & OpenFOAM, 2016).

The robustness of OpenFOAM for engineering problem analysis has been extensively studied in the literature. Lysenko et al. (2013) investigated turbulent flow separation over a planar bluff-body using OpenFOAM and ANSYS FLUENT. The authors' results showed that there is minimum deviations between the two CFD tools and they agreed fairly well with experimental data and other numerical solutions. Robertson et al. (2014) carried out verification and validation study for bluff-body fluid flows using OpenFOAM. The study identifies a second-order linear upwind scheme as the most efficient and accurate for Reynolds-average Navier-Stokes (RANS) simulations and it outperformed FLUENT in delta wing vortex breakdown predictions. Liu et al. (2016) investigated the instability and sensibility analysis of flows in OpenFOAM applying direct and adjoint Navier-Stokes equations linearized around a base flow. The study revealed that only a few minor modifications in the source code are enough for OpenFOAM solver to carry out global instability analysis of 3D flows in engineering applications.

3.1.4 Turbulence Modelling

There are two distinct types of flow, namely laminar flows (or streamline flows) and turbulent flows. Laminar flows occur when fluid flow in parallel layers, with no disruption between the layers while turbulent flow regime is characterized by rapid changes in pressure and velocity in

time and space. The Reynolds number quantifies whether a flow is laminar or turbulent and is defined as

$$Re = \frac{\text{inertial force}}{\text{viscous force}} = \frac{uL}{\nu} \quad (3.33)$$

where L is the characteristic length of the flow. Thus, turbulent flows associated with tidal stream turbines are characterized by high Reynolds numbers and low Reynolds numbers describe laminar flows.

The numerical solution of the Navier-Stokes equations for turbulent flow is extremely difficult and due to its inherent chaotic nature requires very fine grids to resolve all turbulent scales and fine resolution in time (Direct simulation). To counter this, decomposition of the instantaneous variables, velocity components and pressure, into a mean value and a fluctuating value is preferred. The resulting equation is referred to as the Reynolds-average Navier-Stokes (RANS) equation and is the most commonly employed in CFD for modelling turbulent flows. For this purpose, we divide the total flow into an average, \bar{u}_i and a fluctuating component, \bar{u}'_i as

$$u_i = \bar{u}_i + \bar{u}'_i \quad (3.34a)$$

$$p_i = \bar{p}_i + \bar{p}'_i \quad (3.34b)$$

Applying Eqs. (3.34a) and (3.34b) into Eqs. (3.1) and (3.2) give the Reynolds-average Navier-Stokes (RANS) equation

$$\frac{\partial \bar{u}_i}{\partial x_i} = 0 \quad (3.35)$$

$$\rho \left(\frac{\partial \bar{u}_i}{\partial t} + \frac{\partial (\bar{u}_i \bar{u}_j)}{\partial x_j} \right) = \frac{\partial}{\partial x_j} (-\bar{p} \delta_{ij} + 2\mu \bar{S}_{ij} - \rho \overline{u'_i u'_j}) + \rho \bar{f}_i \quad (3.36)$$

Where f_i denote the external body-force term, μ is the dynamic viscosity, and \bar{S}_{ij} is the mean rate of strain tensor given by

$$\bar{S}_{ij} = \frac{1}{2} \left(\frac{\partial \bar{u}_i}{\partial x_j} + \frac{\partial \bar{u}_j}{\partial x_i} \right) \quad (3.37)$$

The term $\overline{u'_i u'_j}$ in Eq. (3.36) is called the Reynolds stress tensor and represents the correlation between fluctuating velocities. It is an additional stress term due to fluctuations in velocity and is unknown. The Reynolds stress tensor needs to be modelled to close Eq. (3.36). This is called closure problem i.e., unknown variables is more than the number of equations i.e., ten (three from velocity components, pressure and six from stresses) to four (continuity equation and three components from the Navier-Stokes equations). To approximate these fluctuations in velocity turbulence models are introduced. These models are classified into two- eddy viscosity models and Reynolds stress models. In the Reynolds stress model, all stresses are solved directly, and they are not widely used due to the complexity associated with the model while eddy viscosity models are widely used as they require one or two transport equations and are implemented in most numerical codes such as OpenFOAM to solve engineering problems.

In eddy viscosity turbulence models, the Reynolds stresses are related to the velocity gradient through the turbulent viscosity. This relation is called the Boussinesq assumption and is given as

$$\overline{u'_i u'_j} = \frac{2}{3} \rho k \delta_{ij} - \frac{1}{2} v_t \left(\frac{\partial u_i}{\partial x_j} + \frac{\partial u_j}{\partial x_i} \right) \quad (3.38)$$

The term $\frac{2}{3} \rho k \delta_{ij}$ is required by tensorial algebra purposes when solving a turbulence model with the turbulence kinetic energy, v_t are the turbulent viscosity (or eddy viscosity) and k is the turbulent kinetic energy given by

$$k = \frac{1}{2} \overline{u'_i u'_i} = \frac{1}{2} (u'_i + v'_j + w'_j) \quad (3.39)$$

Eddy viscosity models are categorized based on the number of transport equations solved to obtain v_t and are as follows:

- Algebraic (or zero-equation) turbulent models

These models do not put into consideration the transport effects of turbulence and are only suitable for simple shear-layer dominated flows. The two well-known zero-equation models are the Baldwin-Lomat model and the Cebeci-Smith model.

- One-equation turbulent models

In these models, one turbulent transport equation usually the turbulent kinetic energy is introduced which is its only advantage over the zero-equation models (rather than using a mixing-length scale). The turbulent length scale l is the only unspecified part of the model. Examples include the Baldwin-Barth model and the Spalart-Allmaras model. However, for it to be implemented in separated flows, a model in which the transport effects on turbulence length scale are also accounted for is preferred.

- Two-equation turbulent models

These models are the bedrock of most of the turbulence model research and compute not only the turbulent kinetic energy, k but also the turbulence length scale, l . They are said to be complete. In other words, these models can be used to predict the properties of a given turbulence flow with no prior knowledge of the turbulence structure (Wilcox, 1998). To complete closure of the turbulent kinetic energy, k , equation, a second transport equation is needed and is model specific. One of the most popular models employed is the dissipation rate of the turbulent kinetic energy, ε , called $k - \varepsilon$ model and the second is the specific dissipation rate of turbulent kinetic energy, ω , called $k - \omega$ model. For details of available turbulence models in the CFD tool used in this study- OpenFOAM, see Greenshields and OpenFOAM (2016) and a comprehensive description of turbulence modelling for CFD (Wilcox, 1998).

The turbulence model employed in all simulations in this study is the $k - \omega SST$ (shear-stress transport) model developed by Menter (1994) by modifying the $k - \omega$ model of Wilcox to account for the transport principal turbulent shear stress with respect to dependency on freestream values of k and ω . The well-known separation prediction capabilities in adverse pressure gradients, as generally expected along the entire duct surface (Menter et al., 2003; Shives & Crawford, 2011), is the reason for choosing $k - \omega SST$ model in this present study. According to Menter (1994), $k - \omega SST$ model should be the model of choice for aerodynamic applications and the transport equations are given as

The turbulence specific dissipation rate, ω equation

$$\frac{\partial \omega}{\partial t} + \frac{\partial(\bar{u}_i \omega)}{\partial x_i} = P_\omega + \frac{\partial}{\partial x_i} \left[\left(\nu + \frac{\nu_t}{\sigma_\omega} \right) \frac{\partial \omega}{\partial x_i} \right] - \beta \omega^2 + (1 - F_1) CD_{k\omega} \quad (3.40)$$

The turbulence specific kinetic energy, k equation

$$\frac{\partial k}{\partial t} + \frac{\partial(\bar{u}_i k)}{\partial x_i} = \tilde{P}_k + \frac{\partial}{\partial x_i} \left[\left(\nu + \frac{\nu_t}{\sigma_k} \right) \frac{\partial k}{\partial x_i} \right] - \rho \beta^* \omega k \quad (3.41)$$

The production terms in ω and k are evaluated as

$$P_\omega = \alpha S^2 \quad (3.42)$$

$$P_k = \nu_t \left(\frac{\partial \bar{u}_i}{\partial x_j} + \frac{\partial \bar{u}_j}{\partial x_i} \right) \frac{\partial \bar{u}_i}{\partial x_j} ; \tilde{P}_k = \min(P_k; c_1 \beta^* \omega k) \quad (3.43)$$

The turbulence viscosity, ν_t is then obtained using

$$\nu_t = a_1 \frac{k}{\max(a_1 \omega F_{23} S)} \quad (3.44)$$

with

$S = \sqrt{2 \bar{S}_{ij} \bar{S}_{ij}}$, the invariant measure of the strain rate, and $CD_{k\omega} = \max\left(2\sigma_{\omega 2} \frac{1}{\omega} \frac{\partial k}{\partial x_i} \frac{\partial \omega}{\partial x_i}; 1.0e^{-10}\right)$, the positive portion of the cross-diffusion term.

The model coefficients are $\alpha_{k1} = 0.85$, $\alpha_{k2} = 1.0$, $\alpha_{w1} = 0.5$, $\alpha_{w2} = 0.856$, $\beta_1 = 0.075$, $\beta_2 = 0.0828$, $\gamma_1 = 5/9$, $\gamma_2 = 0.44$, $\beta^* = 0.09$, $a_1 = 0.31$, $b_1 = 1.0$ and $c_1 = 10.0$

with

The blending functions are defined as

$$F_1 = \tanh(\arg_1^4); \arg_1 = \min \left[\max \left(\frac{\sqrt{k}}{\beta^* \omega y}; \frac{500\nu}{y^2 \omega} \right); \frac{4\sigma_{\omega 2} k}{CD_{k\omega} y^2} \right] \quad (3.45)$$

$$F_2 = \tanh(\arg_2^2); \arg_2 = \max \left(\frac{2\sqrt{k}}{\beta^* \omega y}; \frac{500\nu}{y^2 \omega} \right) \quad (3.46)$$

accounting for switch formulation of the SST model between $k - \omega$ and $k - \varepsilon$ at the wall to the outer part of the boundary layer and outside of it and only on the boundary layer respectively. The term F_3 was later introduced by Hellsten, (1998) to account for roughness layer in rough wall flows and evaluated as

$$F_3 = 1 - \tanh \left[\left(\frac{150\nu}{y^2 \omega} \right) \right] \quad (3.47)$$

The performance of the $k - \omega SST$ turbulence model in predicting flow separation has been extensively studied in the literature. Apsley & Leschziner, (2000) investigated the capability of $-\varepsilon$, $k - \omega$ and $k - \omega SST$ turbulence models to predict different turbulent closures (linear and non-linear eddy viscosity models and differential models) in a 2D asymmetric diffuser. The $k - \omega SST$ model was found to correctly predict the general evolution of diffuser flow though at the expense of early separation. $k - \omega SST$ turbulence model is the most preferred turbulence model used as it has been used in several ducted tidal turbine studies (Shives & Crawford, 2011; Belloni et al., 2013; Fleming & Willden, 2016). A comprehensive summary on the superiority of $k - \omega SST$ turbulence model in predicting complex flows is presented in Shives and Crawford (2011).

3.1.4.1 URANS Model with $k - \omega SST$ Turbulence Closure

The flow field around a flanged duct turbine is characterized as a typical bluff-body flow field with highly complex and unsteady aerodynamic and/or hydrodynamic phenomena: separation and re-attachment of the shear layer along the internal walls of the duct, vortex shedding from the flange in the external flow around the duct and mixing of the internal and external flows at the outlet of the duct. One of the primary focuses of this study is to investigate the performance of flanged duct turbines under bi-directional flow and propose an optimum design. Noting that turbulence is a time-dependent 3D process whose computational simulation is particularly challenging. Among the two-equation RANS models based on Boussinesq approximation, the URANS model with $k - \omega SST$ turbulence closure was adopted in the present study. The $k - \omega SST$ model allows for direct integration through the boundary walls and shows superiority for wall simulation as previously stated. Although 3D LES (Large Eddy Simulation) or DES (Detached Eddy Simulation) is preferred to study the complex 3D flow around a bluff-body, Sun et al. (2009) demonstrated through simulation that 2D URANS solution contains 3D effect and is physical. Several other authors have extensively examined the practical applicability of the URANS $k - \omega SST$ approach. Sun et al. (2009) employed 2D URANS model with $k - \omega SST$ turbulence closure to predict the motion-induced aerodynamic forces of a rectangular section with $B/D = 4$ (where B is the cross-sectional width and D is the section depth) at a reasonable computational cost; also, the effect of the freestream turbulence was studied. A similar study was

carried out by Nieto et al. (2014) using OpenFOAM. Their result also proves that the 2D URANS model with $k - \omega SST$ turbulence closure can adequately model fluid-structure interaction responses, avoiding time-consuming 3D LES simulations or the development of in-house sophisticated software. Stringer et al. (2014) conducted URANS computations of flow around a circular cylinder for a wide range of Reynolds numbers. OpenFOAM was one of the solvers used. The simulation was 2D and the $k - \omega SST$ turbulence closure was employed. The computed results were close to the experimental data in terms of coefficients of lift, drag, and vortex shedding frequency at the subcritical Reynolds number range. Stringer et al. (2014) further suggested using pimpleFOAM, a solver capable of outer loop time-stepping may improve high Re convergence in OpenFOAM.

In the present research problem, the flow is generated by the actuator disk which creates a pressure drop across the disk. The effect of the duct is to divert more flow towards the disk. Flow separation and vortex shedding from the duct exerts a secondary effect on the flow through the disk. The URANS model with $k - \omega SST$ turbulence closure is considered to be a viable tool for the problem. However, the rotating part of the turbine can be more correctly simulated using a moving mesh approach embedded in the CFD model (e.g., PimpleDYMFOAM), to capture the intricate flow patterns around a wind-lens, such as the flow around the rotating blades, the flow separation at the blade trailing edge, and the blade tip vortices. Nevertheless, the actuator disk approximation used in the present CFD showed the computational results were typically in good agreement with the experimental data illustrated in Fig. 4.7. As a result, the present computational procedure is still very useful for the initial performance evaluation of a new profile of wind-lens turbine. Details about the model verification are described in Chapter Four.

In addition, the present computational procedure has been used to maintain an economical computational model (i.e., reduce model complexity which usually requires extremely large computational effort, large set-up time and being the preliminary design phase, a large number of cases and simulation iterations are required) while still being sufficiently accurate.

3.1.5 Open Channel Flow

An open channel flow describes the fluid motion in the free surface flow because its flow boundary is freely deformable, in contrast to the solid boundaries. Assuming steady flow, constant density and temperature, and from the extended Bernoulli equation, the mechanical energy per unit volume of fluid moving along a streamline, $u^2/2 + p + \rho gz$ is constant. Rewriting in terms of energy per unit weight of fluid, we have

$$\frac{u^2}{2g} + \frac{p}{\rho g} + z \quad (3.48)$$

where z is the height of the streamline above an arbitrary datum. For a channel of a small slope, Eq. (3.48) is simplified to

$$H = h_0 + \frac{u^2}{2g} \quad (3.49)$$

where h_0 is the static head and is the depth of the flow, and H is called the total head. This indicates that the total head (i.e., specific energy) is equal to the sum of the depth of water and the velocity head. By differentiating H by h_0 , the critical depth at which the specific energy is minimum for a given volumetric flow rate can be obtained. A dimensionless number describing this relationship is the Froude number. It is expressed as the ratio of the inertial to the gravitational force acting on the flow

$$F_r = \frac{u}{\sqrt{gh_0}} \quad (3.50)$$

The minimum energy flow occurs at $F_r = 1$ (i.e., critical flow). Flows at $F_r < 1$ are termed subcritical while at $F_r > 1$ is supercritical. In most natural and practical open channel flow conditions, the tidal flow is turbulent and tidal flows relevant for energy extraction are generally subcritical with F_r around 0.2. In the present study, F_r is less than 0.3.

3.1.6 Modelling Free Surface Effect for Tidal Turbines

Actuator disk models have been applied to tidal current turbines (Garrett & Cummins, 2007; Housby et al., 2008; Whelan et al., 2009). Garrett and Cummins (2007) considered a tidal turbine in a rigid-lid channel. Whelan et al. (2009) included the deformation of the free surface while Housby et al. (2008) carried out a similar analysis with the inclusion of downstream mixing unlike Whelan et al. (2009). Generally, the models assume that changes in the axial velocity of the flow dominate and that crossflow velocities may be neglected. Increasing blockage improves turbine performance, resulting in higher thrust and power coefficients over a larger range of tip-speed ratios (Garrett & Cummins, 2007; Housby et al., 2008; Whelan et al., 2009; Kolekar & Banerjee, 2015; Ross & Polagye, 2020). Whelan et al. (2009) obtained a good approximation for a highly blocked flow past tidal stream turbines near the free surface with the experimental tests. They concluded that agreement between the effects of free surface proximity and blockage with the experiment should improve further as the blockage is reduced. Consul et al. (2013) demonstrated that the effects of rigid-lid and free-surface deformation on the power of a crossflow tidal turbine to be negligible particularly for blockage conditions less than or equal to 0.25. Kolekar and Banerjee (2015) investigated the effect of blockage on turbine performance characteristics using CFD analysis. Results showed that turbine performance generally increases with increasing the blockage ratio. No blockage corrections are necessary for blockage ratios less than or equal to 0.11 when compared to the unblocked case. Also, the performance with tip-speed ratios less than 4 was found to be weakly dependent on the blockage ratio. For instance, as the tip-speed ratio increases from 1.46 to 2.93, a 6 per cent increase in C_p from blockage ratio of 0.042 to 0.42 was observed. However, the impact of blockage ratio on performance curves is significant with tip-speed ratios greater than 4. The peak C_p increased from 0.32 to 0.46 for the blockage ratio increased from 0.042 to 0.42. On the effect of boundary proximity, their experimental investigation suggested for optimum performance in a confined system, the turbine rotational disk should be at least one radial distance away from the solid channel wall and half radial distance below the free surface. Ross and Polagye (2020) experimentally examined the effects of blockage on the performance of a crossflow and an axial-flow turbine. Both turbines were characterized by conditions of high blockage and negligible blockage while other significant parameters were held approximately constant. Overall, the effects of increased blockage ratio increase the turbine's power performance just as in previous studies. However,

error associated with blockage corrections is turbine geometries or test conditions specific. In the present numerical simulation, the solver employed is OpenFOAM, a free Open-source CFD software package based on the finite volume method as presented in section 3.2.3. The turbine is modelled as an actuator disk, the swirl and shedding of coherent vortices from the blades are not accounted for. This assumption may not be accurate if the turbines are close together as interaction among turbines may exist due to the swirling motion of blades. More so, the inflow cross-sectional area is a circle, and the actual shape of the inflow cross-section is assumed unimportant. This requires that the cross-sectional area is significantly larger than the cross-sectional area of the rotor, and the effect of the free-surface boundary should not be important. To meet these conditions a relatively small blockage ratio is required. Nishino and Willden (2012a) showed that the influence of the aspect ratio is secondary to the blockage ratio when considering the efficiency of an array of turbines installed in a large rectangular tidal channel.

3.2 Chapter Summary

In this present study, we consider the incompressible flow which refers to a flow whose density remains constant in any fluid parcel, i.e., any infinitesimal volume of fluid moving in the flow. Then, the incompressible Navier-Stokes equations were described using the continuity and momentum equations. The resulting equations form a system of dependent non-linear partial differential equations in which (except few cases) no analytical solutions exist and thus, they must be solved numerically. Computational simulation of the hydrodynamic field around tidal turbines (or wind turbines) is particularly challenging and requires advanced numerical modelling to take into account turbulence and fluid-structure interaction. However, a simplified analytical approach such as the actuator disk theory can provide a good understanding of the flow field around horizontal axis turbines, as well as some useful preliminary results at the initial stages of design. Furthermore, the actuator disk model has the further edge in terms of device design over a discrete blade, in that, irrespective of the complexities of flow, the dynamics can be well represented via actuator disk with negligible cognizance to the discrete blade and angular momentum effects but takes a harvest of the linear momentum. The development of the actuator disk model follows Bernoulli's principle. With the assumption that the flow is a steady, inviscid, incompressible and irrotational flow, the turbine is modelled by a disk within a stream-tube flow in an axial direction. The flow within the streamtube is assumed not to interact with the fluid

around it and its direction is along one dimension (say x-axis) perpendicular to the boundary. Thus, there is a conservation of mass rate flow at any position along the streamtube. A pressure difference is caused by the rotor disk as it extracts kinetic energy from the fluid flow.

It was noted that the numerical solution of the Navier-Stokes equations for turbulent flow is extremely difficult and to resolve it, decomposition of the instantaneous variables, velocity components and pressure, into a mean value and a fluctuating value is preferred. The resulting equation is called the Reynolds-average Navier-Stokes (RANS) equation and is the most employed in CFD for modelling turbulent flows. In the present computational modelling, the solver employed for this study is the non-commercial CFD tool- OpenFOAM. Various approaches for solving fluctuations in velocity turbulent models were presented. Noting that one of the primary the focus of this study is to investigate the performance of flanged duct turbines under bi-directional flow and propose an optimum design. The flow field around a flanged duct turbine is characterized as a typical bluff-body flow field with highly complex and unsteady hydrodynamic phenomena: separation and re-attachment of the shear layer along the internal walls of the duct, vortex shedding from the flange in the external flow around the duct and mixing of the internal and external flows at the outlet of the duct. The two-equation RANS models based on Boussinesq approximation, the URANS model with $k - \omega SST$ turbulence closure was adopted. The $k - \omega SST$ model allows for direct integration through the boundary walls and shows superiority for wall simulation and is the most preferred turbulence model used as it has been used in several ducted tidal turbine studies. An open channel flow and assumptions for modelling the free surface effect for tidal turbines are highlighted. In most natural and practical open channel flow conditions, the tidal flow is turbulent and tidal flows relevant for energy extraction are generally subcritical with F_r around 0.2. In the present study, F_r is less than 0.3. The next chapter describes the computational domain and numerical model followed by model validations and presentation of simulation results.

CHAPTER FOUR

Numerical Results and Discussion

In the subsequent sections, the numerical computation domain is described followed by the model set-up and implementation of the actuator disk model in the present study. The schematic representation of the carefully chosen duct types is illustrated and described. Before performing the simulations, grid convergence tests and validation of the present model set-up were carried out and presented. A numerical simulation data set for the study of flanged ducted tidal stream turbines have been generated. The CFD simulation examined the behaviour of a single turbine equipped with a flanged duct for several carefully designed duct shapes in terms of performance and influence of blockage ratio. Then an optimum duct design was proposed.

4.1 Simulation Domain and Boundary Conditions

Many practical flow problems are situated in axisymmetric geometries and generally, for axisymmetric problems, the physical quantities vary only radially and axially and are, therefore, two-dimensional. As a result, for many of these practical applications, the transport equations are solved on a 2D or a thin wedge 3D computational domain in order to drastically reduce the computational effort as only a section of the flow is computed. In the present study, the prediction of performance parameters is the main goal, therefore, taking the axisymmetry of the computational domain and the channel containing the turbine, the simulations of the flow provided relatively adequate accuracy while maintaining an economical computational model i.e., reduce model complexity which usually requires extremely large computational effort, large set-up time and being the preliminary design phase, a large number of cases and simulation iterations are required. Also, this assumption implies that the effects of free surface deformation, supporting structure and channel cross-section are negligible. The turbine region is discretized by unstructured grids around the rotor and structured grids upstream and downstream of the turbine. With the domain size normalized by the turbine diameter, $D_t = 20m$, the inlet, and outlet were $5D_t$ upstream and $10D_t$ downstream of the duct respectively.

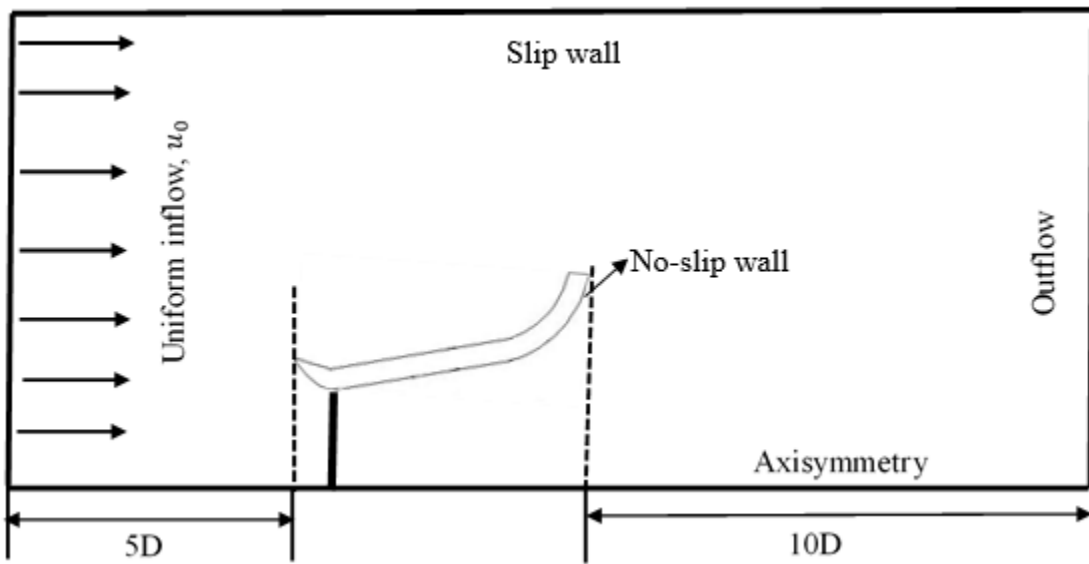


Figure 4.1. Computational conditions and boundary conditions.

Simulation results for the case with a longer domain length ($20D_t$) downstream of the duct are less than one per cent difference with the corresponding simulation results for the domain with $10D_t$ downstream length, so the use of $10D_t$ downstream length is deemed adequate for the present study (Figure 4.1). The boundary conditions used are constant velocity, $u_0 = 2.0\text{m/s}$ at the inlet, zero-gradient at the outlet, slip wall at the top, and no-slip wall with wall function treatment at the duct wall. The fluid is a water of density $\rho = 1000\text{kg/m}^3$ and kinematic viscosity $\nu = 10^{-6}\text{m}^2/\text{s}$, resulting in the Reynolds number $Re = 4 \times 10^7$ (length scale used is the turbine diameter, D_t). The freestream turbulence intensity (FST) of 10 per cent was used in computing freestream inflow turbulence parameters. The inflow turbulence parameters are calculated from

$$k = 1.5(u_0 I)^2 \quad (4.1)$$

$$\omega = \frac{k^{1/2}(0.09)^{-1/4}}{l} \quad (4.2)$$

where I is the turbulence intensity and l turbulent length scale ($= 0.1D_t$) similar to the work by Nishino and Willden (2012b) and Fleming and Willden (2016). Also, a low freestream turbulence intensity of 0.1 per cent was tested for the case of a bare turbine. Table 4.1 shows the details of the simulation scheme.

Table 4.1. Details of numerical simulation.

Computational grid	Mixed (structured and unstructured)
Scheme	Finite volume method
Time advancement method	Euler
Discretization of the convective term	2 nd –order upwind scheme
Coupling algorithm	pimpleFOAM
Reynolds number	4x10 ⁷

The blockage ratio was set at $\epsilon = 0.131$ unless otherwise mentioned for comparisons with previous works (Fleming & Willden, 2016). Figure 4.2 illustrates the definition of blockage ratio (ϵ) as implemented in the study. In the simulation, the outer rectangular region is replaced by a circular region of the same area as the simulation is axisymmetric.

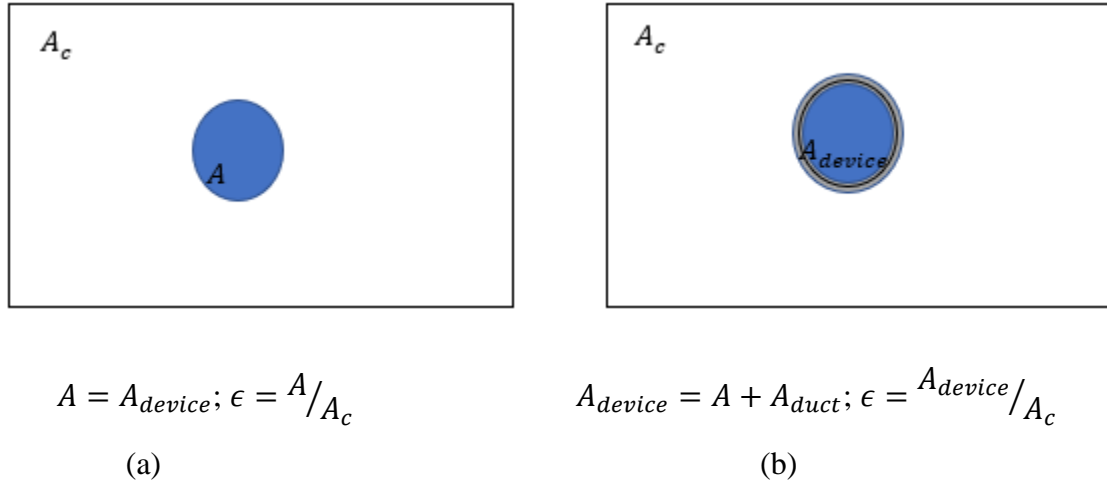


Figure 4.2. Blockage ratio, ϵ definition for (a) bare (b) ducted turbines.

4.2 Actuator Disk Implementation and Model Set-up

The turbine is treated as an actuator disk with the wake swirl and discrete blade effects neglected (Shives & Crawford, 2011; Belloni, 2013; Fleming & Willden, 2016; Rahman et al., 2018). In the numerical model, the axial resistance induced by the actuator disk was represented by a pressure drop Δp across the disk,

$$\Delta p = \frac{1}{2} \rho u_0^2 C_t \quad (4.3)$$

where C_t is a pressure coefficient or load coefficient, and Eq. (3.11) was simplified to

$$C_p = C_t \frac{u_t}{u_0} \quad (4.4)$$

where C_p is the power coefficient using the rotor area as the characteristic area; and u_t is the spatially averaged velocity at the rotor. Another power coefficient C_p^* can be defined using the area swept by the outer diameter of the duct A_{duct} given by

$$C_p^* = \frac{T A u_t}{\frac{1}{2} \rho A_{duct} u_0^3} \quad (4.5)$$

Equation 4.5 was further reduced to

$$C_p^* = \frac{A}{A_{duct}} C_p \quad (4.6)$$

In our numerical analyses as illustrated in Figure 4.2, we note that for bare turbine there is no duct and $A_{duct} = A$, $C_p^* = C_p$. The induction factor a is defined by

$$a = 1 - \frac{u_t}{u_0} \quad (4.7)$$

A negative value of a refers to the condition that the velocity of flow through the rotor is accelerated and greater than the ambient velocity. In OpenFOAM, the pressure-jump Δp in Eq. (4.3) is specified by using the utility function ‘createBaffles’.

As previously stated, the use of an actuator disk to simulate a turbine has the advantage that there is no need to resolve the blades explicitly and the number of grid points can be reduced significantly. Computational efficiency is important as there are a lot of scenarios to be simulated for various ducted turbines. The actuator disk imposes a streamwise resistance only and extracts the upper bound power from the flow. Additional losses due to swirl and shedding of coherent vortices from the blades are not accounted for. Furthermore, a specific rotor design may be required for each duct for optimum performance. For a fair and straightforward comparison of

duct performance, the assessment of the upper bound power extraction by the ideal rotor (actuator disk) is preferable. (Shives & Crawford, 2010; Fleming & Willden, 2016). All meshes were generated using Gmsh 3.0.6 (Geuzaine & Remacle, 2009) and imported into OpenFOAM using the conversion utility command, ‘gmshToFoam’.

4.3 Choice of Duct Shapes

Two types of ducts are carefully chosen. The first three ducts are of asymmetric shape (Type A, B, C) and the fourth duct is of symmetric shape (Type D), as shown in Figure 4.3. Asymmetric shape ducts are commonly used for a ducted turbine in unidirectional flow. Their performance in bi-directional (tidal) flow has however seldom been studied. Symmetric shape ducts are always used in bi-directional (tidal) flow as their performance is independent of the direction of flow. Type B is the design used in Ohya et al. (2008) for unidirectional flow. The vertical flange at the outlet is used to increase the suction in the wake and to generate a larger flow within the duct. This duct is primarily used for unidirectional flow but its performance in bi-directional (tidal) flow will be investigated. Type A is an improved design with a curved flange. It aims to produce better flow behaviour and less head loss under reversed flow conditions. For Type C duct, a small inlet-arc flap is added to improve the inlet flow condition and reduce the inlet head loss. Type D is symmetrical and consists of a Type A duct and its mirror image. Its performance will be identical for flow from both directions. In all cases, the duct thickness, $t = 0.025D_t$, rotor radius $r = D_t/2 = 10\text{m}$ resulting in $R/r = 1.31$ (where R is the duct radius) and position of the rotor $X/D_t = 0$. The geometric parameter of the duct is $L/D_t = 0.25$ and the flange length to duct diameter ratio is $h/D_t = 0.1125$. The inlet-arc flap length and height were set to $f = 0.05D_t$ and $h_f = 0.05D_t$, the length between the duct length and the flange periphery is $S = 0.125D_t$ (specifically for Type A and C duct types) and the inlet angle was set to $\theta = 4^\circ$. The choice of these values is based on a preliminary parametric study together with the results from previous works (Abe & Ohya, 2004; Ohya et al., 2008). Also, in the case with reversed flow direction, the flange height becomes $0.05D_t$, which falls within the recommended range of flange height of $0.04D_t \sim 0.06D_t$ by Limacher et al. (2020).

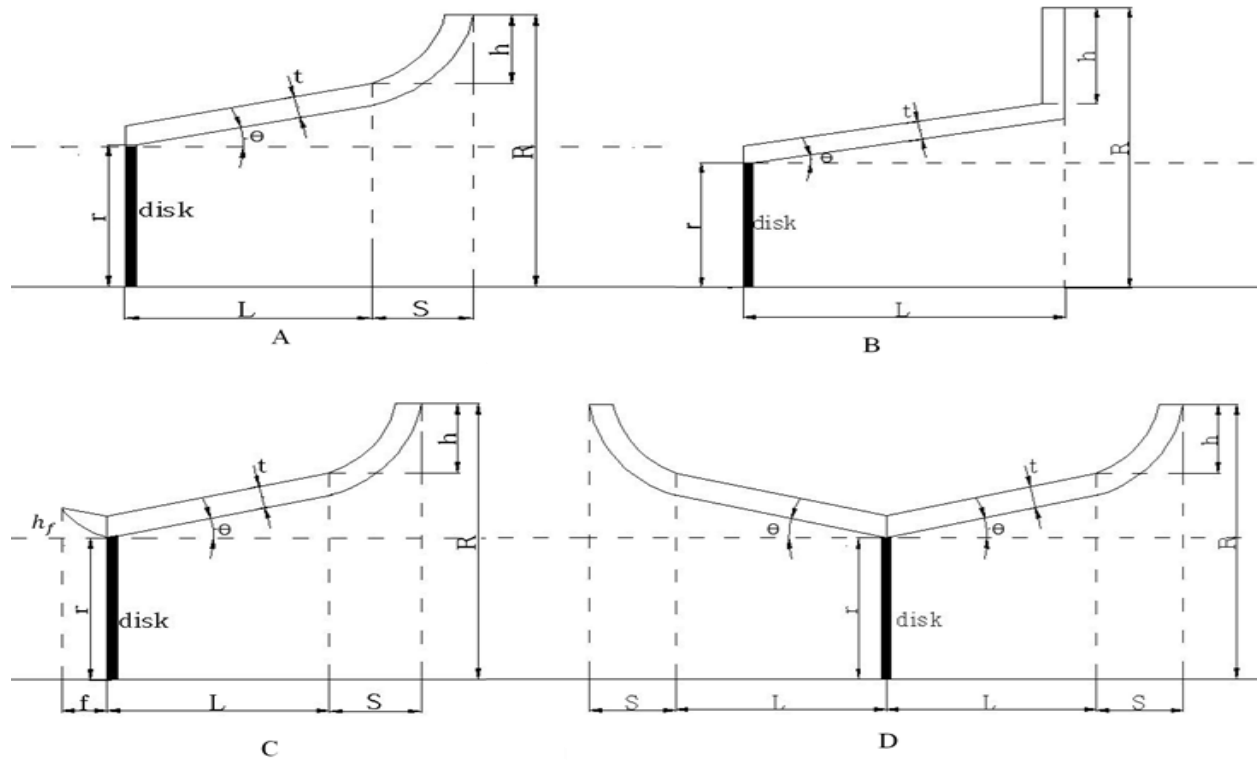


Figure 4.3. Duct geometries for cases with (A) curved flange (B) vertical flange (C) curved flange with inlet-arc flap (D) curved flanges at inlet and outlet. Not to scale.

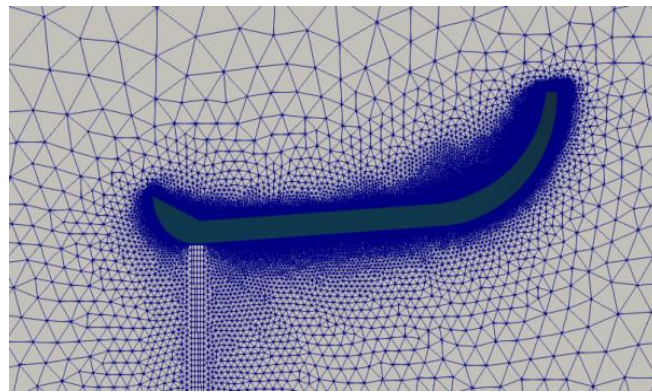
4.4 Mesh Definition and Grid Convergences

The grid used in the CFD simulation is carefully chosen to satisfy the wall function requirements. A typical grid layout used in the simulation is shown in Figure 4.4. Grid convergence tests following the procedures recommended by the Fluid engineering Division of ASME (Celik et al., 2008) have been conducted with Type C ducted turbine. Some details about the grids used and the computed results of interest, C_p (or C_p^*) are shown in Table 4.2. For wall function treatment (appropriate for high Reynolds number flow), the dimensionless distance, y_w^+ ($= u_\tau y_w / \nu$, where u_τ is the friction velocity, y_w is the normal distance to the wall, ν is the kinematic viscosity of fluid) in the range $30 \leq y_w^+ \leq 300$ was set.

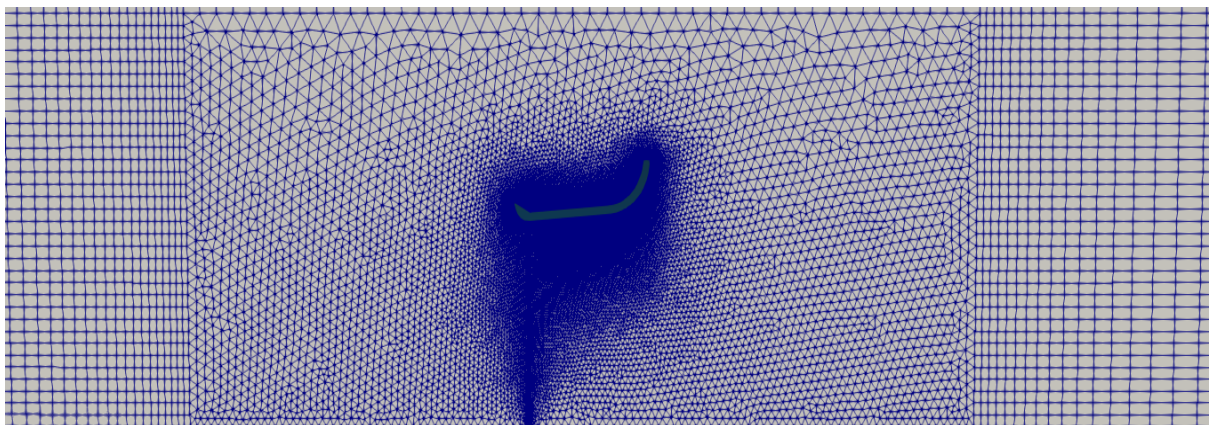
Table 4.2. Grid convergence tests for Type C ducted turbine (with $C_t = 1.05, L = 0.25D_t, h = 0.1125D_t, f = 0.05D_t, S = 0.125D_t$ & $\epsilon = 0.131$).

Grids	No of cells	C_p	C_p^*
Coarse	26172	1.3540	0.7886
Medium	104688	1.2521	0.7293
Fine	418752	1.2256	0.7139

For the solutions, the order of convergence was obtained to be approximately 2. The grid convergence index for the medium grid and the fine grid was computed to be 0.95%. Figure 4.5 shows the sensitivity of computed C_p with grid size. Since the objective is to select the most appropriate mesh that will give acceptable results in less computational time, the medium grid was used in the subsequent simulations.



(a)



(b)

Figure 4.4. Typical grid layout (a) around the duct and turbine (b) before and beyond the duct and turbine.

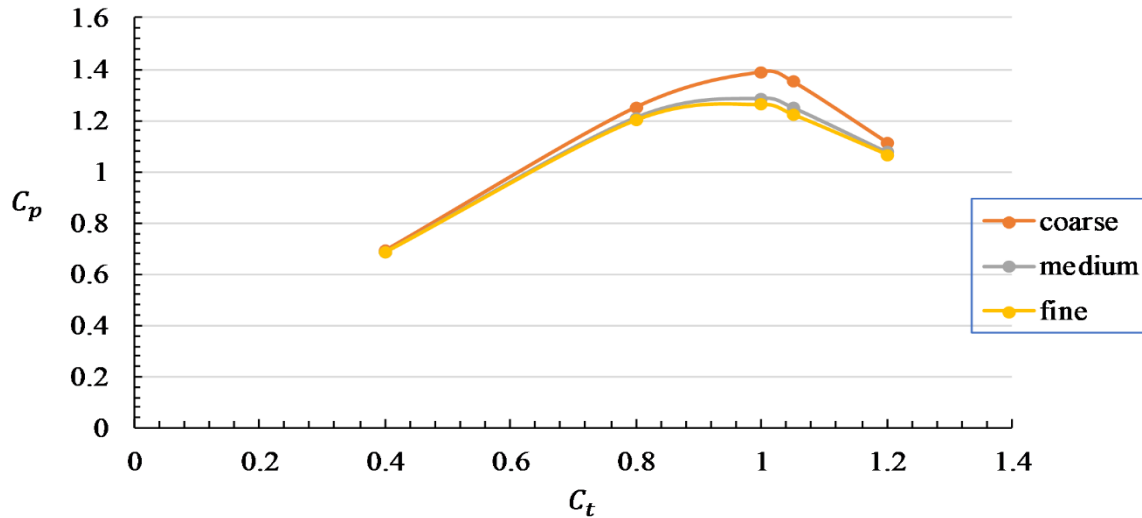


Figure 4.5. Sensitivity of C_p with grid size.

4.5 Initial Validation Studies

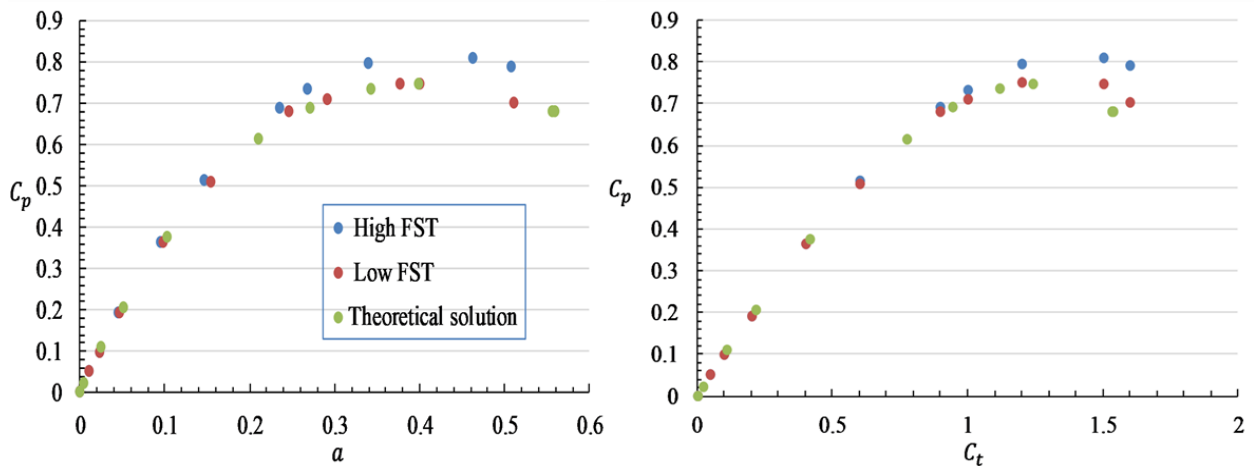


Figure 4.6. Effect of freestream turbulence on C_p with (a) a (b) C_t for a bare turbine with $\epsilon = 0.108$.

The first case is to simulate a bare turbine in a confined channel. The computed power coefficient, C_p is compared with the corresponding power coefficient obtained from the actuator disk theory under confined flow. For this purpose, the blockage ratio of the channel is set to $\epsilon = 0.108$ leading to $C_{p,max} = 0.7448$ (Garrett & Cummins, 2007). With all flow field residuals (velocity and pressure) set to 10^{-6} , the simulations were performed with a transient solver and proceeded with a time step size of 0.0001s. Results were then evaluated by comparing the time-

averaged flow fields and the value of the power output coefficients (Eqs. 4.5 & 4.6). The results are shown in Figure 4.6. It can be observed that the computed results for the low freestream turbulence (Low FST) case match the theoretical results closely. The increase of FST to 10% (High FST) increases the strength of turbulent mixing downstream of the turbine and increases the power generation and hence the coefficient C_p . In the present case with $\epsilon = 0.108$, the increase in the maximum power output is about 8%. The present actuator disk validation results are qualitatively similar to those of Fleming and Willden (2016).

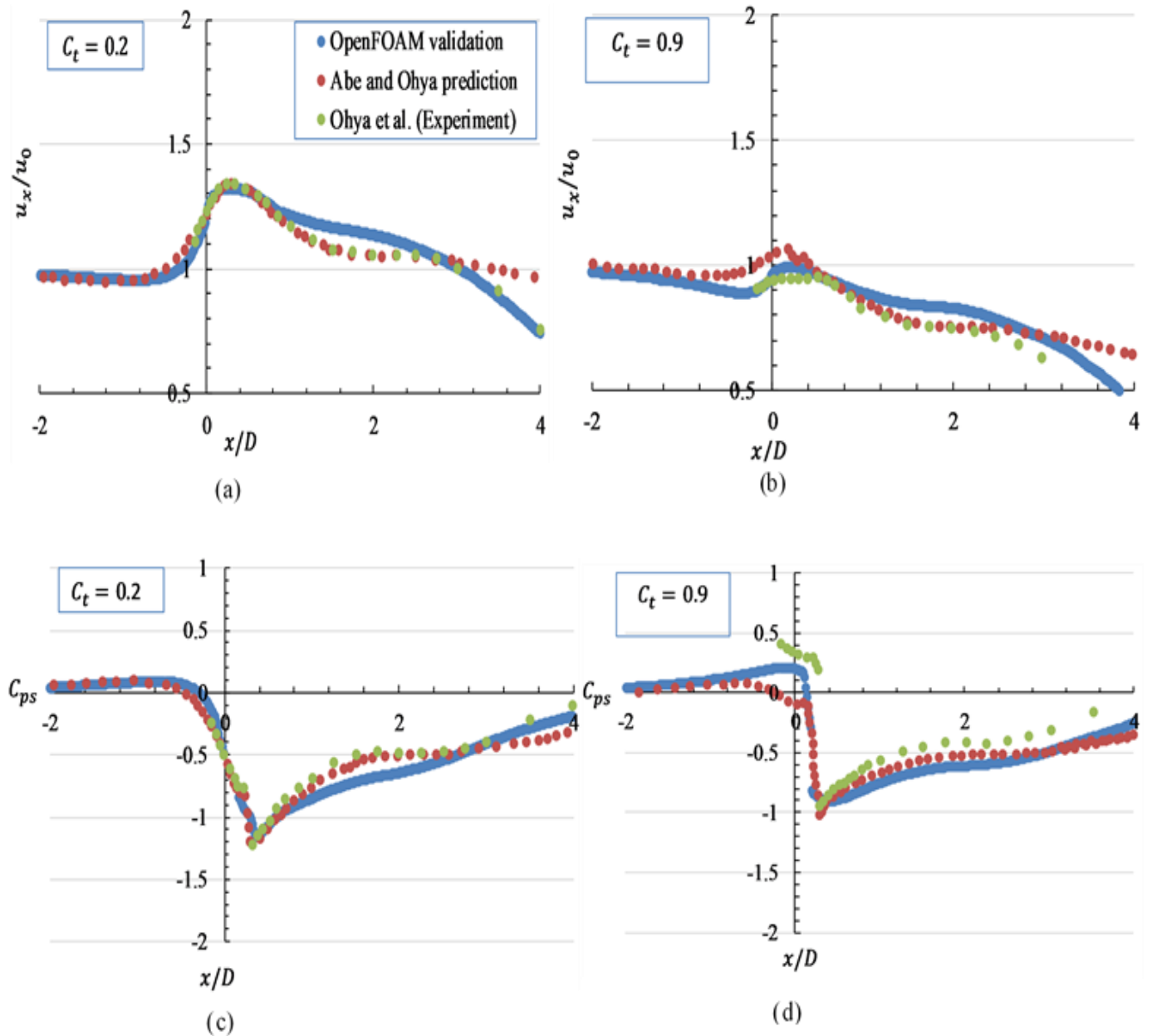


Figure 4.7. Axial distributions of streamwise velocity ratio (a) $C_t = 0.2$ (b) $C_t = 0.9$ and pressure coefficient (c) $C_t = 0.2$ (d) $C_t = 0.9$.

The model was then applied to simulate the flow through the wind lens of Abe and Ohya (2004), Type B duct in Figure 4.3, for two loading conditions: $C_t = 0.2$ and $C_t = 0.9$. The computed variations of pressure coefficient C_{ps} and normalized velocity profiles along the centerline are shown in Figure 4.7. The pressure coefficient is defined as $C_{ps} = (p - p_0)/(0.5\rho u_0^2)$, where p is pressure, and p_0 is the reference pressure of the approaching flow. It can be observed that the computed centerline pressure coefficient profiles and the computed centerline velocity profiles matched well with the corresponding experimental measurements by Abe and Ohya (2004). The present $k - \omega SST$ turbulence model predicted accurately the peak pressure coefficient and the peak velocity ratio for both cases, while the $k - \varepsilon$ turbulence model (Abe and Ohya, 2004) slightly overpredicted the peak velocity ratio and underpredicted the peak pressure coefficient for the case of $C_t = 0.9$. In the far wake region ($X/D_t > 3$) the decreasing trend before the recovery of pressure and velocity are predicted very well by the present $k - \omega SST$ model. In the near wake region ($X/D_t < 3$) the $k - \varepsilon$ turbulence model gives a better prediction of the profiles. The inaccuracies in the simulations may be due to the errors in the experimental measurements, the errors incurred in the turbulence models, and the errors in the grid discretization.

4.6 Numerical Analyses

The remaining sections will now analyse the data set arising from the CFD utilizing the actuator disk approach described and implemented above for analyzing power output and the influence of blockage ratio in detail.

4.7 Performance of Ducted Turbines with Ideal Rotor

Extensive CFD simulations have been carried out for the preliminary parametric study. The optimum geometrical parameters of the duct obtained are relisted here as above: $L/D_t = 0.25$, $h/D_t = 0.1125$, $f/D_t = 0.05$, $S/D_t = 0.125$, $\theta = 4^\circ$. The criteria for choosing this set of parameters are based on the power output performance and the practicability in the realization of the duct. Also, the effects of duct length and flange height variations for Type B duct have been previously reported in Abe and Ohya (2004). In all cases, the rotor area is the same, and

simulations are run at least for five different values of C_t . The power coefficients for the ducted devices are represented by C_p^* and C_p with different reference areas.

4.7.1 Performance of Turbines with Equal Frontal Area

The power coefficient C_p^* is plotted as a function of the axial induction factor, a and thrust coefficient, C_t for duct Type A, Type B, Type C, Type C (Reversed), Type D, and the bare devices in Fig. 4.8. It can be seen that the asymmetric duct design (C and reversed C) shows a significant improvement in power output reaching a peak value of approximately 0.8 compared to the bare device of about 0.85, whereas the symmetric duct Type D attains a maximum power output of about 0.5, which is similar to that obtained from the best performing symmetrical duct designs by Fleming and Willden (2016). This significant improvement achieved by the duct Type C design can be explained as follows: in a duct, the flow expands along the inside wall unless a massive flow separation occurs in the near-wall region. As a result, the pressure coefficient rises and then the velocity decreases toward the duct exit. Owing to this, the flow must accelerate in advance near the duct inlet to compensate for the deceleration inside the duct. Thus, the approaching flow accelerates as a result of the low-pressure region generated behind the flange and reaches its maximum velocity around the inlet region. Similarly, the deceleration mechanism inside the flanged duct means that the pressure coefficient inside the duct must return to a much lower value at the duct exit. Because of this restriction, the approaching flow must accelerate more to lower the pressure coefficient around the duct inlet. Hence, the significant power augmentation of duct Type C is due to (1) the curved nature of the device which was able to streamline the flow along the duct avoiding massive flow separation near-wall region (2) the curved nature of the inlet-flap forced more mass flow convergence into the duct (3) the curved flange generated a large separation behind it thereby inducing a low-pressure (suction) effect. Thus, this inherent simultaneous action of duct Type C led to a significant increase in flow swallowing and transmission capability of the duct entailing a larger low-pressure zone. This is clearly illustrated in Fig. 4.10(b,c,d,e). Duct Type A (with curved flanged but without inlet-flat) showed massive separation in the near-wall region but the presence of the curved flanged resulted in higher speed fluid flow around the disk compared to duct Type B with a vertical flange while duct Type C and C (Reversed) avoided mass flow separation and also have high

mass flowing fluid around the disk as they are equipped with curved inlet-flap and flange. The velocity field and pressure field of the flows are further discussed in section 4.8.

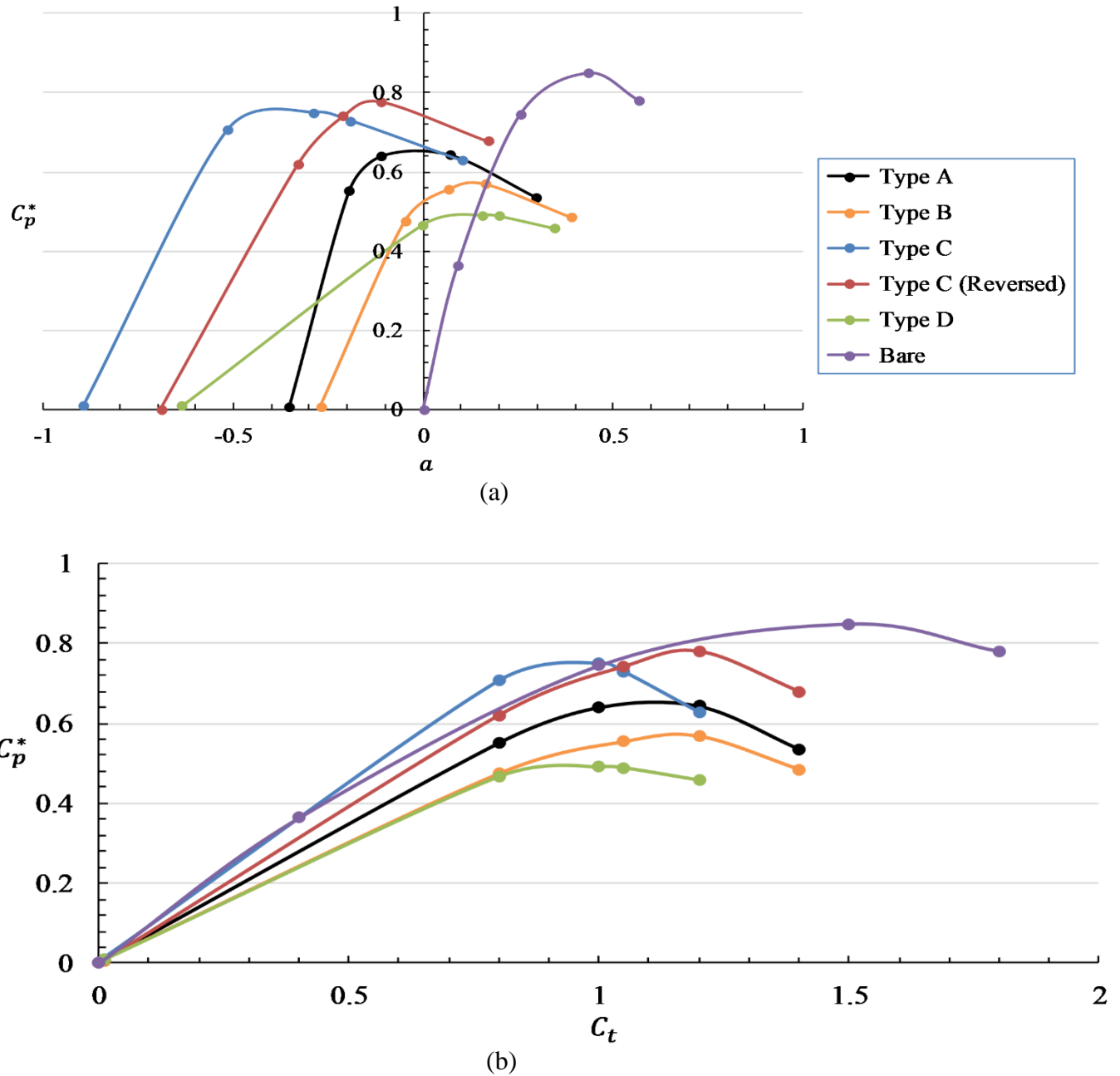


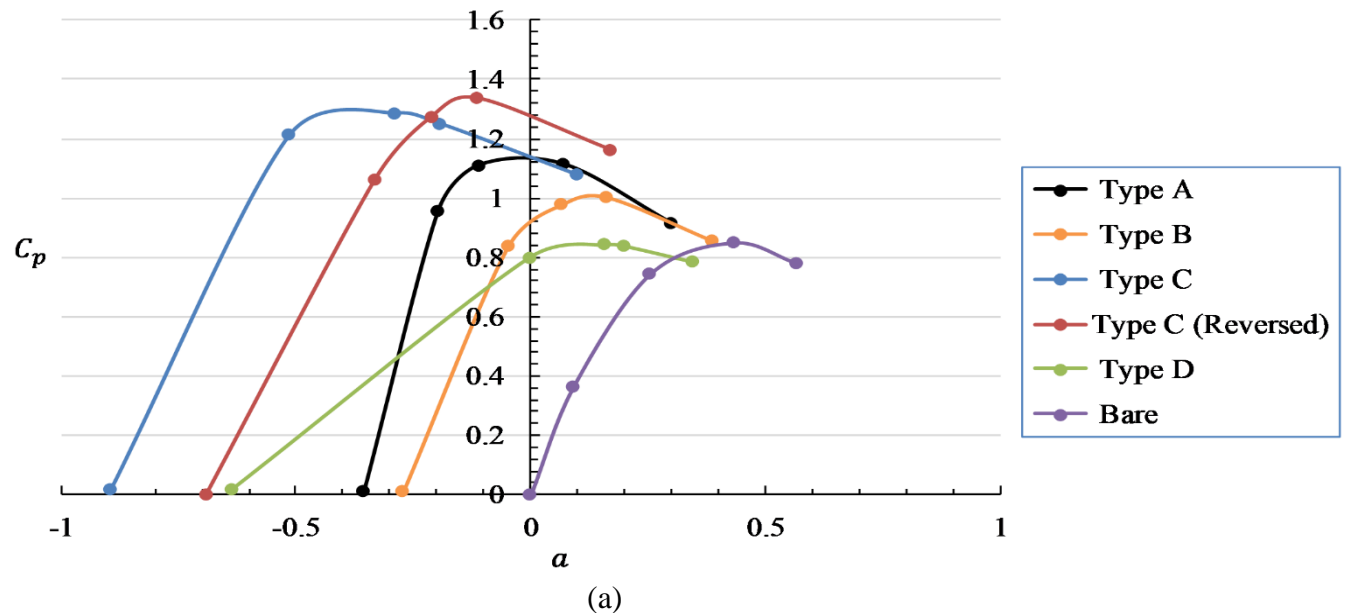
Figure 4.8. Variation of C_p^* with (a) a (b) C_t (C_t ranges from 0 to 2).

The optimal performance of this duct device is however achieved at lower loading conditions ($C_t < 1.2$) and decreases with C_t for C_t exceeding 1.2. This proves that the performance of a flanged duct is strongly influenced by whether or not there exists a separation inside the duct just

as found in previous studies (Abe & Ohya, 2004). In addition, the loading coefficient has a strong relationship with the generation of separation. Thus, at a relatively small loading coefficient ($C_t < 1.2$), avoiding a massive separation near-wall region tends to give high performance for a flanged duct turbine. At $C_t > 1.2$, massive flow separation occurs inside the duct device and the build-up of the recirculation region thereby limiting wake expansion.

4.7.2 Performance of Turbines with Equal Rotor Area

The variation of the power coefficient C_p (adopting the rotor area as the reference area) with the induction factor a and thrust coefficient, C_t are shown in Fig. 4.9. The peak C_p of type C ducted turbine is about 1.6 times that of the bare turbine while the peak C_p of the Type D symmetric ducted turbine is merely close to that of the bare turbine. The magnitude of the pressure gradient increases with the size of the flange up to a certain size. Further increase in flange size will introduce a blocking effect restricting the flow into the duct (Ohya et al., 2008). Therefore, C_p increases with flange size up to a certain value.



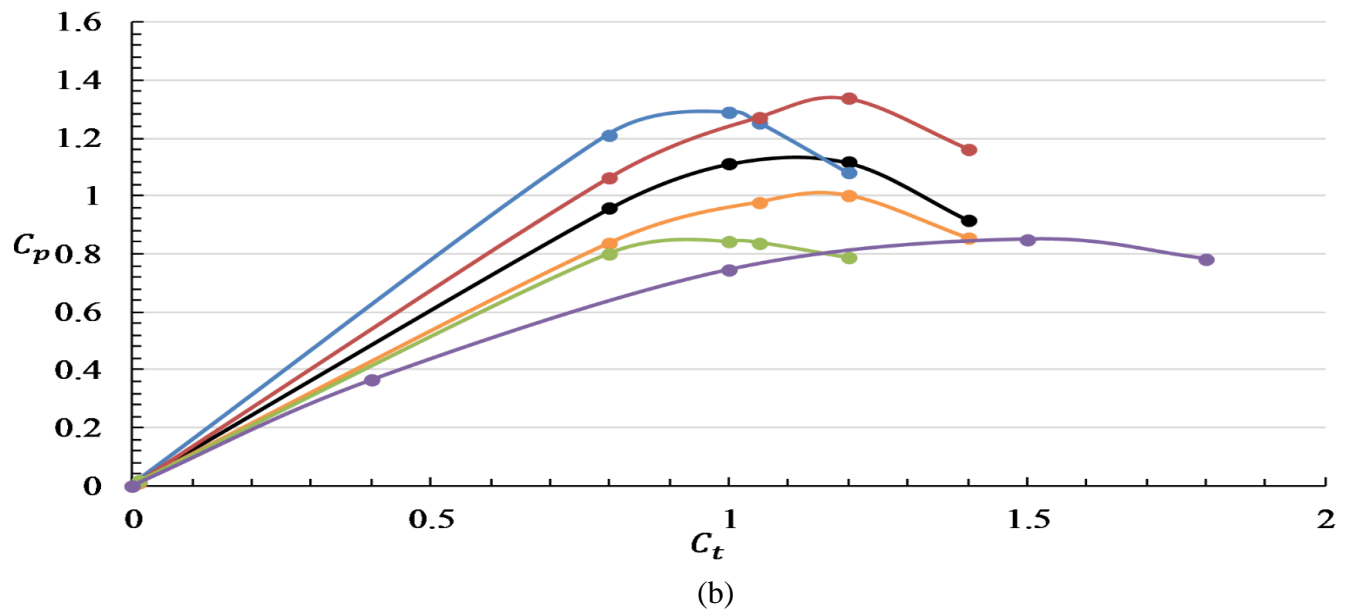


Figure 4.9. Variation of C_p with (a) a (b) C_t (C_t ranges from 0 to 2).

4.8 Flow Field Distributions of Turbines

To investigate the flow characteristics of various turbines, the computed flow streamline coloured with velocity normalized by the inflow velocity at or close to the maximum power output conditions are shown in Fig. 4.10. For the flow streamline integration over the domain, we were interested in illustrating features of the flow field distributions around the rotor, near-wall region and downstream of the flanged duct turbine. In all the cases, we used a total of 10,000 points (i.e., the number of points of integration) over the domain length for the streamlines to achieve a distinct visual description of the flow field. Similar upstream flow behaviour is observed for each of the devices. Differences arise as the incident flow impinges just on the rotor and downstream of the rotor. For the bare case, the velocity decreases as the flow approaches the rotor and gradually expands further downstream of the rotor wake (Fig. 4.10a). For Type A duct, flow recirculation from the flange occurs in the external flow. As a result, a high-speed flow develops just downstream of the rotor but is counteracted by boundary-layer flow separation along the internal walls of the duct. Further downstream, the high-speed flow quickly dies out forming a recirculation wake profile at a lower thrust coefficient ($C_t = 1.0$) and eventually expands (Fig. 4.10b). Similar to Type A duct, flow recirculation from the flange in the external flow occurs in Type B duct (Fig. 4.10c). Although no separation occurs along the internal walls of Type B duct, the Type A duct demonstrates the expanding curved flange not

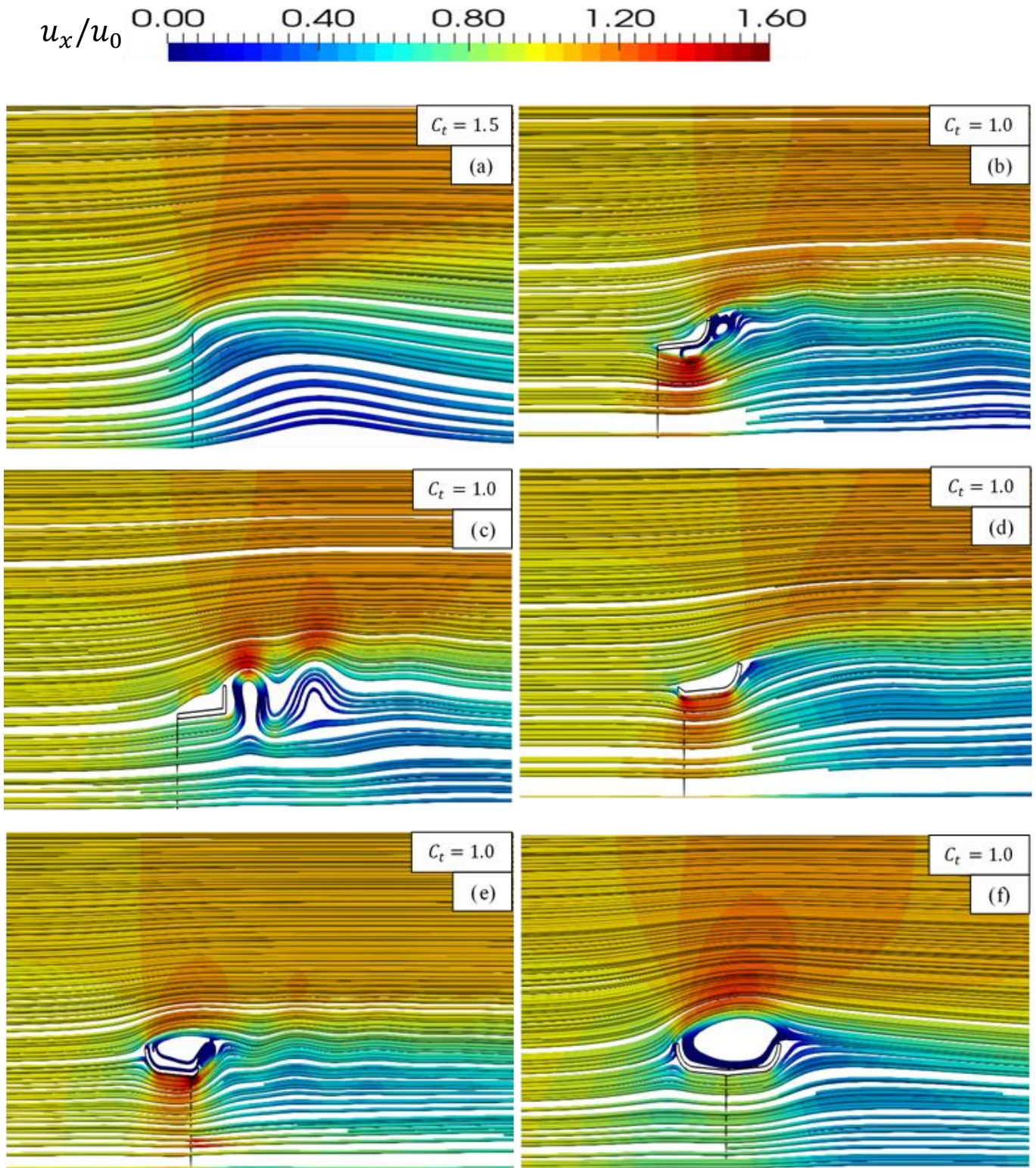


Figure 4.10. Flow streamlines for (a) Bare (b) Type A (c) Type B (d) Type C (e) Type C Reversed (f) Type D. Flow direction is from left to right.

only generates a low-pressure region behind the duct peculiar to flanged duct devices for increasing flow swallowing capacity but also align and channels the flow out of the duct, hence, a greater flow rate. This is a consequence of the increase in the aforementioned duct performance presented in Fig. 4.8 and 4.9. For Type C duct equipped with a curved inlet-arc flap ensures that no separation occurs along the inner boundary walls of the duct as it streamlined the flow into the rotor plane and along the duct walls. Also, the presence of the expanding curved flange at the periphery of the duct easily aligns and channels the flow out of the duct while still generating a low-pressure region behind the duct. This inherent simultaneous action led to a significant increase in flow swallowing and transmission capability of the duct entailing a larger low-pressure zone (Fig. 4.10d and Fig. 4.11d). A higher-speed flow concentration is seen around the rotor and downstream of the duct just before the duct exit, unlike Type B with a slightly less velocity spread around the rotor. Similar behaviour is observed in the reserved case (Type C Reversed) where the curved inlet-arc flap served as the duct flange (Fig. 4.10e). This further shows that a curved flanged type is preferred and hence, the best performing duct type (see Fig. 4.8 and 4.9). For the Type D duct, the front curved flange generates a large recirculation zone just outside the duct (Fig. 4.10f). The recirculation bubble diverts more flow outside the duct and results in a lower flow rate through the rotor. It should be noted that for the ducted turbines the peak power coefficient occurred at the loading condition with the thrust coefficient significantly smaller than that of a bare turbine. Also, the incorporation of the inlet-arc flap and the shape of the inlet-arc flap and flange is a strong determinant of the nature of the flow inside and around the duct and downstream.

The pressure fields of various ducted turbines at or close to the maximum power output conditions are shown in Fig. 4.11. For the bare case (Fig. 4.11a), a pressure rise occurs in front of the rotor. This limits the approaching flow (at zero pressure) through the rotor. For Type A duct (Fig. 4.11b), a slight pressure rise occurs in front of the rotor but is counteracted by the action of the curved flange which diverts more flow into the duct. For Type B duct (Fig. 4.11c), the pressure rise is of a lesser extent due to the vertical flange which creates a lower pressure zone downstream. For Type C (Fig. 4.11d), no pressure rise occurs in front of the rotor (unlike Type A) and a suction zone occurs just downstream of the rotor. A larger flow thus is resulted. For Type C reversed duct (Fig. 4.11e), a slight pressure rise occurs. This is counteracted by the action of the curved flange which diverts more flow into the duct. For Type D duct (Fig. 4.11f), the recirculation bubble just outside the duct is larger than that of Type C reversed. The

downstream part of the duct with curved flange shelters the rotor and causes the low-pressure zone to occur further downstream of the rotor, resulting in a lesser flow rate.

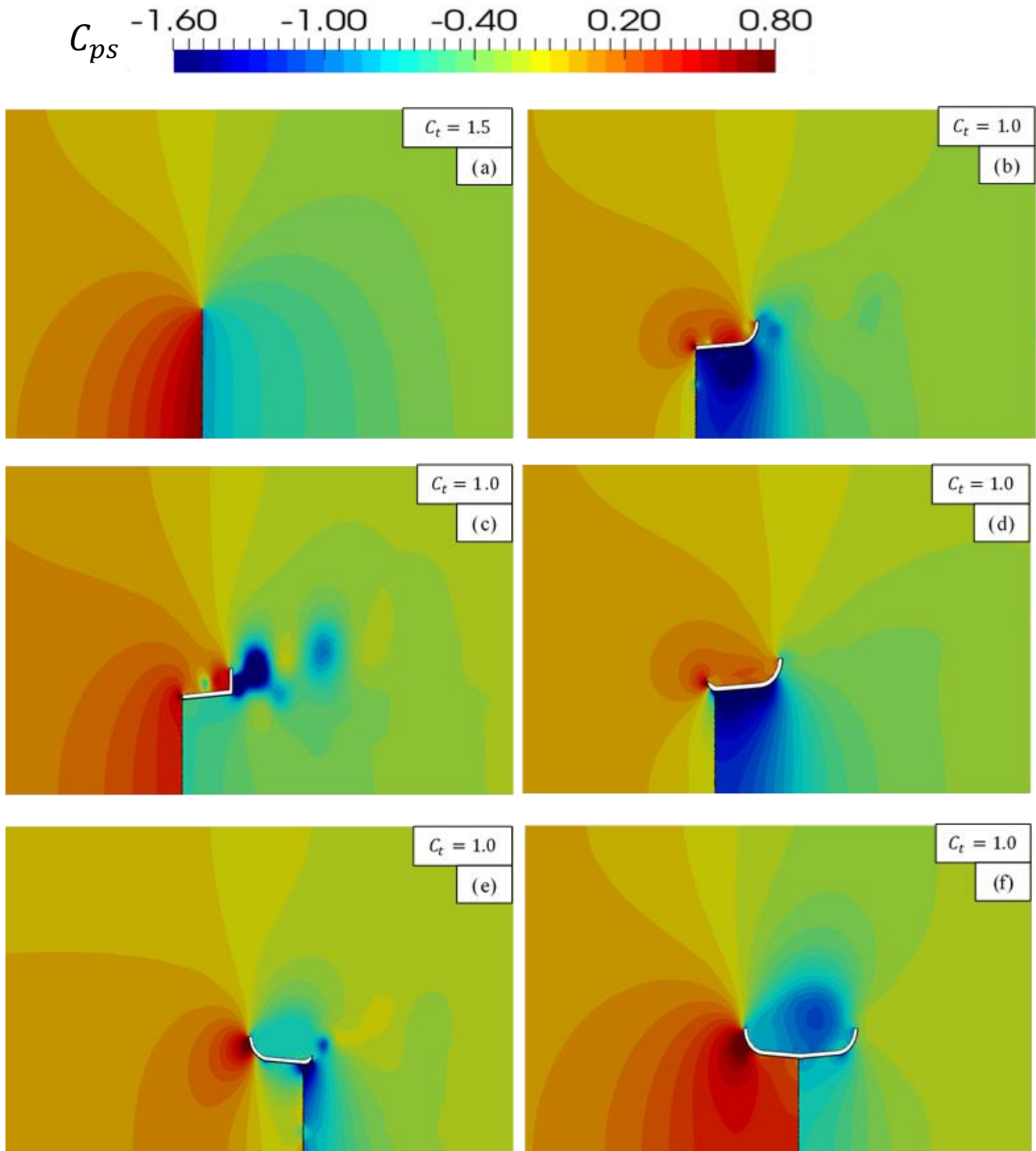


Figure 4.11. Pressure fields for (a) Bare (b) Type A (c) Type B (d) Type C (e) Type C Reversed (f) Type D. Flow direction is from left to right.

The variation of streamwise velocity ratio and pressure coefficient along the centerline for Type C and bare turbines are shown in Fig. 4.12. At the location of peak power coefficient, the pressure coefficient just downstream of the rotor is the lowest, corresponding to $C_t = 1.05$ for Type C duct, $C_t = 1.2$ for Type C reversed duct. A peak velocity also occurs just upstream of the rotor. When the loading condition shifts away from that producing the peak coefficient, the peak velocity decreases and can be lower than the approaching velocity (case with $C_t = 1.2$ for Type C duct), and also the value of the lowest pressure increase.

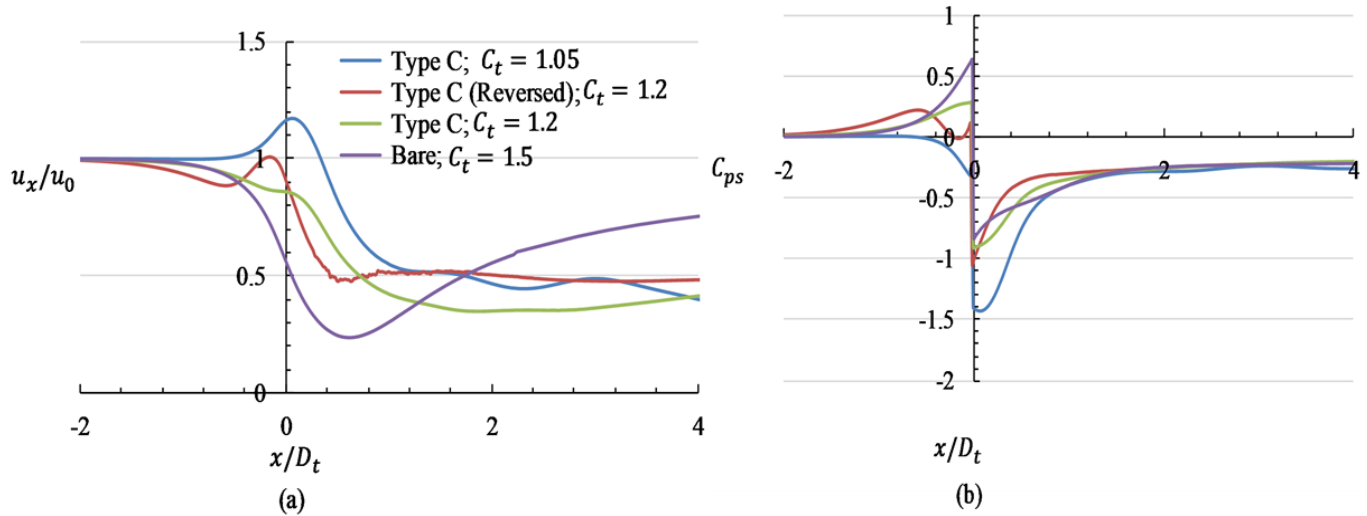


Figure 4.12. Axial distributions of streamwise (a) velocity ratio (b) pressure coefficient for bare and Type C ducted turbine.

4.9 Effect of Blockage Ratio

In placing arrays of turbines in a tidal channel more flow will be drawn into the turbines due to flow confinement from adjacent turbines. Garrett and Cummins (2007) have developed an analytical model to study the effect of flow confinement on the flow through a bare turbine. The effect of the blockage ratio on the peak power coefficient of the ducted turbines is studied by using CFD. Fig. 4.13 shows the variation of the maximum power coefficient (in terms of C_p^*) with the blockage ratio. As stated previously, the blockage ratio is defined to be the cross-sectional area of the rotor divided by the cross-sectional area of the flow bounded by adjacent turbines or solid boundaries. It is observed that the maximum power coefficient increases with

the blockage ratio and reaches a value of 0.78 when the blockage ratio is 0.131 (Garrett & Cummins, 2007). For a higher blockage ratio, the interaction between adjacent turbines may be significant and the inlet velocity may become nonuniform. This is beyond the scope of the study of the present work. In the present computation, the height of the channel is varied such that the required blockage ratio is achieved. The blockage ratio varies from 0.035 (relatively unblocked) to 0.131 chosen from related past studies (Belloni, 2013; Fleming & Willden, 2016). The results for Type C and Type D turbines are shown in Fig. 4.13.

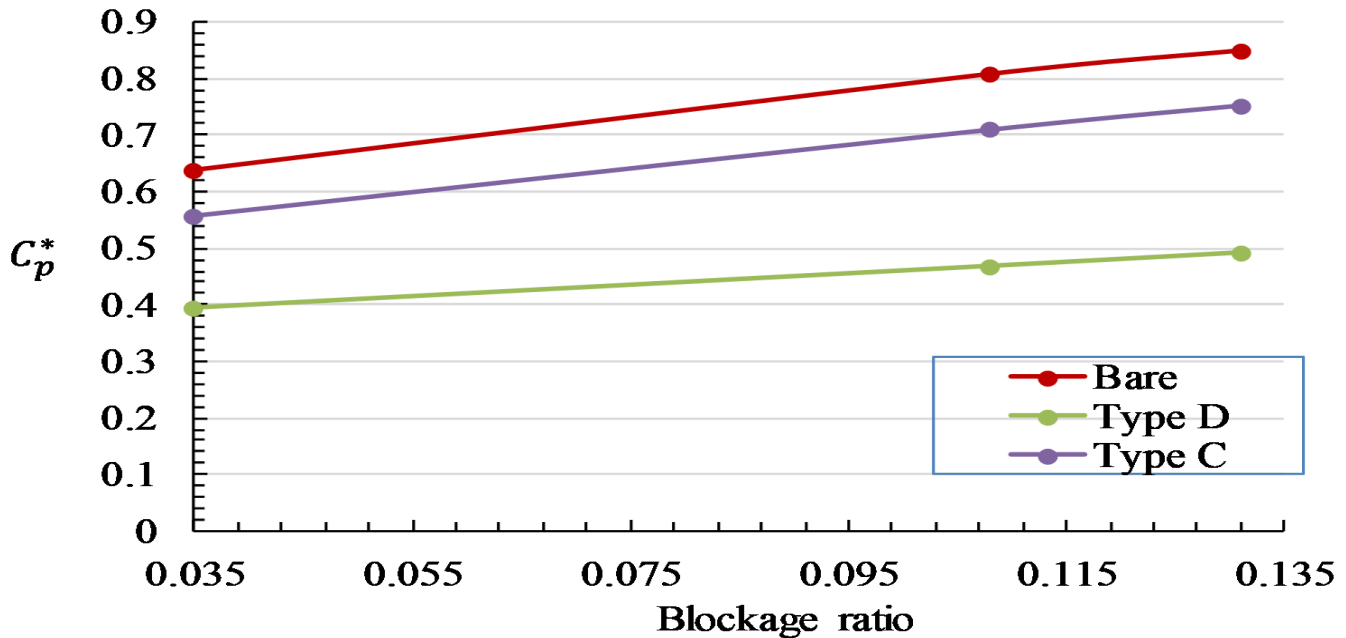


Figure 4.13. Variation of C_p^* with blockage ratio for bare, Type C, and Type D turbines.

In all cases the peak C_p^* increases with the blockage ratio. The bare turbine consistently gives the highest C_p^* for a given blockage ratio, as the rotor size is increased and set equal to the duct size for the other cases. The relative performance of duct turbines varies little with the blockage ratio, with Type D turbine giving the least rate. For Type C turbine, its C_p^* is 88% of the corresponding C_p^* of bare turbine over the range of blockage ratio covered. For Type D turbine, its C_p^* slightly varies from 62% of the corresponding C_p^* of bare turbine at blockage ratio 0.035 to 58% at blockage ratio 0.131. Additionally, the numerical simulations done by Limacher et al. (2020) are of blockage ratio approximately equal to 0.01 and the highest C_p^* obtained was 0.576. In our simulation results shown in Fig. 4.13, the highest C_p^* obtained at the blockage ratio of 0.035 is

0.56 for Type C ducted turbine. Therefore, our results are comparable and consistent with those of Limacher et al. (2020).

CHAPTER FIVE

Experimental Method

In this chapter, we present a detailed description of the experiments in this study, including the procedures, design, and set-up of the model turbines. The main objectives are to investigate the interaction effects between turbines in an array.

5.1 Experimental Approach

Installation and testing of large-scale prototypes of turbines to ascertain turbine performance and justify for long time investments are capital intensive. It has been previously established that multiple tidal stream converters in arrays have been identified to be critical to trim cost down (Goltenbott et al., 2017; Marine Renewables Canada, 2018). As tidal power plant installation sites are limited, installing multiple tidal stream converters in close proximity may significantly alter the operational conditions of the energy converters, which in turn affects their performance and durability. Also, full-scale tidal turbine construction and measurements at the tidal energy power sites can have a substantial negative impact on the surrounding ecosystem or marine life forms. Thus, experimental studies of model turbines in controlled environments e.g., laboratories will provide insights on the performance objectives of developed converter designs and wake characterisation arising from different array layout configurations and allow for a large unexplored parameter space for the design to be investigated.

Additionally, experimental data sets (power performance and wake characteristics) provide vital information needed for the validation of numerical models for the design and optimization of tidal energy converters in prototype scale projects. This is also important for the future development of technologies for marine energy utilization.

Experiments on flow through a micro-scaled (1:200th of a 20m diameter full-scale turbine) model turbine has been conducted in an open channel with water recirculating system housed in the Hydraulic Laboratory, Department of Civil and Environmental Engineering, The Hong Kong Polytechnic University, SAR, China. In the experiments, the interaction effects between flanged

ducted turbines or non-ducted turbines on their power performances and wake characteristics were examined in detail. Wake mapping was represented in terms of centerline, lateral (crossflow), and vertical profiles of velocity ratios and turbulence intensity.

In the subsequent sections, the experimental design and set-up of the model turbines used across all experiments are introduced. Test facilities configuration of the array of turbines used in the experiments as well as the flow measurement equipment, ADV and the data analysis procedure are outlined.

5.1.1 Model Design

The specific details of the micro-scaled model turbine are described in the following sections.

5.1.1.1 Blade Section Details

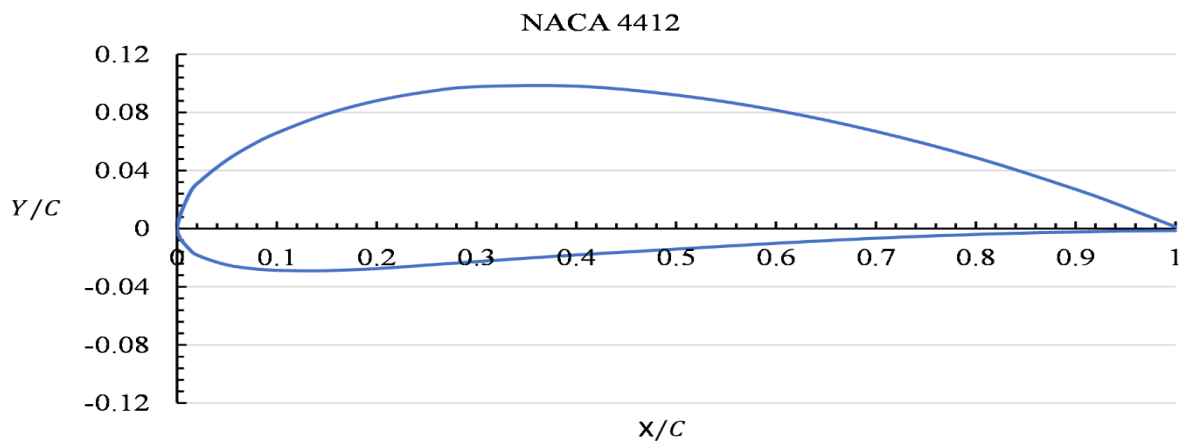


Figure 5.1. Cross-section of NACA 4412 airfoil.

It is well known that the NACA (National Advisory Committee for Aeronautics) airfoil series has been designed for aeronautical applications. Also, the wing sections now in common use are either NACA design or have been strongly influenced by the NACA investigations (Abbott & Doenhoff, 1959). The airfoil section of NACA 4412 is shown in Fig. 5.1. For the four-digit NACA airfoil section, the first digit is the maximum camber as a percentage of the chord, the second digit is the location of the maximum camber along the chord from the leading edge in

tenths of the chord, and the last two digits give the maximum thickness as a percentage of the chord (Anderson Jr, 2010). Pinkerton (1938) measured in considerable detail the aerodynamic properties of NACA 4412 section for Reynolds numbers (based on chord length, c) from 100,000 to 8,200,000. Results showed that the pressure distribution on NACA 4412 section is practically unaffected by the change in Reynolds number except at the location where there is a flow separation.

The aerodynamic properties of NACA 4412 airfoil section have been investigated using the flying hot-wire probe (Badran & Bruun, 2003; Al-Kayiem & Bruun, 1991; Nakayama, 1985; Wadcock, 1978). Adopting the flying X-hot-wire probe to measure the U and V components of the flow field over NACA4412 airfoil, Badran and Bruun (2003) presented mean flow and Reynolds stresses results, obtained on the centerline plane of the airfoil, covering the boundary layers over the upper surface, the potential flow region, and the wake downstream of the trailing edge at a 15° angle of attack (AoA). Their results showed that an intermittent reverse flow region occurred near the trailing edge of the airfoil and then swept away with the streamwise flow. The values of the Reynolds normal and shear stresses were shown to increase continuously when moving away from the surface with downstream distance, while in the wake region, relatively large values of Reynolds stresses occurred. The AoA of 15° corresponded to the position of maximum lift for a NACA 4412 airfoil section.

Chang (2004) carried out an experimental study to measure phase-averaged mean velocity and turbulent intensity in the near-wake region of an oscillating NACA 4412 airfoil at different Reynolds numbers. In all cases measured, the results of Chang (2004) showed that the velocity defects were coupled with both the camber effect and the Reynolds number effect and that the Reynolds number effect may be associated with the laminar or turbulent boundary layer on the airfoil surface. The near-wake characteristics of an oscillating NACA 4412 airfoil were showed to be insensitive at Reynolds numbers between $Re = 1.9 \times 10^5$ and 4.1×10^5 , while at $Re = 5.3 \times 10^4$ a velocity deficit of much larger in magnitude and width was observed. Also, in the range between $Re = 5.3 \times 10^4$ and 1.9×10^5 , a critical value of the Reynolds number existed, at which laminar separation or turbulent separation occurred in the near wake of an oscillating NACA 4412 airfoil.

Vardar and Alibas (2008) investigated the rotation rates and power coefficients of miniature wind turbine rotor models manufactured using NACA profiles. Their results showed that the NACA 4412 profiles with zero-grade twisting angle, five-grade blade angle, double blades had the highest rotation rate and a power coefficient of about 0.3.

Haque et al. (2015) carried out an experimental investigation to explore the possible improvement of the aerodynamic performance of airfoil by incorporating curvature at the leading edge of a NACA 4412 wing. In the experiment, a curvature was incorporated at the leading edge in such a way that the surface area from the middle of the wing towards the root increases and the area decreases towards the tip at the same rate while maintaining the overall surface area of the wing to that of the rectangular planform. From the analysis of their experimental data, it was observed that the lift coefficient of the curved leading-edge planform increases and the drag coefficient decreases at AoA below 12° in comparison to that of the rectangular planform.

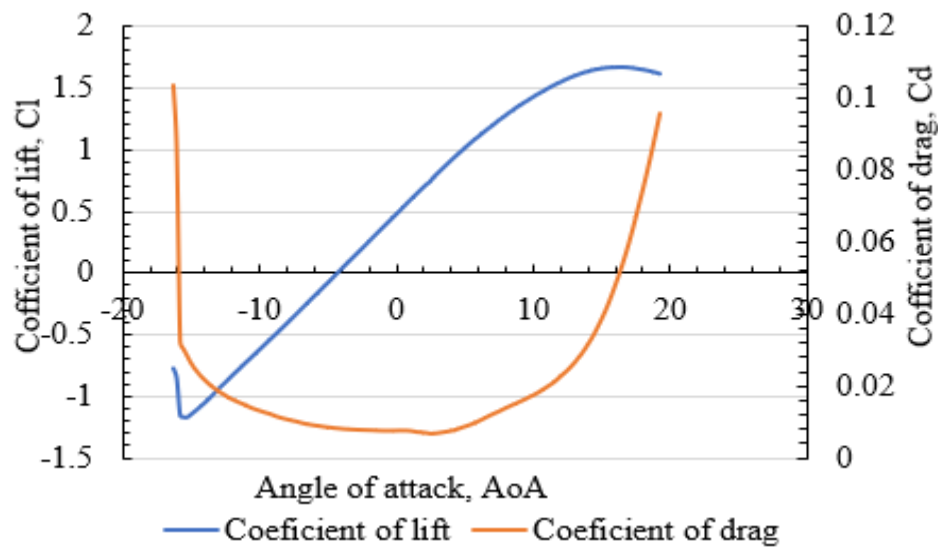


Figure 5.2. C_l and C_d vs AoA plots for NACA 4412 at $Re = 1 \times 10^6$.

The coefficient of lift, C_l and coefficient of drag, C_d , which illustrate the performance of a hydrofoil in a certain flow is presented in Fig. 5.2 against the angle of attack, AoA for NACA 4412 airfoil. The figure shows that from 0° to 15° there is a linear increase in lift and a relatively small increase in drag. A sudden steep increase in drag and a decrease in the lift are observed after 15° . At this angle, an aerodynamic stall is set in as separation occurs.

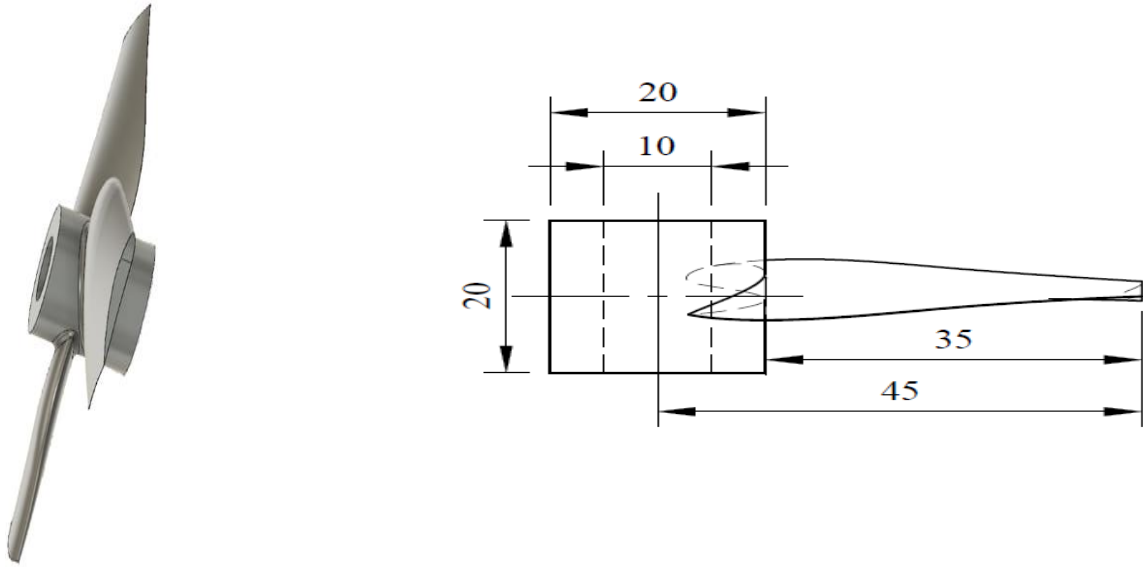


Figure 5.3. The sketch of blade and rotor (measurement is shown in $m m$).

In the present study, the design of blades is shown in Fig. 5.3 and is based on the NACA 4412 airfoil. The blades were located 120° apart (3 blades in total) on the rotor and were fabricated in-house from PLA (Polylactic Acid) filaments using a 3D printer. They were rubbed with sandpaper to improve smoothness and arrive at a more homogeneous distribution of surface roughness. The three-blade rotor was geometrically scaled to the diameter of the rotor, D_t of $0.09m$ and the key design parameters are blade height r_h , rotor radius r (i.e., total blade height, $D_t/2$), and twist angle (Fig. 5.4). The spanwise distribution of the airfoils is done at every 10% successive interval of the blade. The hub is of diameter $0.02m$ and the distance between the hub circle and the blade root is 22% of the rotor radius (r). The blade twist angle is designed to be higher at the root airfoil as it experiences fewer rotational forces on the blade and then gradually starts to decrease towards the entire span of the blade and zero twist at the tip. The hydrofoil cross-section profile is presented in terms of blade height-rotor radius ratio (r_h/r), chord length-rotor radius ratio (c/r) and blade twist angle distribution in Table 5.1. The length of the nacelle connected to the rotor is about $0.1m$. Although the model scale is small due to the limitation of the testing facility, the testing results are expected to be used as a reference for the design of prototype tidal turbines.

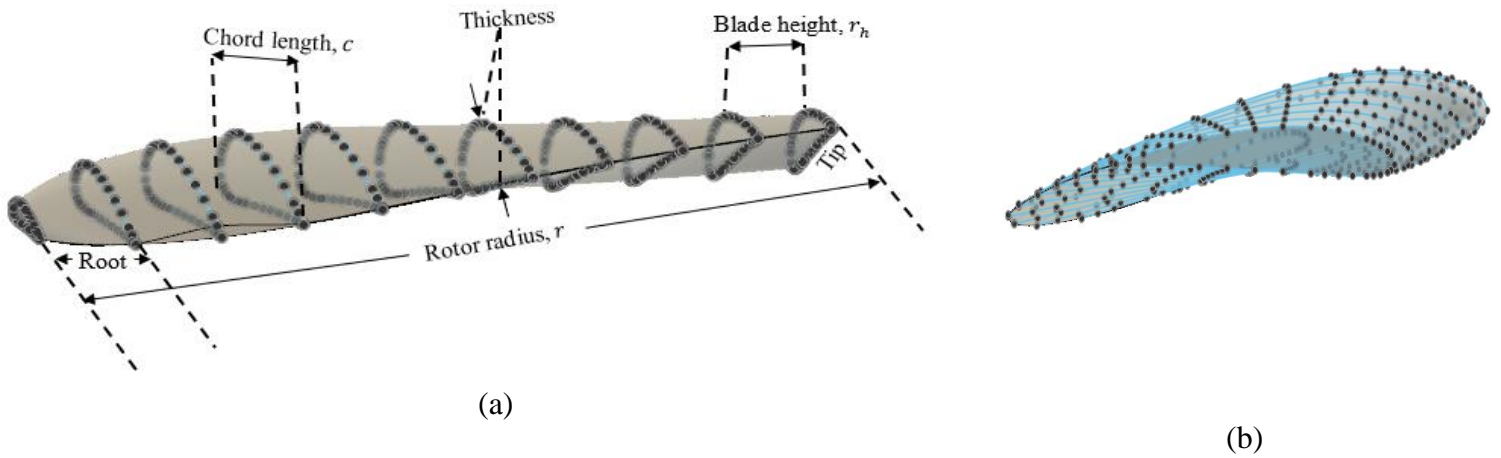


Figure 5.4. Typical blade (a) profile sections (b) twist along the blade span.

Table 5.1. Geometric distribution of the base design blade sections.

r_h/r	c/r	Twist distribution (°)
0.2	0.31	12.0
0.3	0.34	10.5
0.4	0.35	9.0
0.5	0.33	7.5
0.6	0.31	6.0
0.7	0.28	4.5
0.8	0.25	3.0
0.9	0.23	1.5
1.0	0.20	0.0

5.1.1.2 Duct Design

The duct shape used in the present experimental study is duct Type C shown in Fig. 3.6 and was fabricated in-house from PLA (Polylactic Acid) filaments using a 3D printer. It was geometrically scaled to the diameter, D_t of $0.09m$ and a duct-rotor gap of $0.01m$ resulting in $R/r = 1.42$. Figure 5.5 illustrates the duct design shape and scaled geometry of the experimental duct Type C. The radius of the duct section with the inlet arc-flap is $0.0545m$ and the radius of the duct section with rotor installation is $0.05m$. The maximum outer radius of the duct section at the diverging zone is $0.06395m$. The shape of the support structure facing the incoming flow was designed with an elliptical shape to reduce the impact on the flow field by minimizing the

crossflow dimension. The duct supporting pile has a diameter of 0.02m and a length of 0.05m with a base length of 0.05m and a thickness of 0.01m.

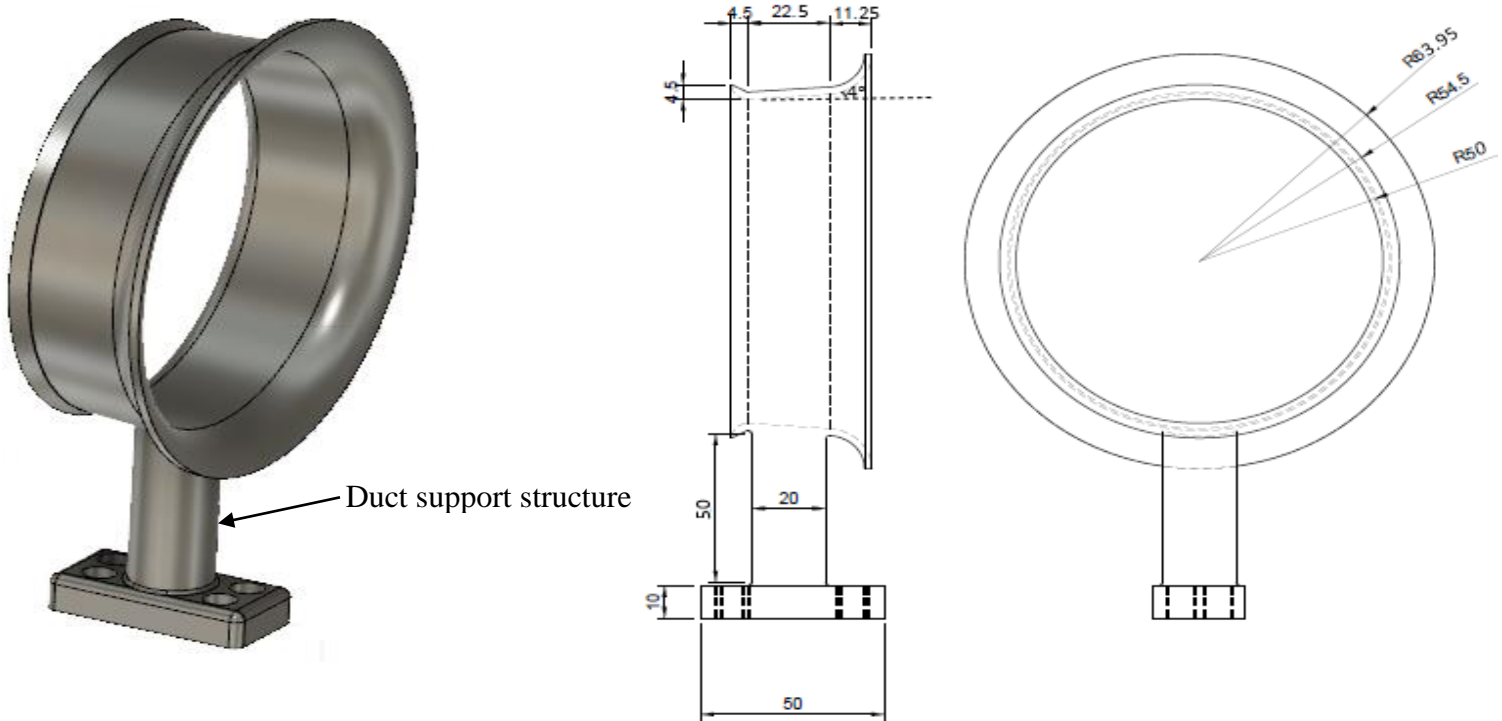
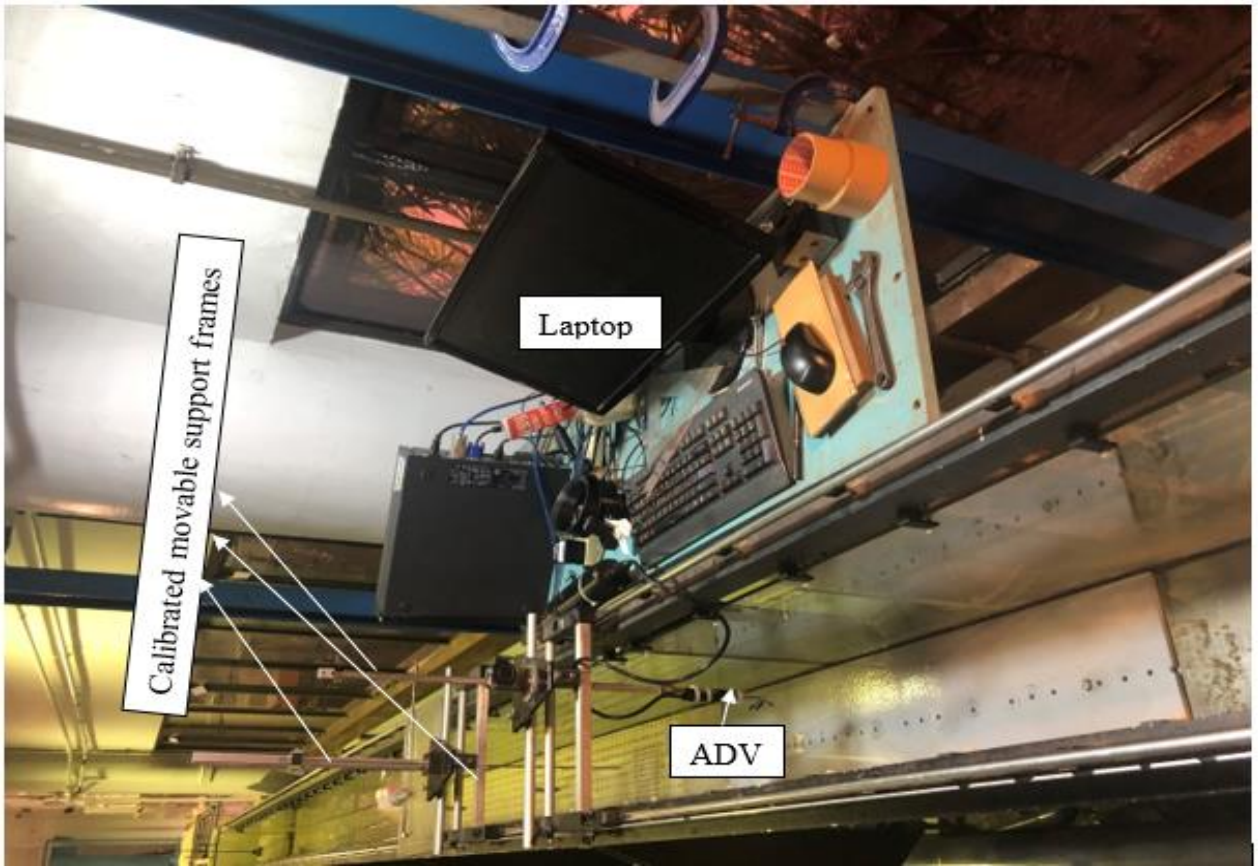


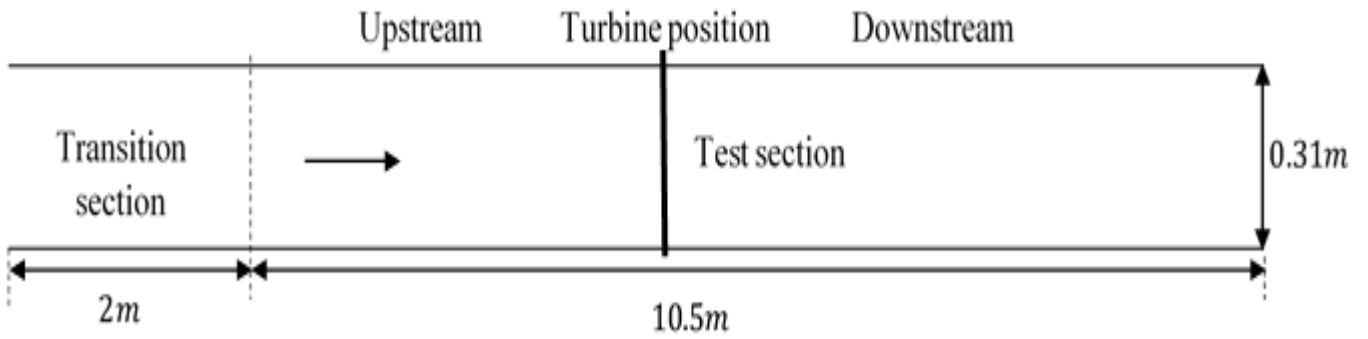
Figure 5.5. The sketch of duct design (measurement is shown in *m m*).

5.1.2 Test Facility

The experiments were conducted in the open-channel recirculating water flume housed in the Hydraulic Laboratory, Department of Civil and Environmental Engineering, The Hong Kong Polytechnic University, SAR, China (Fig. 5.6). The open channel is 0.31m wide, 0.45m deep and 12.5m long. The turbine was installed in the open channel such that the distance between the flume bottom and the hub of rotor was 0.11m. The water depth (d) at the location of the rotor (denoted as OD_t) was maintained at 0.2m throughout the experiments. The diameter-depth ratios were 45% for rotor and 63.95% for duct. To achieve a more steady flow at the flume inlet, a 2m long thin rectangular foam was placed on the water surface to damp the surface water level fluctuations.



(a)



(b)

Figure 5.6. (a) Top view of test section (b) Schematic of the open-channel recirculating water flume and the location of the three blades turbine.

5.1.2.1 Hydrodynamic Performance

As presented in previous chapters, the hydrodynamic performance of the tidal stream turbine is represented in terms of several parameters such as the power coefficient C_p , thrust coefficient C_t , blockage ratio ϵ , tip-speed-ratio (TSR) and solidity σ . The blockage ratio ϵ in the scaled model used in this study is approximately 10% based on rotor area while ϵ is approximately doubled (i.e., 20%) based on the duct area. The TSR ranges from 0 to below 4, as measured in the experiments. However, we note that from Kolekar and Banerjee (2015), the turbine performance is independent of blockage ratio below 10% and at lower TSR (< 4), while it is significantly enhanced for blockage ratio greater than 10% and TSR greater than 4.0. In the present study, blockage corrections were not implemented as the blockage ratio is 10% if the rotor area is used as a reference, and there is insufficient information for the values of thrust. Instead of using blockage correction, the comparative results are also presented against the maximum power coefficient for each data set. The blockage correction is more precise and widely used for a system with a blockage ratio greater than 10%. The equation of blockage corrections for non-dimensional coefficients are presented in Bahaj et al. (2007a).

A Prony brake was used to measure turbine performance, i.e., the power coefficient C_p . The mechanism of working of the rope brake dynamometer is shown in Fig. 5.7a and has been used for the present purpose with good results (Meher-Homji, 2000; Senior et al., 2008). Baron Riche de Prony first proposed his dynamometer in a memoir published in 1822. The rope Prony brake measures power developed by an engine by the method of absorption (friction). As illustrated in Fig.5.7a &b, the rope brake dynamometer uses a rope (friction belt) wound around the rim (radius, r_d) of the pulley rotating at a frequency f_q , a weight m_w is attached to one end of the rope and a spring balance (counterweight), m_s at its other end. The output power, P is then calculated by applying the principle of torque produced by engine equal to frictional torque caused by the rope as

$$P = (m_w - m_s)gr_d\Omega \quad (5.1)$$

where Ω ($= 2\pi f_q$) is the rotor angular velocity and g is the acceleration due to gravity ($= 9.81m/s^2$). The rotor angular velocity, Ω was measured by a digital laser tachometer (Fig. 5.7c)

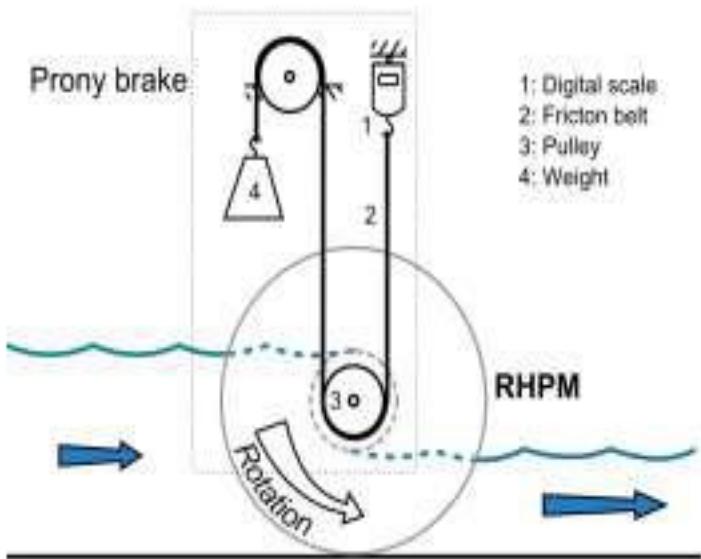
with an accuracy of $\pm(0.05\% + 1 \text{ digit})$ focused on a reflective surface wound around the shaft of the turbine. The TSR is then calculated as the ratio of the rotor tip velocity to the inflow velocity

$$TSR = \frac{\Omega r}{u_0} \quad (5.2)$$

Another characteristic of a turbine is its solidity, σ . Solidity is a coefficient that reflects the turbine efficiency and is expressed as the ratio of the total blade area to the area swept by the turbine.

$$\sigma = \frac{nc}{\pi r} \quad (5.3)$$

where n is the number of blades. It has been shown that increasing the number of blades on the rotor of a wind turbine increases its performance albeit with diminishing returns i.e., impact on aerodynamic efficiency and impulsive noise (Tangler, 2000; Wenehenubun et al., 2015). Also, an increase in the number of blades reduces the operational range and the optimum tip speed ratio. Duquette et al. (2003) investigated the solidity and blade number effect on the performance of horizontal-axis wind turbines and showed that increasing the number of blades at a constant solidity resulted in a reduction in aerodynamic efficiency and power, contrary to the flat plate experimental results and the numerical predictions (Duquette & Visser, 2003).



(a)



(b)



(c)

Figure 5.7. (a) Schematic of Prony brake (Senior et al., 2008) (b) top view of Prony brake system (c) digital laser tachometer.

Thus, a higher solidity would result in lower TSR which would lower cut-in speeds, reduce structural requirements, blade erosion, noise levels and a possible increase in energy extracted. These are some of the reasons why the majority of horizontal axis wind turbines are three (3)-bladed. However, the drawbacks on the weight, cost and turbine efficiency must be considered for the entire turbine design. In the present study, σ is 0.09, where c has been considered in the calculation at 75% of the blade length. This is typical for practical micro (< 100KW) wind turbines with three-bladed rotors that reflect the design philosophy of large utility-scale machines (Duquette et al., 2003).

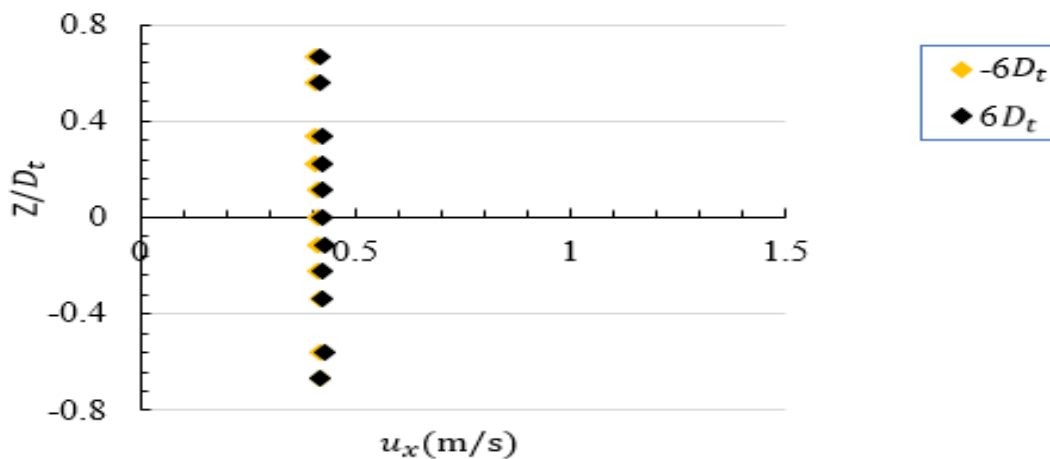
5.1.2.2 Flow Velocity Measurement

Side-looking Acoustic Doppler Velocimeter (ADV, Nortek As, Rud, Norway), a Vectrino Profiler, was used to measure the time-varying flow fields to obtain the centreline (longitudinal), crossflow (lateral) and vertical flow profiles and calculate mean velocity and turbulence intensity. The ADV uses the Doppler effect to measure current velocity by transmitting short pairs of sound pulses, listening to their echoes and measure the change in pitch or frequency of the returned sound. Unlike standard Doppler profilers and current meters, the Nortek Vectrino Profiler is a bistatic sonar i.e., it separately transmits sound through the central beam and receives via the four passive receivers at an angle of 30° towards the transceiver. A

comprehensive description of the probe is presented in Craig et al. (2011) and Thomas et al. (2017). The ADV then calculates the time-varying velocity of the water in the x, y, and z directions in the Vectrino software over a sampling rate of 100 Hz recording 8000 discrete values of velocity. Throughout the measurements, the majority of the samples had a signal to noise ratio (SNR) and correlation coefficient (COR) above 21 and 90 respectively. The total flow velocity (time-varying) is given just as in Eq. (3.34a) with the time-averaged velocity, $\bar{u}_t = \frac{1}{N} \sum_{i=1}^N u_i$ and N is the number of velocity samples (= 8000). The dimensionless longitudinal turbulence intensity I_x is then defined as

$$I_x = \frac{\sqrt{\frac{1}{N} \sum_{i=1}^N (u_i - \bar{u}_t)^2}}{u_0} \times 100\% \quad (5.4)$$

Measurements of vertical profiles of undisturbed flow were taken at $-6D_t$ and $6D_t$ downstream of the test section to ascertain the ambient current and turbulence conditions before conducting the experiments. The vertical profiles of the time-averaged velocities at the two cross-sections were very similar as depicted in Fig.5.8a. The longitudinal current velocities across the vertical direction, Z ($-0.7D_t$ to $0.7D_t$) gradually decreased from 0.43m/s below the hub height to about 0.41m/s near the water surface while in the hub region, the mean longitudinal velocity was approximately 0.42m/s . The longitudinal turbulence intensity, I_x distribution along the vertical direction is displayed in Figure 5.8b.



(a)

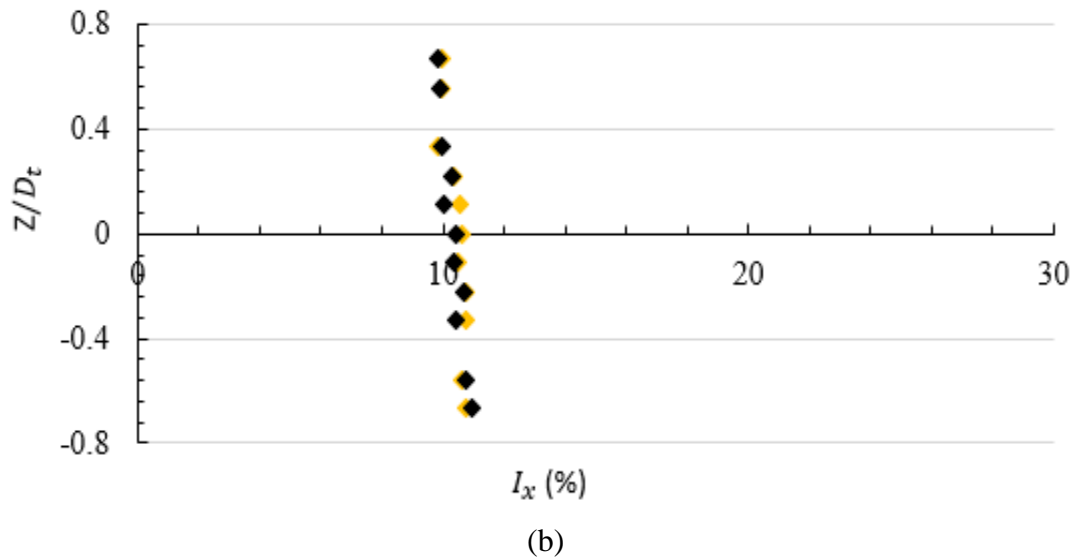


Figure 5.8. Undisturbed flow profiles (a) Vertical Current (b) longitudinal turbulence intensity.

The turbulence intensity at the two cross-sections mainly varied approximately by 1% with slightly stronger turbulence found close to the channel bed of about 11% and decreased to about 10% near the water surface. For calculating dimensionless flow and longitudinal turbulence intensities throughout the experiments, a mean longitudinal inflow velocity, u_0 of 0.42m/s was adopted. The transverse components of mean flow velocity (u_y and u_z) in these regions are less than $0.05u_0$, though not presented, and are not expected to influence rotor loading or wake recovery.

5.1.2.3 Limitations of Scaled Model Testing and Measurement Uncertainty

For physical modelling, a common difficulty is that the geometrical size of turbines that can be tested is often limited due to the size of test facilities available. As one might expect, full-scale Reynolds numbers for a tidal channel are high, in the order of 10^7 , and therefore fully turbulent. In order to extrapolate scaled model data to a full-scale prototype, it is expected that the model and prototype must obey the same physical laws and that relevant dimensionless numbers are the same either by kinematic or dynamic means (Kofoed et al., 2010). In tidal turbines, Reynolds number scaling is the most relevant as it considers fully submerged devices but is almost

impracticable to achieve for micro-scale models under laboratory conditions. Thus, when Reynolds number similitude is not possible, common industrial practice is to use the Froude number (F_r) scaling or kinematic relations (Kofoed et al., 2010; Meyers and Bahaj, 2010). Although, linear scaling between the Froude number and Reynolds number cannot be achieved when the model/prototype ratio becomes too small. However, researchers have tolerated the discrepancy between model and prototype Reynolds numbers for the scaling of hydraulic channels by setting the conditions that Froude scaling is maintained. The Froude number, F_r is expressed as the ratio of the inertial to gravitational forces acting on the flow (Eq. 3.50). In most natural and practical open channel flow conditions, the tidal flows relevant for energy extraction are generally subcritical with F_r around 0.2. In the present study, F_r is less than 0.3. The transition to turbulent flow occurs at Reynolds numbers of approximately 2×10^3 (Myers & Bahaj, 2012). The value of Reynolds number of incoming flows in the flume was $Re(= du_0/\nu) = 8.2 \times 10^4$. Generally, it is acceptable to assume that in an open channel flow the Reynolds numbers lie within the same turbulent classification (just as in the case presented in this study). Also, the Reynolds number in the present study exceeded 4.8×10^4 , the threshold of Reynolds independence for mean flow statistics (mean velocity, turbulence intensity, kinematic shear stress and velocity skewness) as determined by Chamorro et al. (2012). Other previous research suggested that testing of diffuser flows wherein the inlet Reynolds number is above 7.5×10^4 , the pressure recovery, diffuser effectiveness and flow regime are independent of diffuser Reynolds effects for incompressible flow (Cockrell & Markland, 1963; McDonald & Fox, 1966). Though the present model size is necessitated by the limitation of the flume dimensions and more so, we did not intend to replicate any existing marine device but rather to present a good case study on performance characteristics and wake interactions for duct devices in isolation and within an array. The present 1:200th scaled flanged duct tidal stream model set-up, however, represents a turbine of diameter 20m in a water depth of 44.4m.

Another limitation in the present study is that the thrust on the turbine was not measured but a uniform flow rate of $90m^3/hr$ was maintained throughout the experiment resulting in approximately within the value of the adopted mean longitudinal inflow velocity, u_0 (based on the cross-section of the test channel at the position of the turbine). Meyers and Bahaj (2010) pointed out that the thrust coefficient of the rotor disk only has an obvious influence on the velocity deficit of near wake but less influence on the far wake. Park et al. (2007) showed that

the power coefficient of a wind turbine is very sensitive to change in model scale, but the thrust coefficient is independent of the scale effects. Therefore, the differences in scales of model and full-scale prototypes may result in dissimilitude between the flow regimes and thus, the performance of the turbines at model-scale may slightly deteriorate. Micro-scaled tidal turbines nevertheless have an important role to play with exciting prospects in meeting our daily thirst for clean energy and will contribute to meeting the target of a net-zero greenhouse gas emissions economy by 2050.

In terms of ebb and flood tides, tidal current flows are nearly bidirectional. Therefore, a horizontal axial tidal turbine with unidirectional hydrofoils must be able to redirect its face to the current directions in order to achieve maximum current energy harvesting. There are different approaches to accomplish turbine alignment with the changing direction of the tides: yaw mechanism, blade pitch angle adjusting mechanism and a turbine with a bidirectional rotor (Liu et al., 2014; Nedyalkov & Wosnik, 2014; Frost et al., 2015; Guo et al., 2020). However, due to the severe maritime environment and the high cost of installation and maintenance, the first two techniques are not cost-effective in marine applications. The latter approach (i.e., the use of a bidirectional rotor) achieves about the same energy extraction capacity capability in either tidal current direction (Liu et al., 2014; Guo et al., 2020). Therefore, in the experiments, we considered the turbine to be a bidirectional rotor installed to a monopile and housed in a flanged duct. The performance of the devices is solely evaluated based on the performance of the rotor. For the reversed flows, the duct is rotated to study its performance under bidirectional flows. However, it is envisaged that the phase of the flood and the ebb-tidal cycles will vary greatly in real-world applications for bi-direction tidal flows and the whole device system must rotate when tidal flow turns over. As a result, it can be said that the present experimental set-up is an idealized case to some extent i.e., a monopile and a duct are coupled to the rotor, and the tidal cycles' phase is assumed to be the same size and in opposite direction relative to the turbine. Hence, a better design should be adopted in field applications, such as the industrial applications shown in Fig. 2.2 (Rotech Tidal Turbine), Fig. 2.3 (Solon Tidal Turbine) and/or Fig. 2.6 (HydroHelix Tidal Turbine) and a bidirectional rotor will be used such that its performance is independent of the flow direction.

To further facilitate the possible use of experimentally determined data for commercial purposes, the uncertainty associated with such data are strongly recommended to be evaluated as it directly

reflects the economic feasibility of wind turbine plants (Frandsen et al., 1990). Thus, uncertainty affecting measurements are estimated by applying the law of propagation of uncertainty to quantities of interest (λ and C_p) with the assumption that the uncertainty sources are independent (Frandsen et al., 1990; Taylor & Kuyatt, 1994; Kofoed et al., 2010; Coleman & Steele, 2018). That is

$$U = U(q_1, q_2, \dots, q_i) \quad (5.5)$$

$$(\delta U)^2 = \left(\frac{\partial U}{\partial q_1} \delta q_1\right)^2 + \left(\frac{\partial U}{\partial q_2} \delta q_2\right)^2 + \dots + \left(\frac{\partial U}{\partial q_i} \delta q_i\right)^2 \quad (5.6)$$

where δ is the uncertainty in each parameter, U is the quantity of interest, and q_i are the measured variables. Since the different measurand errors provide different sensitivities, a combination of all would be useful in providing a more realistic uncertainty measure. Practically, significant uncertainties may be attached to power curve measurement, so applying propagation of uncertainty Eq. (5.6) in Eqs. (5.2) and combined (3.11) & (5.1), we have for the combined standard uncertainty of the calculated parameters of interest

$$TSR = TSR(\Omega, r, u_0) \quad (5.7a)$$

$$(\delta TSR)^2 = \left(\frac{\partial TSR}{\partial \Omega} \delta \Omega\right)^2 + \left(\frac{\partial TSR}{\partial r} \delta r\right)^2 + \left(\frac{\partial TSR}{\partial u_0} \delta u_0\right)^2$$

$$(\delta TSR)^2 = \left(\frac{r}{u_0} \delta \Omega\right)^2 + \left(\frac{\Omega}{u_0} \delta r\right)^2 + \left(-\frac{\Omega r}{u_0^2} \delta u_0\right)^2 \quad (5.7b)$$

$$\Rightarrow \text{the relative uncertainty in } TSR, \delta TSR_r = \frac{\delta TSR}{TSR} = \sqrt{\left(\frac{\delta \Omega}{\Omega_{mean}}\right)^2 + \left(\frac{\delta r}{r}\right)^2 + \left(\frac{\delta u_0}{u_0}\right)^2} \quad (5.7c)$$

and

$$C_p = C_p(m_w, m_s, g, \Omega, r_d, \rho, A, u_0) \quad (5.8a)$$

$$(\delta C_p)^2 = \left(\frac{\partial C_p}{\partial m_w} \delta m_w\right)^2 + \left(\frac{\partial C_p}{\partial m_s} \delta m_s\right)^2 + \left(\frac{\partial C_p}{\partial \Omega} \delta \Omega\right)^2 + \left(\frac{\partial C_p}{\partial r_d} \delta r_d\right)^2 + \left(\frac{\partial C_p}{\partial \rho} \delta \rho\right)^2 + \left(\frac{\partial C_p}{\partial A} \delta A\right)^2 + \left(\frac{\partial C_p}{\partial u_0} \delta u_0\right)^2$$

$$(\delta C_p)^2 = \left(\frac{gr_d\Omega}{0.5\rho Au_0^3} \delta m_w\right)^2 + \left(-\frac{gr_d\Omega}{0.5\rho Au_0^3} \delta m_s\right)^2 + \left(\frac{(m_w-m_s)gr_d}{0.5\rho Au_0^3} \delta \Omega\right)^2 + \left(\frac{(m_w-m_s)g\Omega}{0.5\rho Au_0^3} \delta r_d\right)^2 + \left(-\frac{(m_w-m_s)gr_d\Omega}{0.5\rho^2 Au_0^3} \delta \rho\right)^2 + \left(-\frac{(m_w-m_s)gr_d\Omega}{0.5\rho A^2 u_0^3} \delta A\right)^2 + \left(-3\frac{(m_w-m_s)gr_d\Omega}{0.5\rho Au_0^4} \delta u_0\right)^2 \quad (5.8b)$$

\Rightarrow the relative uncertainty in C_p ,

$$\delta C_{p_r} = \frac{\delta C_p}{C_p} = \sqrt{\left(-\frac{\delta m_s}{(m_w-m_s)_{mean}}\right)^2 + \left(\frac{\delta \Omega}{\Omega_{mean}}\right)^2 + \left(\frac{\delta r_d}{r_d}\right)^2 + \left(-\frac{\delta \rho}{\rho}\right)^2 + \left(-\frac{\delta A}{A}\right)^2 + \left(-3\frac{\delta u_0}{u_0}\right)^2}$$

(5.8c)

The standard uncertainty values for velocity (δu_0), density ($\delta \rho$), angular velocity ($\delta \Omega$), rotor radius (δr), rim radius (δr_d), and counterweight (δm_s) are equal to 0.01 (m/s), 0.04464 (kg/m^3), 0.0005 (rad/s), 0.0001(m), 0.0001(m), 0.000001(kg) respectively. $\frac{\delta A}{A} = 2 \frac{\delta r}{r}$ while the attached weight (δm_w) is neglected as it is a predetermined mass slot. The values with the subscript ‘mean’ are the average value of each measurement. Thus, the resulting relative uncertainties (Eqs. 5.7c & 5.8c) in δTSR_r and δC_{p_r} are 2.4% and 8.4% respectively.

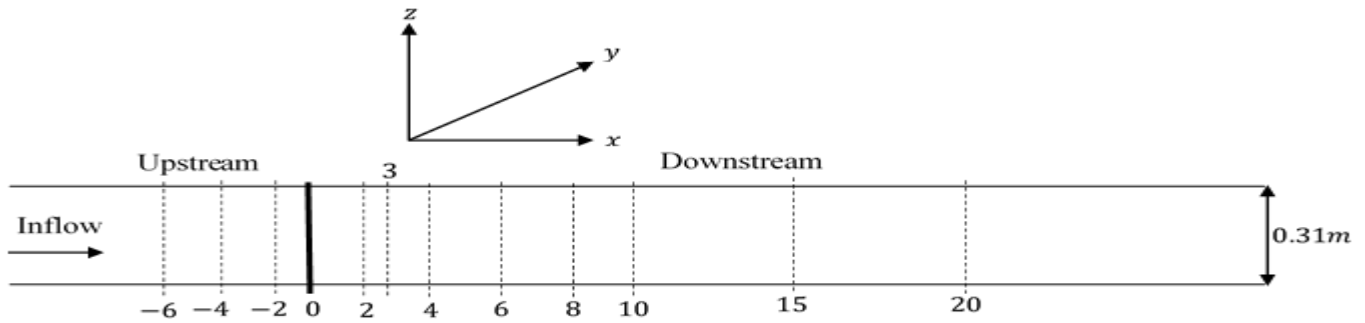
5.1.3 Turbine Layout Configurations

The layouts of the arrangement of model turbines in the experiments are presented in the following sections. Locations of wake measurements are represented in terms of the distance in meters divided by the turbine diameter with reference to the rotor center of the upstream turbine. The origin of each experiment study is positioned at $0D_t$, the middle of the channel with 6.25m downstream away from the inlet and wake measurement extents are reported up to $20D_t$ and $30D_t$ downstream for the single turbine case and two-inline turbines case respectively.

5.1.3.1 Single Row of Turbines

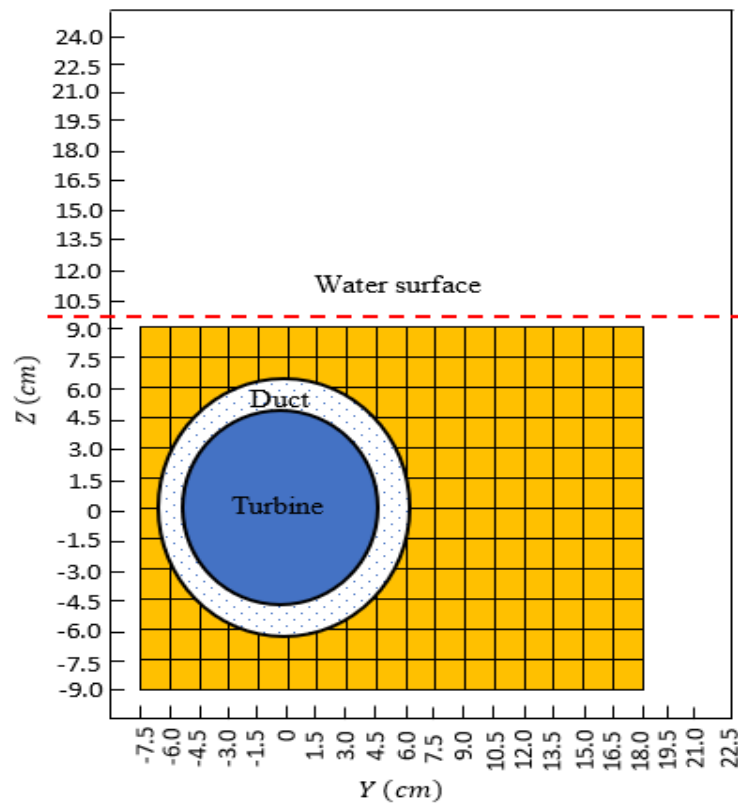
In the single row of turbines arrangement, the lateral separation of adjacent turbines is determined by the channel width which is 0.31m. Only one turbine is required, and it is installed in the middle of the channel. For wake measurements and characterisation of the local flow, the origin of the coordinate system is placed at the position of the rotor, with the in-stream direction denoted by x, the cross-stream direction as y and the vertical position by z. The ADV was mounted by a clamping system fixed on a carrying platform that was freely moved along the flow direction. The ADV can be moved along the vertical direction and lateral direction of the channel and was used to measure the time-varying velocities (u_x, u_y, u_z). The three-dimensional mean velocities and the dimensionless longitudinal turbulence intensity were subsequently

calculated. Detailed velocity measurements were carried out at six test cross-sections



downstream to investigate the far wake characteristics. The interval between the cross-sections

(a)



(b)

Figure 5.9. Velocity measurement locations (a) Locations of cross-sections where velocity measurement was made, the numbers on the dash lines denote the distance (D_t) from turbine rotor plane (b) locations of velocity measurement made at all cross-sections except the blade and duct swept area.

was $2D_t$ from distance $4D_t$ to $10D_t$, then changed to $5D_t$ from distance $10D_t$ to $20D_t$. In the vertical direction, velocity samples were collected at thirteen heights, with an average spacing

of $0.01m$. The top layer and the bottom layer of the velocity measurements were both $0.01m$ below the water surface and above the test channel bed. In the lateral direction, velocities were measured over the range Y ($-0.7D_t$ to $1.0D_t$) with a spacing of $0.02m$. The schematic representations of locations of velocity measurement are illustrated in Fig. 5.9. Figure 5.10 depicts turbine set-up in the open-channel recirculating water flume.

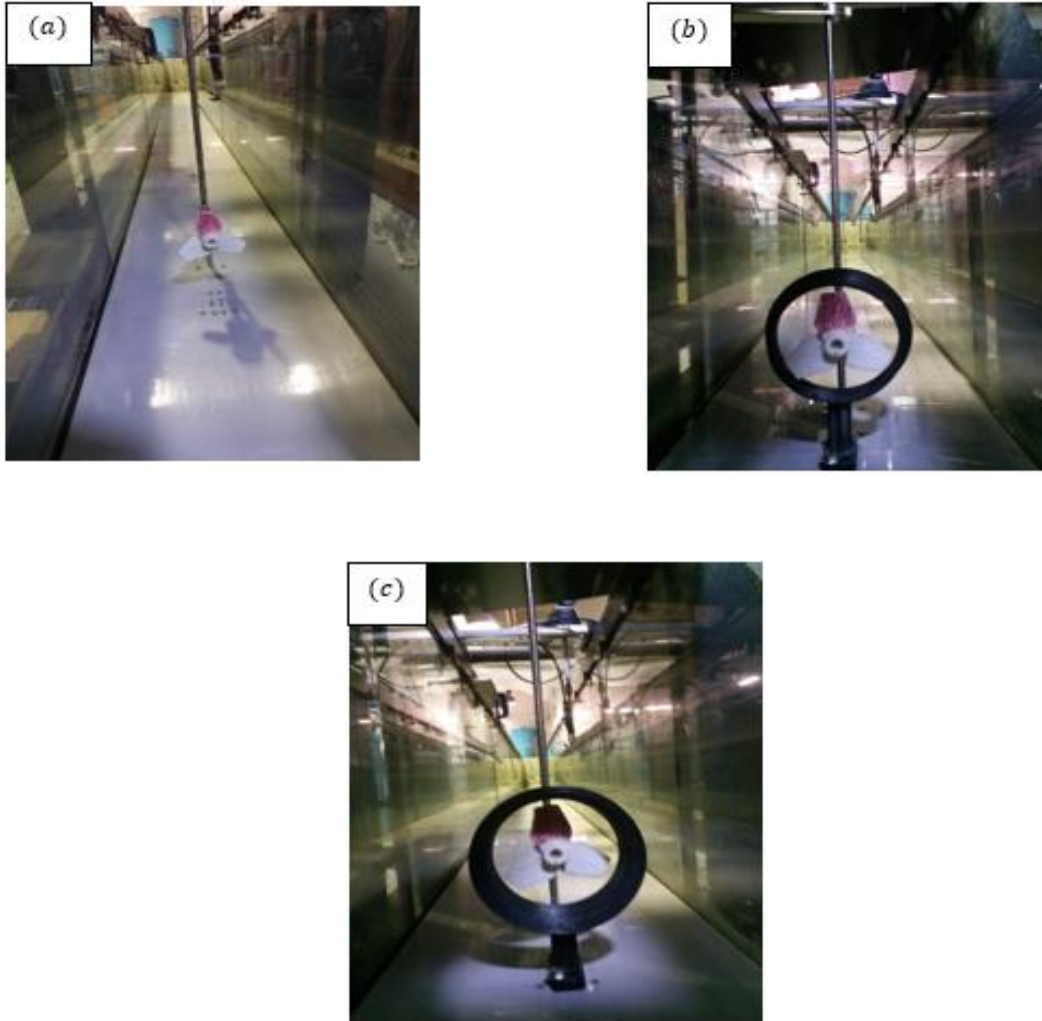
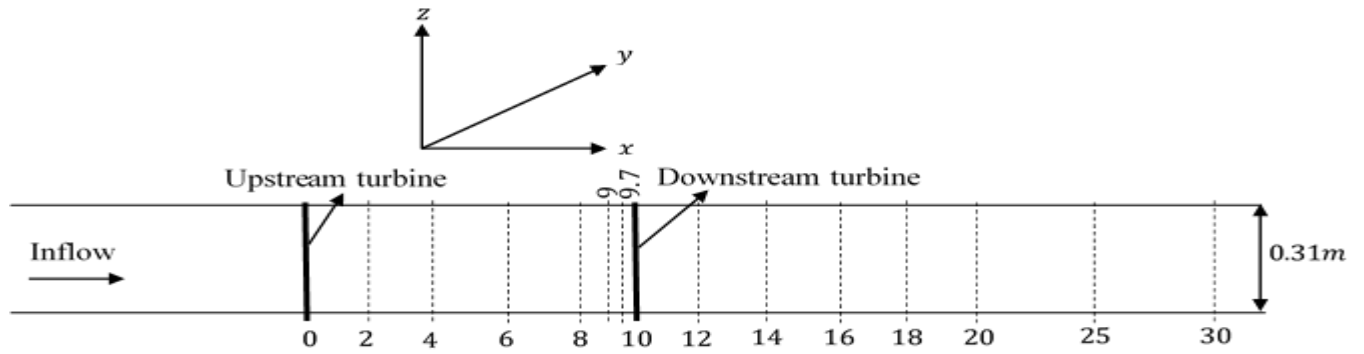


Figure 5.10. Single turbine set-up in the open-channel recirculating water flume (a) bare (b) ducted turbine in forward flow (c) ducted turbine in reversed flow.

5.1.3.2 Two-inline Turbines



(a)

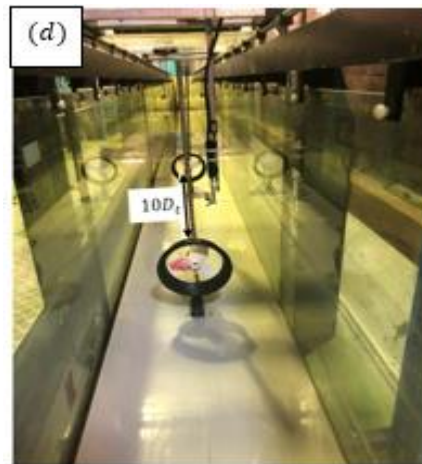
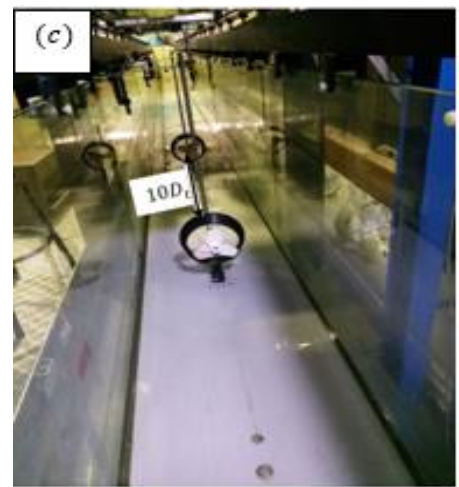
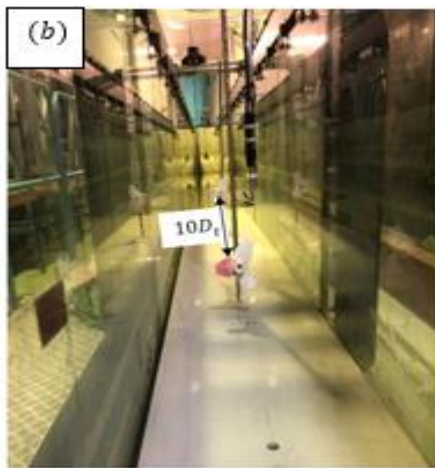


Figure 5.11. Velocity measurement locations (a) Locations of cross-sections where velocity measurement was made for two inline turbine arrays, the numbers on the dash lines denote the distance (D_t) from the turbine rotor plane. Axially aligned turbine set-up in the test section (b) bare (c) ducted turbines in forward flow (d) ducted turbines in reverse flow.

To make tidal streams commercially viable multiple tidal stream turbines are likely to be placed in farms or arrays (Funke et al., 2016). Adcock and Draper (2014) showed that there is a significant interaction between multiple turbines deployed in a given region. In this section, a multiple-row array configuration is developed to further investigate the wake structure of a turbine in an array. An in-line arrangement is applied to the multiple-row array and the corresponding schematic of turbine spacing is shown in Fig. 5.11. For simplification, only two turbines were deployed with a separation distance of $10D_t$ throughout the experimental measurements. Similar to measurements for the case of single row turbine, detailed velocity measurements were carried out at five test cross-sections upstream of the downstream turbine and at seven test cross-sections downstream of the downstream turbine as illustrated in Fig. 5.10a to investigate the far wake characteristics for each turbine system.

5.2 Chapter Summary

The chapter introduced the design of model turbines and the set-up of experiments. We noted that studies in controlled environments will provide insights on the performance objectives of developed converter designs and wake characterisation arising from different array layout configurations and allow for a large unexplored parameter space to be investigated. Thus, a comprehensive 1:200th scaled tidal stream model experiment was conducted in an open channel housed in the Hydraulic Laboratory, Department of Civil and Environmental Engineering, The Hong Kong Polytechnic University, SAR, China. The experimental setup in the present study represents a turbine of diameter 20 m in a water depth of 44.4 m. The working test section is 0.31m wide, 0.45m deep and 12.5m long and the value of the Reynolds number of incoming flows in the open channel was $Re = 8.2 \times 10^4$ indicating that the experimental conditions in the open channel are within the turbulent region. The experiment is to examine in detail the interaction effects between flanged ducted and non-ducted marine current turbines in terms of performances and wake characterisation. Wake mapping was represented in terms of longitudinal (centerline), lateral (crossflow), and vertical profiles of velocity ratios and turbulence intensity.

The blade design chosen for this study is based on the NACA 4412 airfoil. Three blades were used and were located 120° apart. The airfoil was constructed in-house and produced via a 3D

printer, then rubbed with sandpaper to ensure smoothness and a more homogeneous distribution of surface roughness. It was geometrically scaled to the diameter, D_t of $0.09m$ and the key design parameters that defined the three-bladed rotor are blade height r_h , rotor radius r and twist angle distribution. The duct shape used is the duct Type C whose performance was first numerically investigated using the actuator disk method. The duct was geometrically scaled to the diameter, D_t of $0.09m$ with a duct-rotor gap of $0.01m$ resulting in $R/r = 1.42$. The duct inlet and maximum outer radii are $0.0545m$ and $0.06395m$ respectively. The duct is mounted on an elliptical-shaped supporting pile of length $0.05m$ and a base length of $0.05m$. The distance between the flume bottom and the hub of rotor is $0.11m$ and water depth (d) at rotor location ($0D_t$) was maintained at $0.2m$ throughout the experiments. Before doing experiments on turbines, measurements of undisturbed flow were conducted using the ADV at $-6D_t$ and $6D_t$ downstream of the test section to ascertain the ambient current and turbulence conditions. The longitudinal turbulence was found to vary from about 11% close to the channel bed to about 10% near the water surface for all systems while current velocities gradually decreased from $0.43m/s$ below the hub height to $0.41m/s$ near the water surface. Throughout the control experiment, a mean longitudinal inflow velocity, u_0 of $0.42m/s$ was adopted for calculating dimensionless flow and longitudinal turbulence intensities.

For the measurement of turbine performances, the principle of Prony brake was adopted which measures power developed by an engine by the method of absorption (friction). The Prony brake has shown good results in previous works specifically for this purpose. Locations of wake measurements were represented in terms of the distance in meters divided by the turbine diameter with reference to the rotor center of the upstream turbine. For a single-row turbine, detailed velocity measurements were carried out at six test cross-sections downstream at an interval of $2D_t$ from distance $4D_t$ to $10D_t$, then changed to $5D_t$ from distance $10D_t$ to $20D_t$. Then in the vertical direction, velocity samples were collected at thirteen heights, with an average spacing of $0.01m$. The top layer and the bottom layer of the velocity measurements were both $0.01m$ below the water surface and above the test channel bed. In the lateral direction, velocities were measured over the range y ($-0.7D_t$ to $1.0D_t$) with a spacing of $0.02m$. Similarly, for the configuration of the two-inline turbine, detailed velocity measurements were carried out at five test cross-sections upstream of the downstream of the reference turbine and seven test cross-sections downstream of the second turbine.

CHAPTER SIX

Experimental Results and Discussion

With the proposed optimum duct design from CFD solutions, a comprehensive scaled physical experiment was then conducted in an open-channel recirculating water tunnel to further assess the influence of the interaction effects between turbines of the same kind. The cases of bare turbine and ducted turbines were investigated to quantify the power performances and wake characteristics. The experiments included flow through isolated turbines and flow through two axially aligned turbines. The key findings were analyzed and presented in the following sections.

6.1 Experimental Analyses

From the preliminary extensive CFD simulation results analyzed and discussed in the preceding sections, the best performing duct type was identified as duct Type C. This was attributed to the incorporation of an inlet-arc flap and a curved flange and a consequence of an inherent simultaneous action leading to a significant increase in flow swallowing and transmission capability of the duct entailing a larger low-pressure zone. Hence, significantly improved peak power coefficient, although at the loading condition with the thrust coefficient significantly smaller than that of a bare turbine. The physical experiment geometrically scaled to the diameter, D_t of $0.09m$ was then conducted in an open-channel recirculating water tunnel using duct Type C and a three-bladed turbine based on the NACA4412 airfoil located 120° apart. The turbine was positioned at $0D_t$ mark in the tunnel and with an inflow velocity, $u_0 (= 0.42m/s)$. The interaction effects of the duct on the performance and characteristics of wake evolution downstream of a flange ducted tidal stream turbine model was examined. The power performance was determined using the Prony brake while velocity and turbulence measurements were conducted using the side-looking ADV. Locations of velocity measurements were represented in terms of the distance in meters divided by the turbine diameter, D_t with reference to the rotor center of the upstream turbine. Velocity measurement locations were up to $20D_t$ downstream of the cases with an isolated turbine and $30D_t$ for the cases with two axially aligned ducted turbines or bare turbines.

6.2 Performances of Ducted Turbines with Real Rotors

In this section, the power performance of the ducted turbines obtained from the physical experiments was presented and compared to that of the bare turbine. Firstly, the power performance of isolated turbines was analysed in section 6.2.1. Secondly, the power performances of the downstream turbines in the axially aligned arrangement were examined in section 6.2.2. The separation distance between the two axially aligned turbines was $10D_t$.

6.2.1 Performances of Isolated Turbines in Single Row Arrangement

The result for the variation of the power coefficient, C_p (based on the rotor area) with the tip speed ratio, TSR is shown in Fig. 6.1. Notably, the power coefficient - TSR curve is relatively short spanning, with a TSR range of 0.90 - 3.80. This is typical for a tidal stream rotor for which the maximum power is delivered at lower values of TSR ($TSR < 4$), leading to large torque production (Borg et al., 2020). The operating range of the bare turbine is about 9% (freewheeling $TSR = 3.2$) smaller than that of the duct Type C, and about 19% (freewheeling $TSR = 3.5$) smaller than that of duct Type C Reversed (freewheeling $TSR = 3.8$) turbine. Similarly, the operating range of duct Type C is about 9% smaller than that of duct Type C Reversed. The maximum C_p of value about 0.18, 0.22 and 0.25 occurs at TSR equal to 2.1, 2.5 and 2.9 for the bare, duct Type C and duct Type C Reversed respectively. The TSR for optimum operation is increased by 36% for duct Type C Reversed and 19% for duct Type C as compared to that of the bare turbine. The duct Type C Reversed gives the best power performance and the peak C_p value is about 11% higher than that of the duct Type C. In numerical simulations, similar results are obtained although the peak C_p for Type C Reversed is about 4% higher than that of Type C (Fig. 4.9a, b). This enhancement in duct performance can only be a consequence of a strong reduction in inlet loss and unsteady pressure zone at the duct exit, thus inducing more flow into the interior region of the duct. The concentration of flow inside the duct is clearly supported by the higher incoming flow at the duct inlet depicted in Fig. 6.2 for duct Type C with no rotor present. Also, both ducted turbines are better than the bare turbine in terms of power performance. The peak C_p of duct Type C is 25% higher than that of the bare turbine, and the peak C_p of duct Type C Reversed is 36% higher than that of the bare turbine. The power performance of the ducted turbines is similar to that of a 200 kW OpenHydro demonstrator device, i.e., C_p about 0.3 with a

2.5m/s rated flow speed (Polagye et al., 2010). To facilitate the comparison between the experiment and the numerical results, it is noted that TSR and $(1 - a)$ are both related to the freestream velocity and the numerical results (Fig. 4.9) were redrawn in terms of C_p vs $(1 - a)$ for the bare, duct Type C and duct Type C Reversed turbines as illustrated in Fig. 6.3. The curves all clearly follow the same trend as the curves obtained in experiments results but with larger magnitudes.

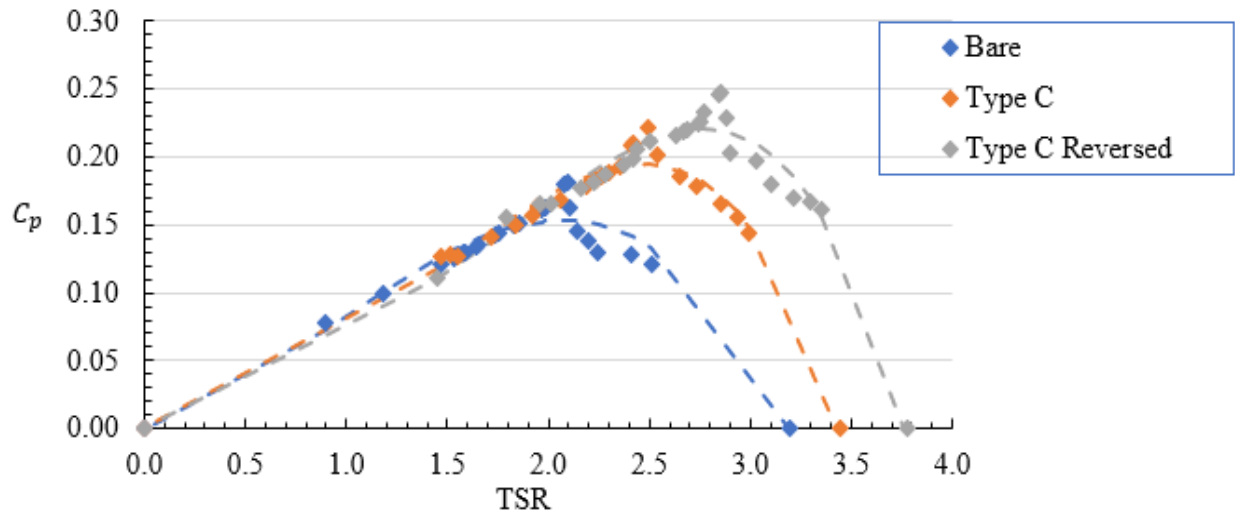


Figure 6.1. Power coefficient vs TSR for single row turbines.

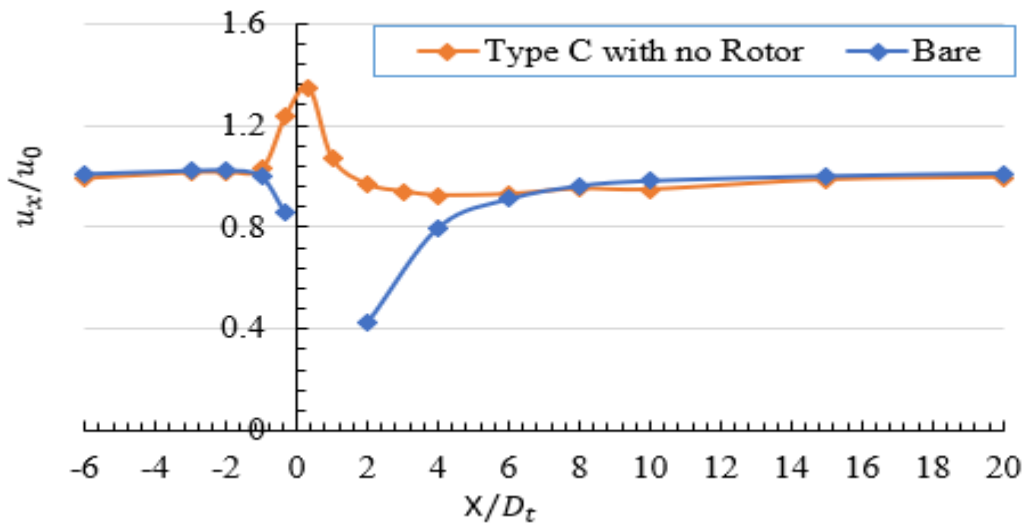


Figure 6.2. Centerline velocity distribution.

For the experimental performance curves, duct Type C reaches freewheeling earlier than duct Type C Reversed, which is different from that shown in the numerical performance curves. The shift in the peak and/or freewheeling positions is likely due to that TSR and $(1 - a)$ do not bear a directly proportional relationship. However, Figure 4.9b (i.e., C_p vs C_t) shows that Type C reaches freewheeling earlier than Type C if C_t is employed instead of $(1 - a)$, which is consistent with the experimental curves (Fig. 6.1). The comparatively substantial difference in the performance levels between the numerical and experimental results may be due to the use of a uniform actuator disk model in the numerical simulation. The actuator disk model tends to over-predict the turbine performance due to the omission of swirl and shedding of coherent vortices from the discrete blade. Another factor that could influence the performance is the sensitivity of the power coefficient to change in model scale (1:200 in the present study) as shown by Park et al. (2007).

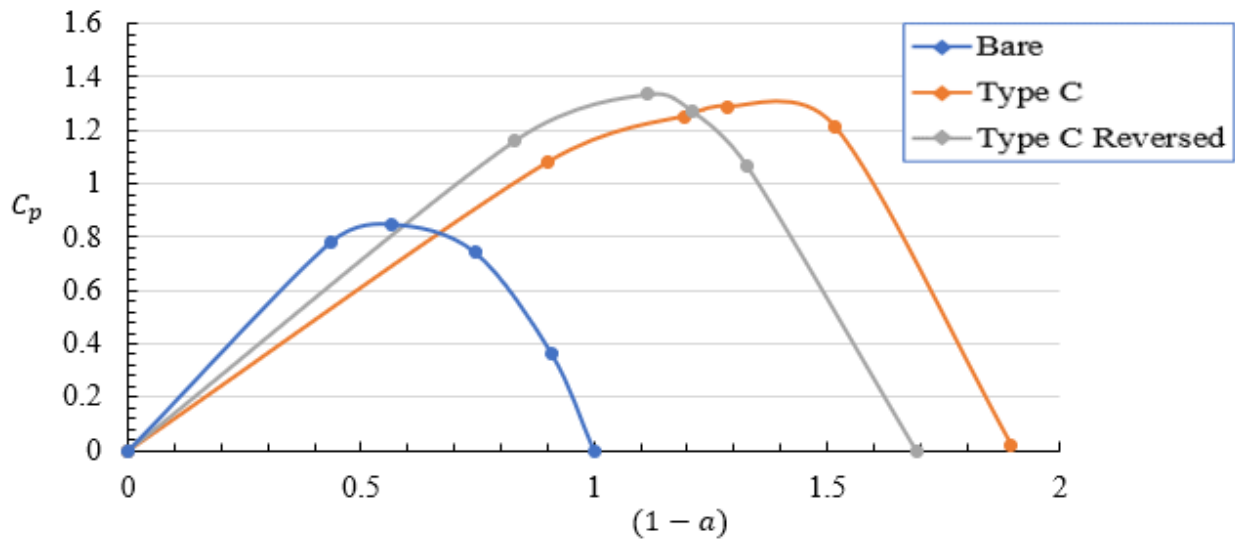


Figure 6.3. CFD Power coefficient vs $(1 - a)$ for single row turbines.

Under laboratory conditions, the Reynolds number attained in the experiments was not sufficiently large and the flows did not reach the fully turbulent conditions for the rotor. This may affect the operational capabilities of the scaled turbines. The extrapolation of the results to the prototype scale thus should be with caution. In the present experimental test setup, one of the limitations is that the loading coefficient on the turbine was not ascertained. Peak C_p occur at

very low rotor loading (thrust) for the ducted turbines (Abe & Ohya, 2004; Belloni, 2013; Fleming & Willden, 2016; Maduka & Li, 2021). Thus, the actual value of the thrust in the present experiment (not measured) may also influence the duct performance. As highlighted in Bahaj et al. (2007a), the proximity of the water surface reduces the pressure difference across the turbine and thus contributed to the reduction in turbine performance. Notwithstanding, the results show that ducted turbines generate higher peak power per rotor unit area than that of the bare turbine.

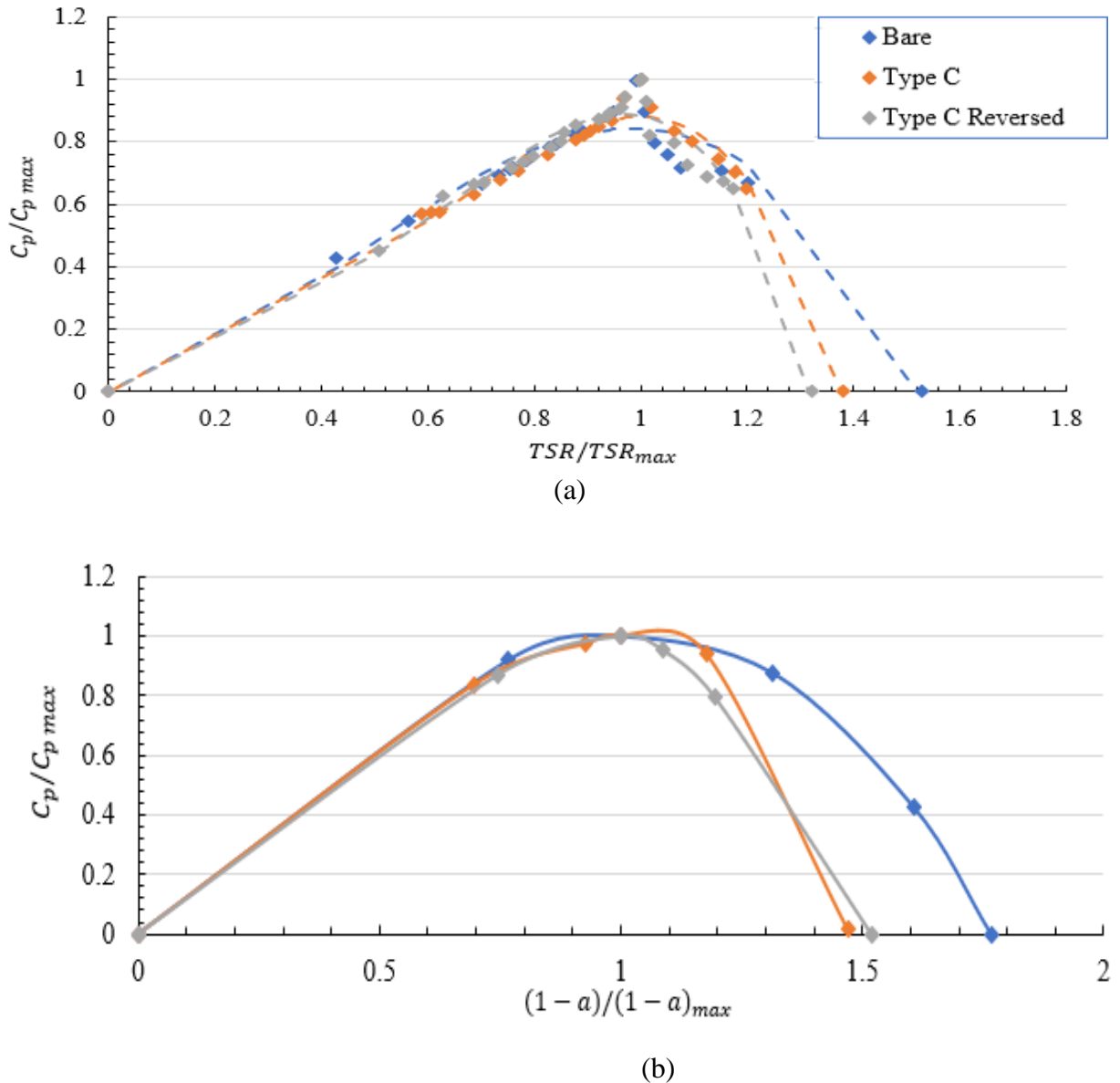
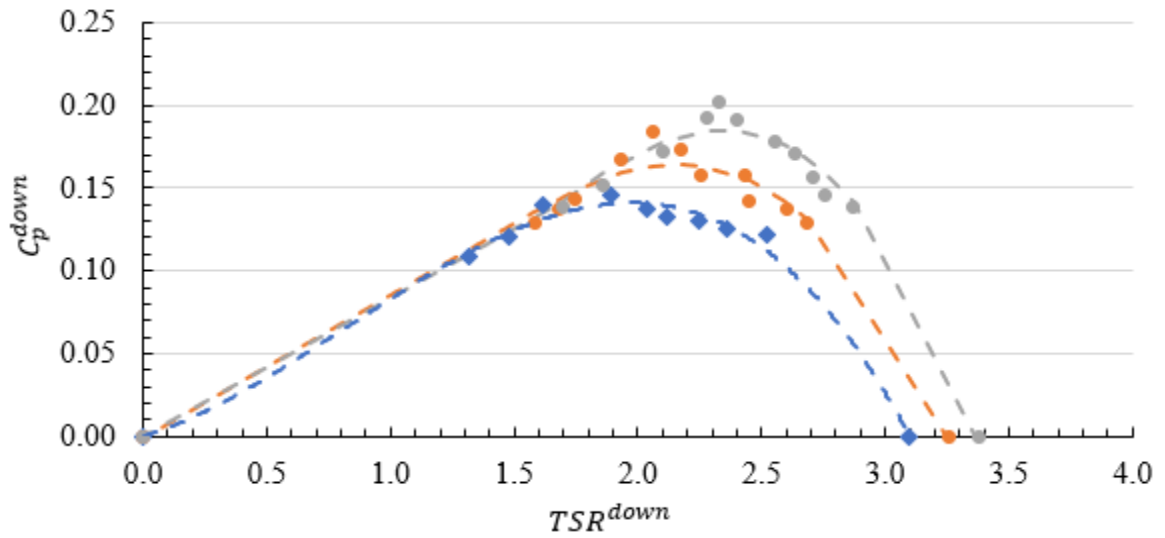


Figure 6.4. Normalized peak power coefficient vs peak TSR & peak $(1-a)$ for single row turbines (a) experiment (b) numerical.

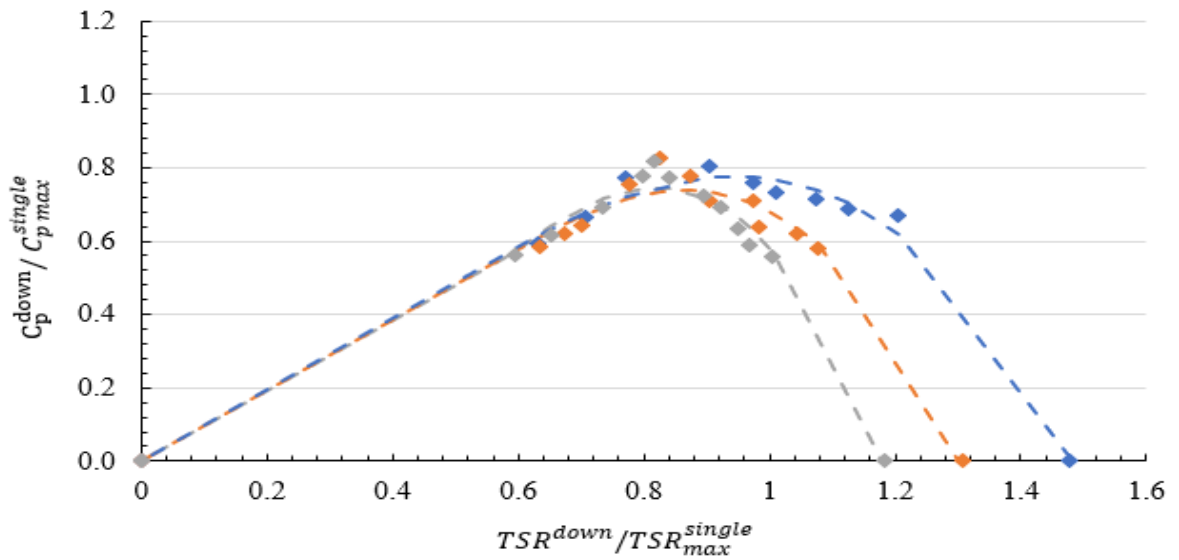
It also suggests an effective way to significantly increase the performance of a turbine of a given rotor size. In general, the data from the physical modelling implies that the results are dependent on turbine flow, device design and operating conditions with a reduction in operating range when working with smaller scales while larger turbine develops higher power performance (Rancourt et al., 2007; Watson et al., 2019). The outcome of experiments also agrees well with Betz's findings in the technical memorandum for medium-speed windmills (Betz, 1928), Mycek et al. (2014), and Yigit (2020) with a peak power coefficient of about 0.3. For further analysis between the experimental and the numerical results, additional figures with quantities normalised in terms of TSR or $(1 - a)$ at the point of the occurrence of maximum C_p are presented in Fig. 6.4. It can be seen that the performance curves for both the experiments and the numerical simulations overlap in the rising regions ($0 < \frac{TSR}{TSR_{max}} < 1$) or ($0 < \frac{1-a}{(1-a)_{max}} < 1$) for all turbines. In the falling regions ($\frac{TSR}{TSR_{max}} > 1$) or ($\frac{1-a}{(1-a)_{max}} > 1$), some differences in the curves occur especially at the freewheeling points.

6.2.2 Performances of Downstream Turbines in Two-axially-aligned Turbine Arrangement

One way to evaluate the interaction effects between two turbines is to examine the performance of the downstream turbine which was installed at a distance of $10D_t$ downstream of the upstream turbine (section 5.1.3.2). The variation of C_p^{down} of the downstream turbine is with the associated TSR^{down} is shown in Fig. 6.5a for different devices. This can show the degree of influence of the operating upstream device. The variation of C_p of an isolated device as a function of the associated TSR is already discussed in section 6.2.1. For a more convenient comparison, Fig. 6.5b depicts the curve of the normalised C_p^{down} ($= C_p^{down} / C_p^{single}$) of the downstream turbine against the associated normalised TSR^{down} ($= TSR^{down} / TSR_{max}^{single}$), where C_p^{single} refers to the C_p_{max} of the corresponding isolated turbine and TSR_{max}^{single} refers to the TSR_{max} of the corresponding isolated turbine. The results (Fig. 6.5a) show that the reduction in the power coefficient is the least for the bare turbine (i.e., 20%), more for duct Type C (i.e., 22%) and the most for the duct Type C Reversed (i.e., 25%).



(a)



(b)

Figure 6.5. (a) downstream turbine $C_p^{\text{down}} - \text{TSR}^{\text{down}}$ curve (b) normalised downstream turbine $C_p^{\text{down}} - \text{TSR}^{\text{down}}$ curve with $C_{p \max}^{\text{single}}$ and $\text{TSR}_{\max}^{\text{single}}$

The curves shown in Fig. 6.5b are similar to the curves in Fig. 6.4a and show that the downstream turbine is adversely affected by the presence of an operating axially aligned upstream turbine, with the reduction in power coefficient of up to 25%. This is due to the wake characteristics of the upstream turbine, which will be discussed in detail in the next section. The wake recovery of duct turbines was found to be relatively poor, with the wake velocity being slightly less than 5% for duct Type C (at I_x of about 14%) and about 7% for duct Type C

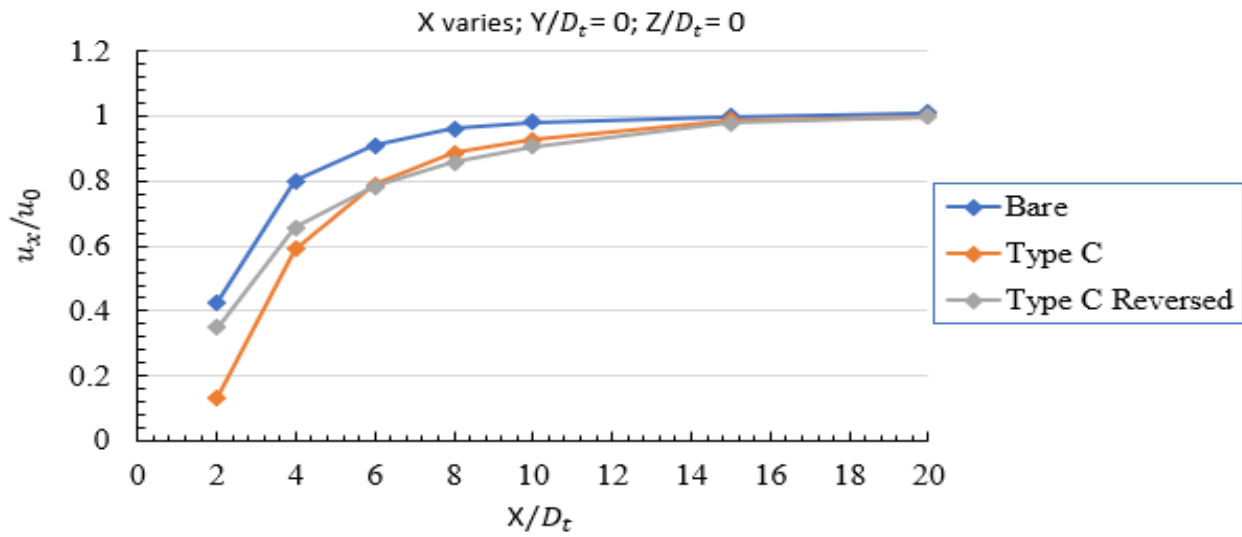
Reversed (at I_x slightly above 14%) to that of the bare turbine (at I_x of about 12%) at 10 rotor diameters downstream (Fig. 6.6 in the next section). The experimental study shows that the performance of the downstream turbine mainly depends on the streamwise distance between the turbines for the aligned configuration considered. Therefore, power reduction in this region can be improved if the turbines are placed apart such that they are minimally affected by wakes from turbines directly upstream. Noting that minimizing the cost of energy rather than maximizing the energy production per land area is a typical interest to a tidal-turbine-farm design. The far wake characterisation is essential to understand the interaction of turbines in arrays on power extraction. These will be investigated in detail in the next section.

6.3 Wake Field Analyses

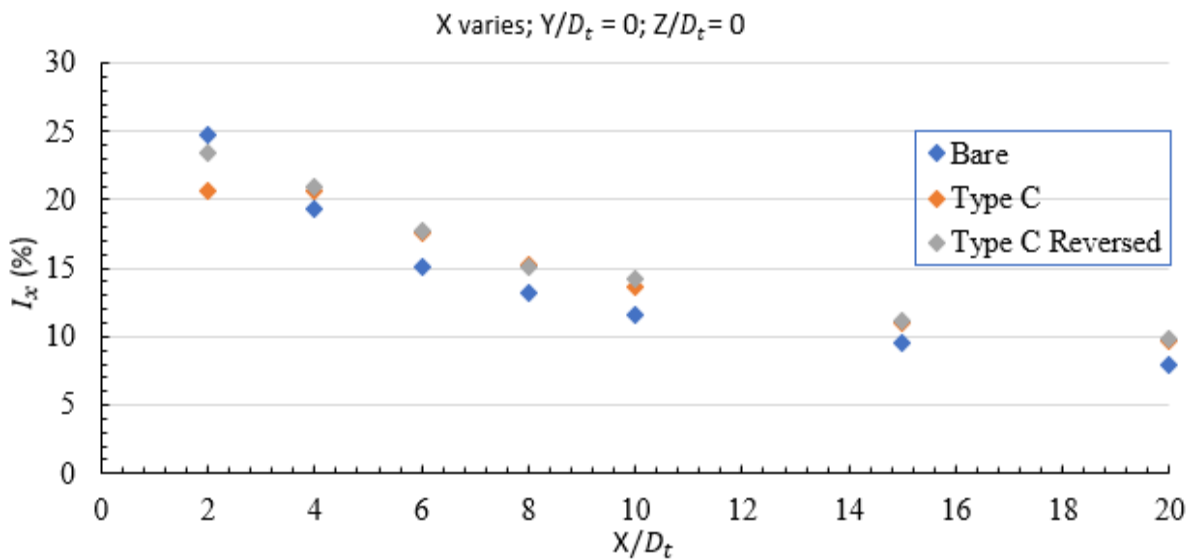
In this section, the far wake characteristics of the ducted turbines obtained from the physical modelling are discussed and compared to those of the bare turbine. Firstly, we analyse the far wake characteristics for a single turbine. Secondly, for the scenario of two in-line turbines with a separation distance of $10D_t$, we investigate the wake characteristics of the upstream turbine, and finally, in the presence of the operating upstream turbine, the wake characteristics of the downstream turbine is analysed and discussed.

6.3.1 Wake Characteristics of Isolated Turbines

The streamwise velocity averaged over the sampling time at a point in the turbine wake is referred to as u_x . In the experiments the incoming velocity u_0 was set at 0.42m/s and the turbines were under no-load condition. The variation of the mean centreline velocity ratio, u_x/u_0 with axial distance is shown in Fig. 6.6a, and the corresponding streamwise turbulence intensity, I_x is shown in Fig. 6.6b. The results in Fig. 6.6 show that, at the downstream side of the turbine, the velocity of incoming flow decreased but the streamwise turbulence intensity increased. The reduction of wake velocities and the increase in turbulence intensities were both larger for the ducted turbines than those of the bare turbine. All the devices show monotonically increasing trends for streamwise velocity and decreasing trends for turbulence intensity against the axial distance.



(a)



(b)

Figure 6.6. Streamwise distribution for a single row turbine (a) velocity ratio (b) turbulence intensity.

For the bare turbine, the velocities and turbulence intensities in the wake were less affected, and they recovered faster than those of the ducted turbines i.e., the bare turbine absorbed lesser energy from flow and exerted smaller effects on its wake than the ducted turbines. At the axial position of $X/D_t = 10$, the wake velocity ratio, u_x/u_0 recovered to 0.98 for the bare turbine, 0.93 for duct Type C and 0.91 for duct Type C Reversed while the turbulence intensity was still larger

than that of the incoming flow for all the devices (about 12% for bare turbine and 14% for both duct turbines). For the bare turbine, the wake velocity gradually recovered at and beyond the distance of $13 D_t$, and the turbulence intensity was smaller than that of the incoming flow. At the position $X/D_t=6$, both duct turbines had the same wake velocity and turbulence intensity but beyond this position, duct Type C recovered faster than duct Type C Reversed. For duct Type C, the wake velocity recovered to that of the incoming flow at about $X/D_t=19$ and the turbulence intensity was still slightly larger than that of the incoming flow. For duct Type C Reversed, the wake velocity fully recovered at $X/D_t=20$ with the turbulence intensity slightly smaller than that of the incoming flow.

At the axial locations of $X/D_t=4, 6$ and 8 , and $X/D_t=10, 15$ and 20 , the change in the ratio of u_x to u_0 along the z - and y -directions as well as their corresponding streamwise turbulence intensity, I_x are shown in Fig. 6.7a, Fig. 6.7b, Fig. 6.8a, and Fig. 6.8b respectively. For all devices, the vertical (z) profiles of the streamwise velocity ratio u_x/u_0 shows that u_x increases near the water surface and decreases near the seabed. The trend is not so apparent for turbulence intensities. The high velocity surrounding fluid mixes with the slow-moving fluid in the wake as axial distance increases thereby transporting momentum into the center of the wake. This causes wake expansion in the radial direction and a reduction in velocity deficit. At $X/D_t=4$ (Figs. 6.7a, b), the bare turbine has a greater velocity ratio than the ducted turbines across the entire vertical profile while all devices have the highest level of turbulence near the water surface and the lowest level of turbulence near the bed. The wake recovery region of the bare turbine is shorter than those of the ducted turbines. Beyond $X/D_t=8$ (Figs. 6.7a, b), the vertical profiles become fairly uniform. The turbulence intensity decreases with the axial distance and the profile becomes fairly uniform from $X/D_t=10$ onwards. At $X/D_t=20$, the variation in turbulence intensity is less than 2% over the entire depth for all the devices. The bare turbine has the least turbulence intensity level (8%) while the ducted turbines have turbulence intensities close to that at the inflow boundary. The present results are similar to those reported in Stallard et al. (2013) and Tedds et al. (2014). However, the development of wake velocity deficit was incomplete in the vertical direction due to the limitation of water depth (less than 4 rotor diameters). The profiles of u_x/u_0 along y -direction are shown in Figs. 6.7 and 6.8. The profiles are quite symmetric and are similar to the axisymmetric wake profile for wind turbines. The velocity profiles of the duct turbines have a larger velocity deficit in the central region as compared to that of the bare turbine

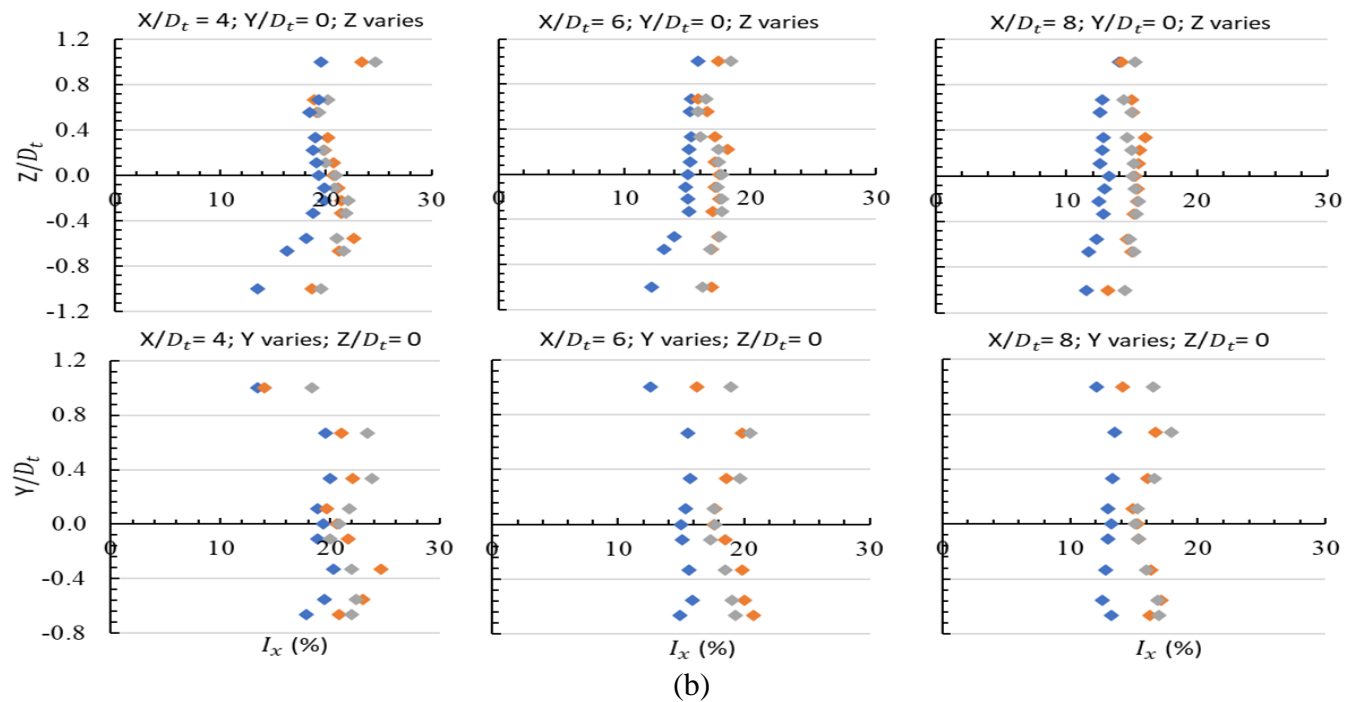
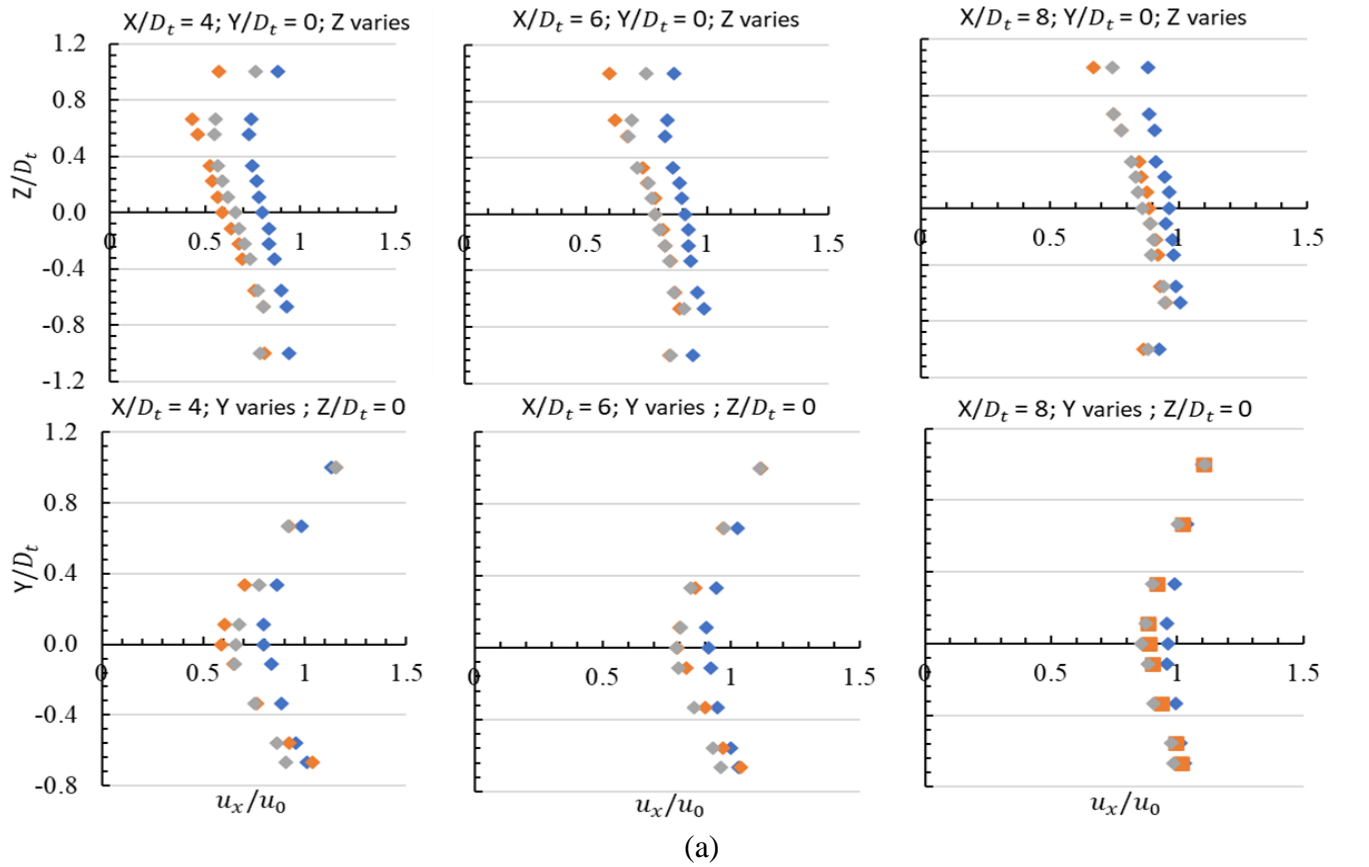


Figure 6.7. Streamwise vertical and lateral profiles (a) velocity ratio (b) turbulence intensity downstream of the single turbine at $x = 4D_t - 8D_t$. (Blue symbol – bare; orange symbol – Type C; grey symbol – Type C reversed).

At the outer region, all the velocity profiles nearly overlapped. The wakes gradually expanded with increasing downstream distance and finally approached the uniform inflow condition (i.e., beyond $X/D_t=10$). Their corresponding streamwise turbulence intensities, I_x gradually diffused and became fairly uniform with increasing downstream distance and approached the inflow condition (at $X/D_t=15$ and 20). The results imply that additional turbine(s) can be placed within the accelerated lateral positions, say $Y/D_t \geq \pm 1.0$ where the flow is greater than the inflow current velocity. Though the development of wake velocity deficit was incomplete in the lateral direction due to the limitation of channel width, the wake characteristics are qualitatively similar to those of the previous studies (Harrison et al., 2010; Maganga et al., 2010; Myers & Bahaj, 2012; Mycek et al., 2014; Ceccotti et al., 2016).

For all devices, the velocity deficit (Fig. 6.8a) is slightly less than zero ($u_x/u_0 > 1$) at $|z| < 4$ and $|y| > 0$ for $X/D_t=15$ and beyond, which implies that within these regions, the wake velocity is slightly greater than the inflow velocity. In general, turbulence enhanced wake mixing and velocity recovery. In this study, about 13 rotor diameters for the bare turbine and 20 rotor diameters for the ducted turbine is required for the velocity profiles returning to the uniform inflow velocity profile. Previous experiments demonstrated that centerline velocity deficits are still appreciable at 10 rotor diameters downstream and that streamwise spacing between two in-line turbines could be in the order of 15–20 rotor diameters (Myers et al., 2008a, 2008b). The presence of the turbine support structure has a significant effect in the near wake (within $X/D_t=2$ downstream) inducing a significant velocity deficit and enhancing the turbulence intensity.

The evolution of the mean centerline streamwise velocity downstream of the bare rotor, illustrated in Fig. 6.9, compares qualitatively well with published data (Maganga et al., 2010; Stallard et al., 2013; Tedds et al., 2014; Chen et al., 2017; Zang et al., 2019). Previous studies have shown that a direct comparison may not be really possible as a result of the interdependency of wake velocity reduction and rate of recovery of wake velocity on several factors. The spread of data could be due to the range of turbulence intensities and variations in the thrust and turbine model. In Maganga et al. (2010) a different model turbine was used, and the flow was of higher turbulence intensity (25%) and with a lower blockage ratio of 5%. The resulting velocity deficit was lower than that of the present study (blockage ratio 10%) in the wake region ($X/D_t < 6$), and the velocity recovery rate was similar to that of the present study

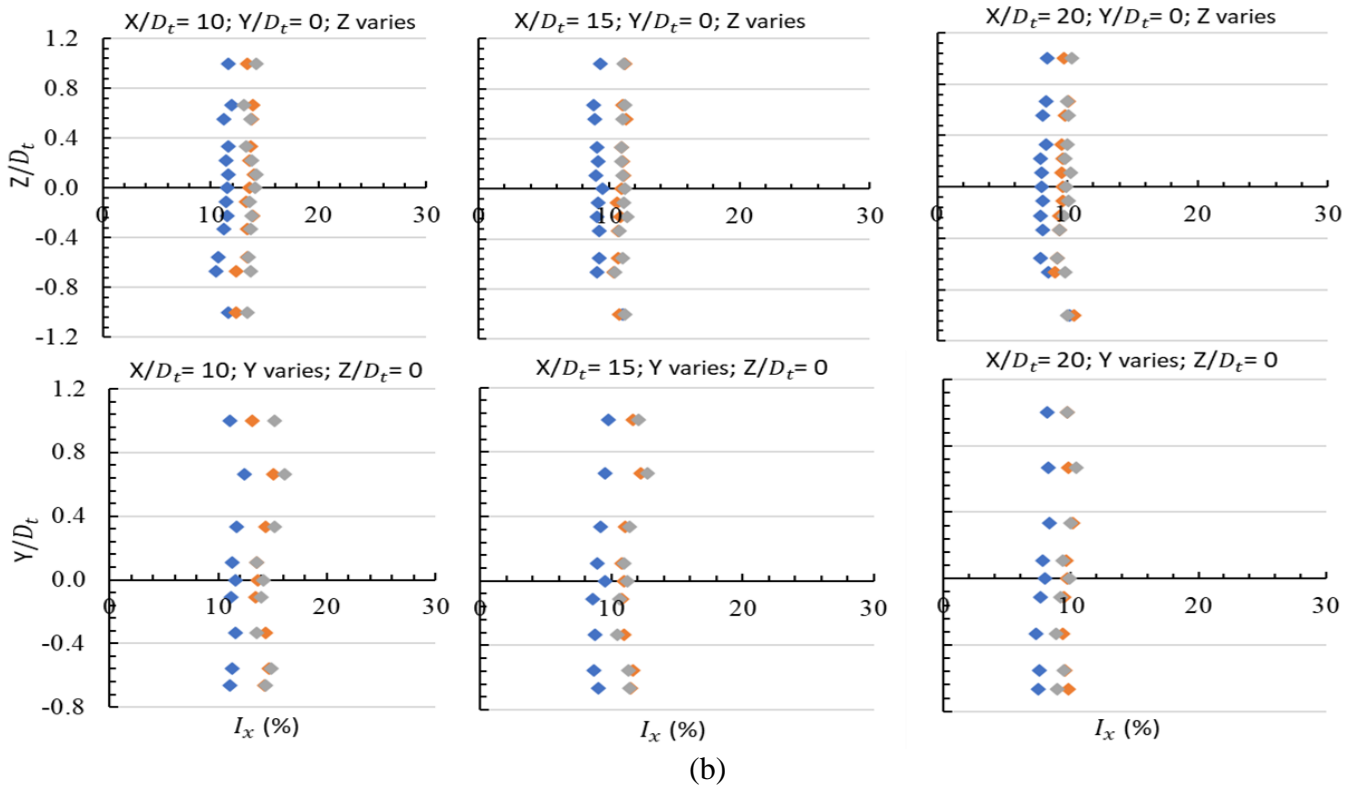
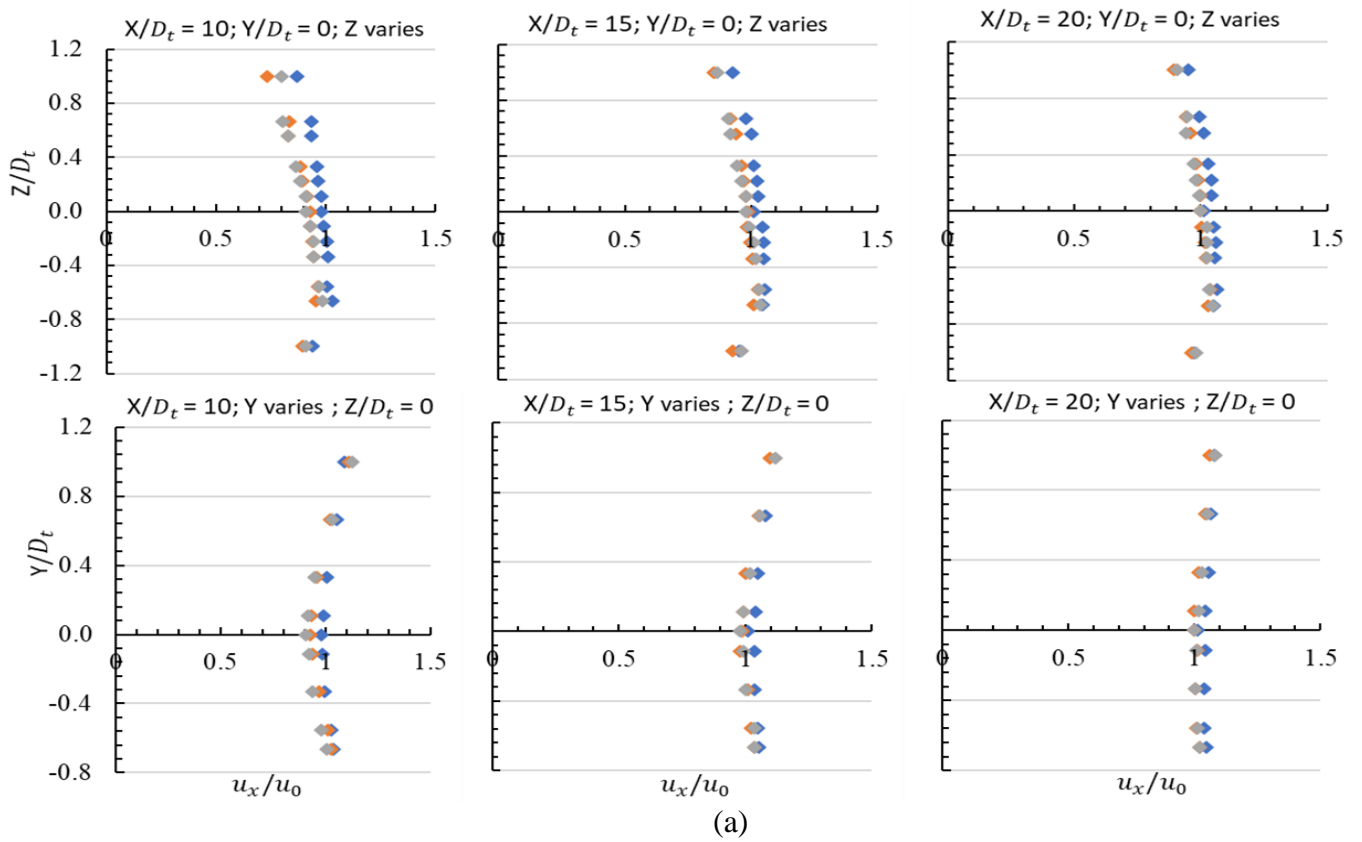


Figure 6.8. Streamwise vertical and lateral profiles (a) velocity ratio (b) turbulence intensity downstream of the single turbine at $x = 10D_t - 20D_t$. (Blue symbol – bare; orange symbol – Type C; grey symbol – Type C reversed)

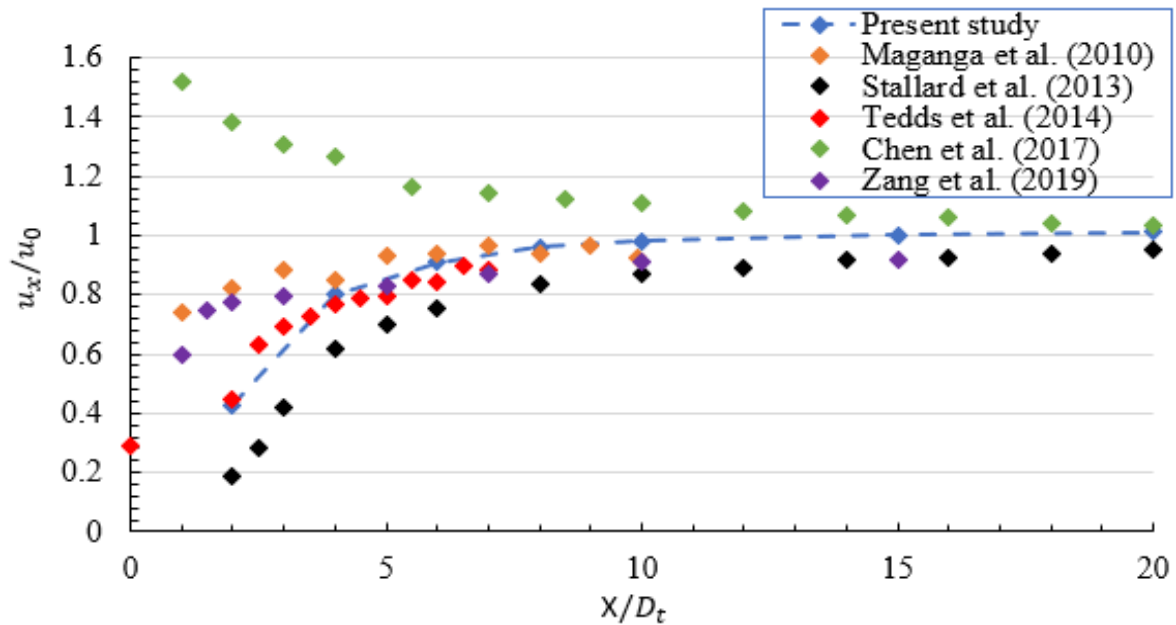


Figure 6.9. Normalised velocity for the bare turbine against published data.

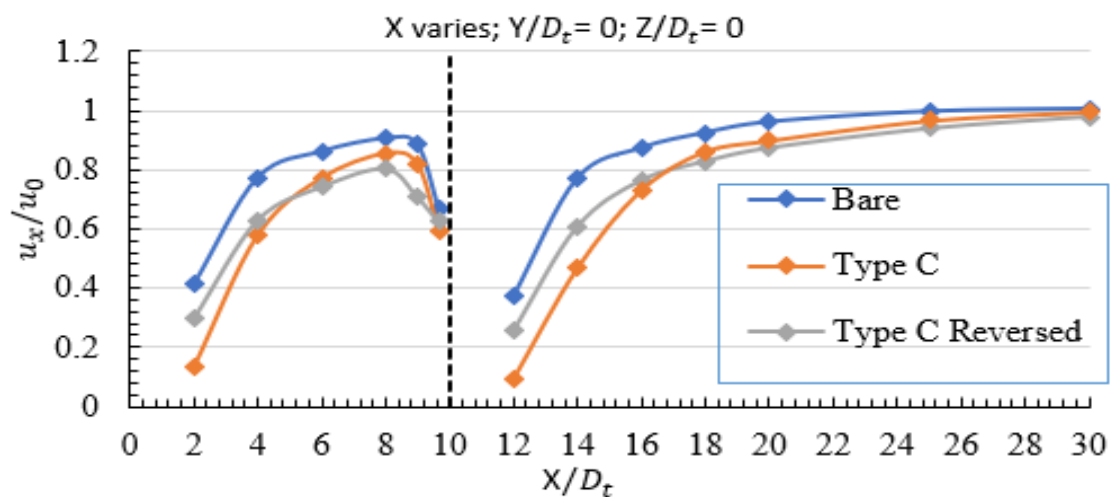
beyond $X/D_t=8$. One cause of the difference in the results may be due to the difference in the blockage ratio used. A higher blockage ratio will cause a measurable increase in thrust coefficients and bypass flow velocity (and hence the wake recovery length scales). Stallard et al. (2013) employed a lower blockage ratio of 2.5% (inflow turbulence intensity of 10%) and the results gave a slower flow recovery as compared to that of the present study (blockage ratio of 10%). Chen et al. (2017) employed a higher blockage ratio of 16.4% (inflow turbulence intensity of 2%), the results gave a more rapid flow recovering rate for the model turbine investigated. Zang et al. (2019) employed a blockage ratio of 8.7% (inflow turbulence intensity of 10%) and the results showed that the velocity deficit was smaller at the near wake zone ($X/D_t < 5$) and the flow recovery rate is slower beyond $X/D_t=5$, as compared to those of the present study. A much longer distance ($>20D_t$) would be required for the velocity to return to the incoming velocity. The longitudinal variation of velocity deficit in the experiments by Tedds et al. (2014) compares qualitatively and quantitatively well to that of the present study. Their experimental test condition was of inflow turbulence intensity 2% and blockage ratio of 16%, resulting in a maximum difference of about 7% in velocity compared to the present study.

The rate of wake recovery for the ducted turbine could be more affected by the surrounding boundaries due to its close proximity to the seabed and water surface (flow depth is less than 4 rotor diameters), which would constrain vertical expansion of the wake leading to a slower-

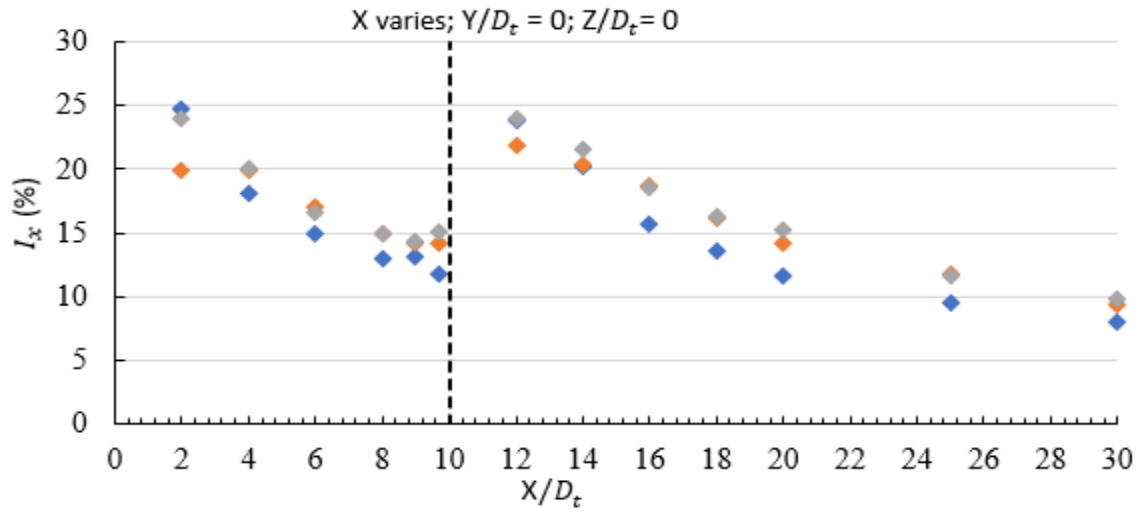
moving region of flow on the underside of the wake thus persistence of the wake far downstream than it would affect the bare turbine (Myers et al., 2008a, 2008b; Myers & Bahaj, 2010). Also, the flow in the ducted turbine has a combination of duct and rotor wake effects. The flow surrounding the centerline axis has the greatest wake effect with a significantly low velocity compared to the bare turbine. This can be attributed to the additional flow losses induced by the presence of the duct and thus, a high turbulence intensity than that observed for the bare turbine. Hence, results presented so far demonstrated that several interdependent variables affect the rate of wake recovery and will have a significant impact on the spacing of marine current turbines within an array. The extent and structure of the wakes of each turbine created downstream will be most important for the determination of the inter-device spacing layout of an array of turbines. In the next section, we shall examine the evolution of the flow field in the presence of two operating tidal turbines axially separated by ten rotor diameters.

6.3.2 Wake Characteristics for Two In-line Turbines

Measurements of the streamwise velocity along the centerline of two in-line turbines were conducted and the results are shown in Fig. 6.10. In Fig. 6.10, the locations $X/D_t = 12, 14, 16, 18, 20, 25$ and 30 correspond to $X/D_t = 2, 4, 6, 8, 10, 15$ and 20 respectively if the position of the downstream turbine is taken to be zero. Presently the position of the first turbine is set to zero and the position of the second turbine is at $X/D_t = 10$.



(a)



(b)

Figure 6.10. Streamwise distribution of two axially aligned turbines (a) velocity ratio (b) turbulence intensity.

For the upstream turbine, the variation of the streamwise velocity along the centerline is very close to that for an isolated turbine in the near wake region ($X/D_t < 5$) for all cases (Fig. 6.10a). The blocking effect of the downstream turbine becomes apparent in the region of $X/D_t > 5$, the recovery rate of the streamwise velocity is reduced and the peak value of u_x/u_0 is about 0.9 for bare turbine, about 0.85 for Type C turbine, and about 0.8 for Type C reversed turbine. The location of the peak is around $X/D_t = 8$ for all cases. Further downstream the streamwise velocity is reduced due to the significant blocking effect of the downstream turbine. The approaching velocity to the downstream turbine can be inferred from Fig. 6.6a. For bare turbine, $u_x/u_0 \sim 0.98$; for Type C turbine, $u_x/u_0 \sim 0.9$, for Type C Reversed turbine, $u_x/u_0 \sim 0.92$. The lower approaching velocity ($u_x/u_0 < 1$) causes a lower velocity in the wake region. The velocity at $X/D_t = 12$ in Fig. 6.10 is less than the velocity at $X/D_t = 2$ in Fig. 6.6a. Also, a longer distance is required for the recovery of the velocity to the inflow value. A distance of about $20D_t$ is required (Fig. 6.10) compared to the distance of about $15D_t$ for an isolated turbine (Fig. 6.6a).

For the turbulence intensity downstream of the upstream turbine, the spatial variation is very close to that of the corresponding turbine in isolation in the near wake region, $0 < X/D_t < 8$, for all cases (cf. Fig. 6.6b and Fig. 6.10b). The effect of the downstream turbine is negligible. At the region near the downstream turbine ($8 < X/D_t < 10$), the blocking effect of the downstream turbine enhances the turbine intensity slightly. For the turbulence intensity downstream of the

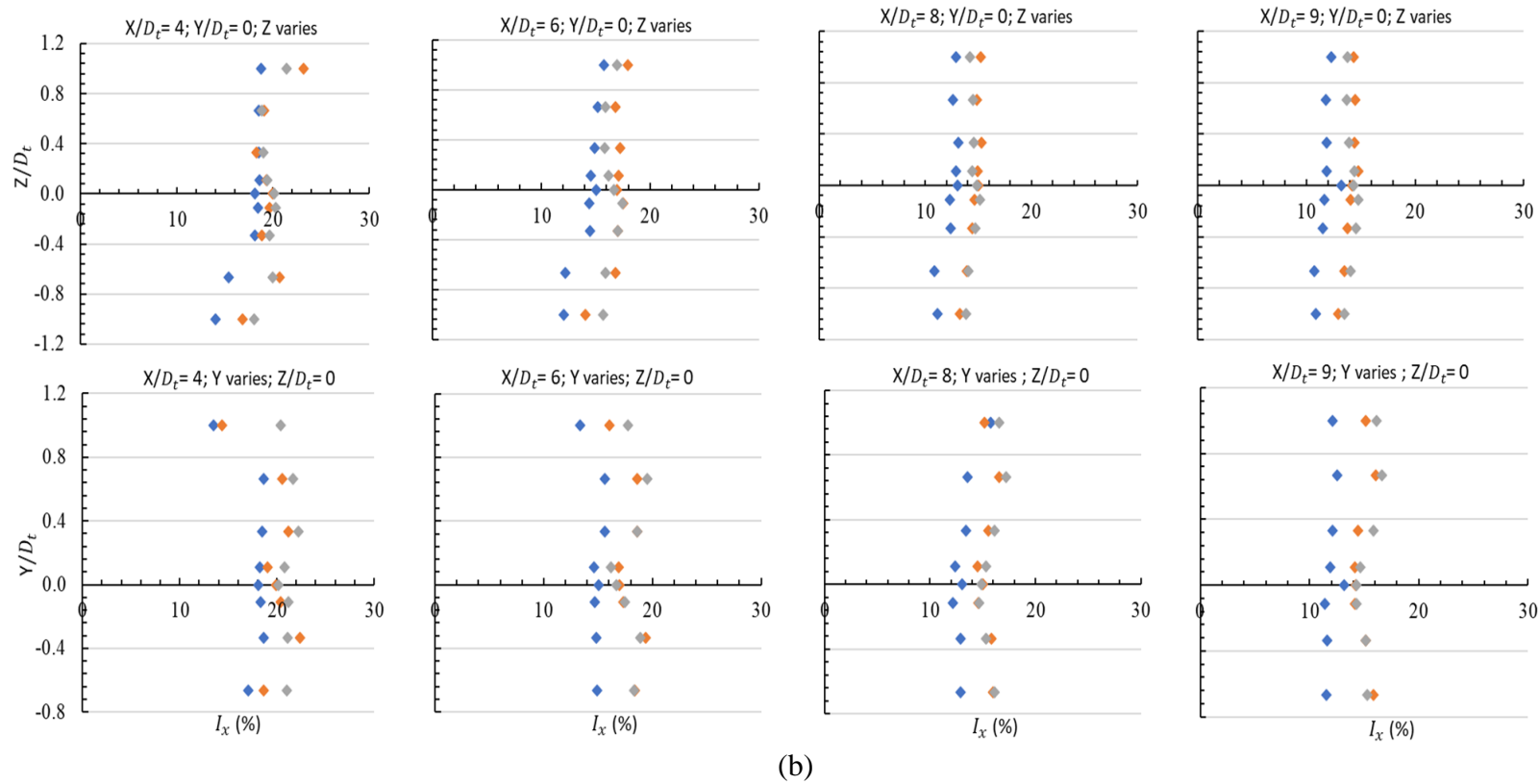
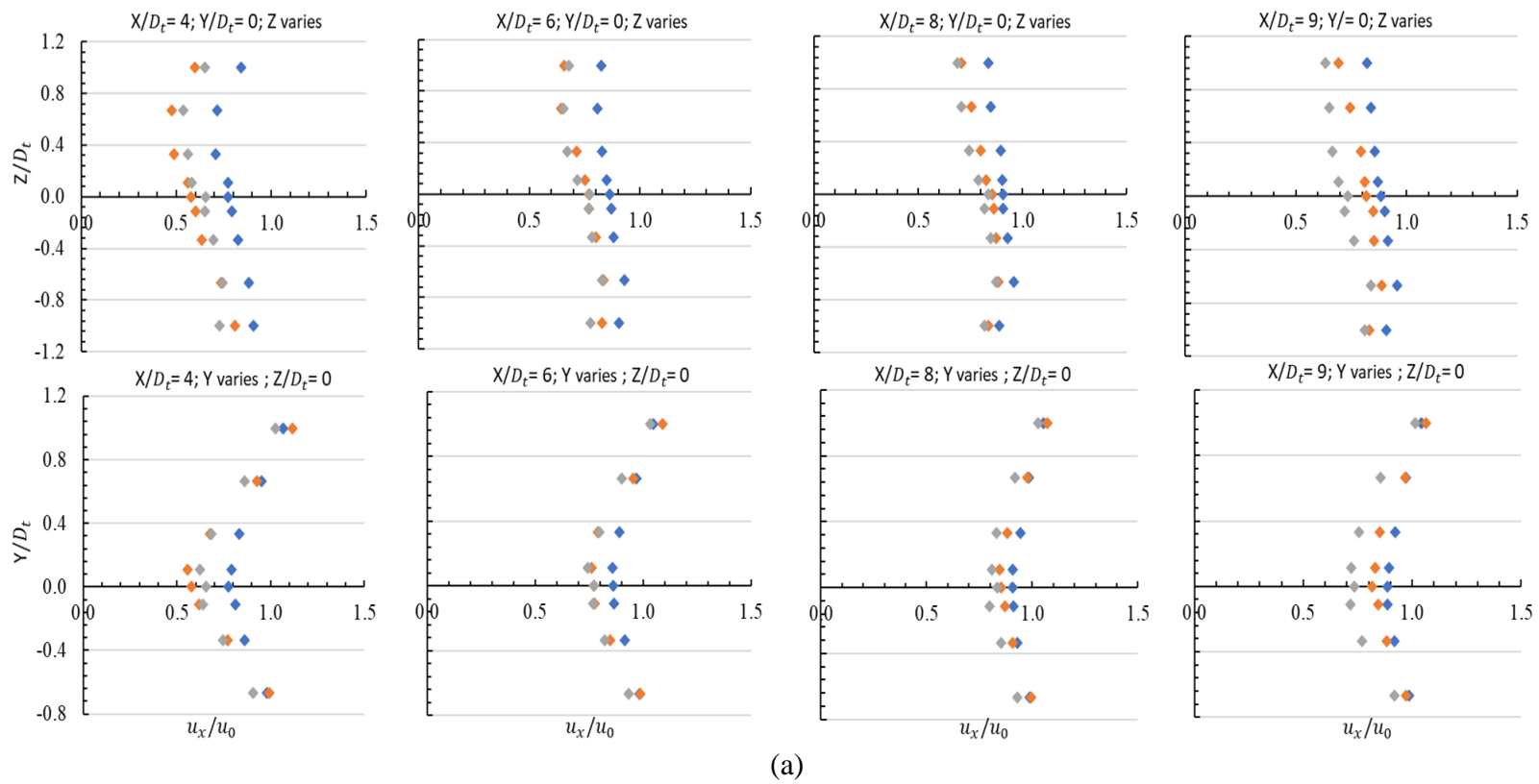


Figure 6.11. Streamwise vertical and lateral profiles (a) velocity ratio (b) turbulence intensity between the wake of the upstream turbine and upstream of the second turbine at $x = 4D_t - 9D_t$.

downstream turbine, the spatial variation is close to that of the corresponding turbine in isolation in the far wake region ($X/D_t > 16$) for all cases. The turbulence intensity is slightly enhanced in the near wake region ($10 < X/D_t < 16$). This may be due to the incoming velocity profile towards the downstream turbine is not perfectly uniform due to the disturbance of the upstream turbine.

Further comparison of Fig. 6.6a and Fig. 6.10 shows that at $X/D_t=24$ and beyond, the streamwise velocity profile of the downstream turbine superimposed that of the isolated turbine for the bare turbine (cf. Fig. 6.6a at $X/D_t=15$). That is, within this region, the second downstream turbine appears as if it is operating in isolation. In this region and beyond, the wake in the downstream turbine persisted compared to the isolated case for the ducted turbines. Thus, full recovery is extended beyond $X/D_t=30$ considered in the present study for the two in-line ducted turbines.

Figure 6.11 illustrates the vertical and lateral variation of the streamwise velocity and turbulence intensity at different locations within the region between the upstream turbine ($X/D_t=0$) and downstream turbine ($X/D_t=10$). The profiles are similar to those of the corresponding isolated turbine. At $X/D_t=9$, there is velocity reduction of the profile as compared to the corresponding profile at $X/D_t=8$ for both cases of ducted turbines. This is due to the interferences of the corresponding downstream ducted turbine. For turbulence intensity, the profiles at $X/D_t=9$ are quite similar to the corresponding profiles at $X/D_t=8$. It appears the presence of the downstream turbine only affects the magnitude of the velocity and turbulence intensity at a short region (about a rotor diameter length) upstream and does not affect the lateral and vertical variation of the quantities.

The vertical and lateral variations of the streamwise velocity at the region downstream of the second turbine are illustrated in Fig. 6.12a and Fig. 6.13a. The corresponding variations of streamwise turbulence intensity, I_x are illustrated in Fig. 6.12b and Fig. 6.13b respectively. For all devices, the vertical profiles are similar to those of the corresponding isolated turbine (Figs. 6.7 & 6.8), except that the velocity deficit is larger. Similar to the isolated cases, at $X/D_t=20$ and beyond, the velocity profiles are nearly symmetric and approach uniform for all cases (Fig.6.13a). Further downstream (at $X/D_t=30$), the velocity deficit is less than zero at $|z| < 0.7D_t$

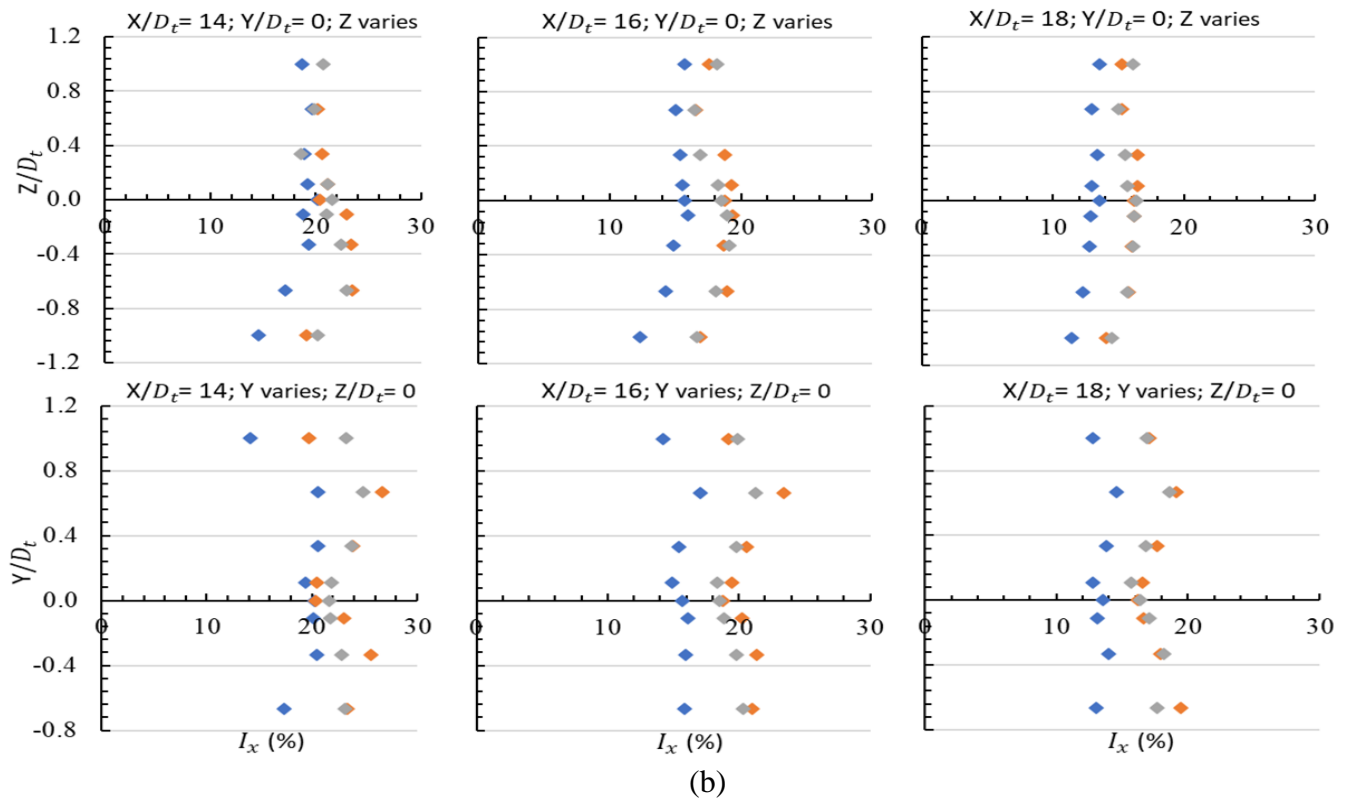
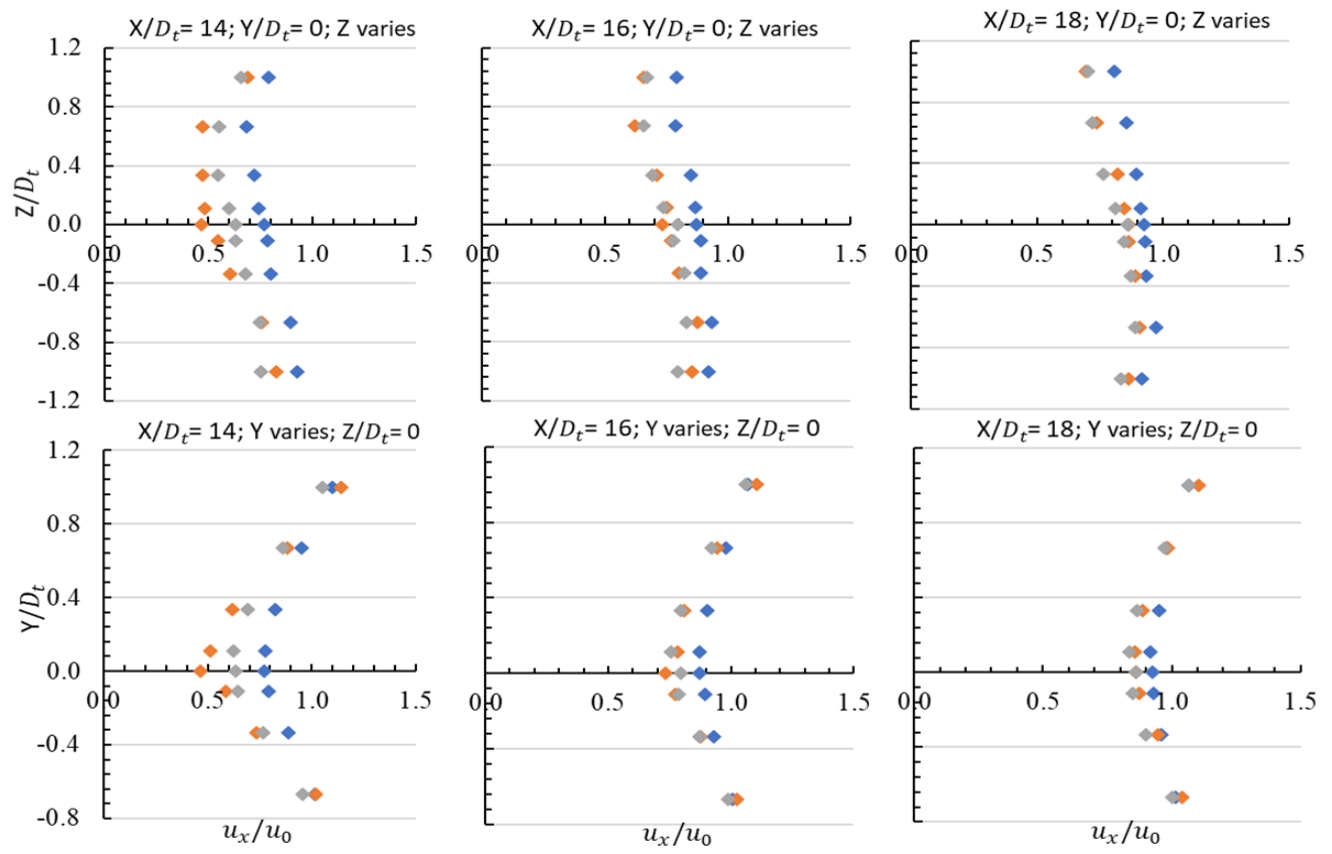
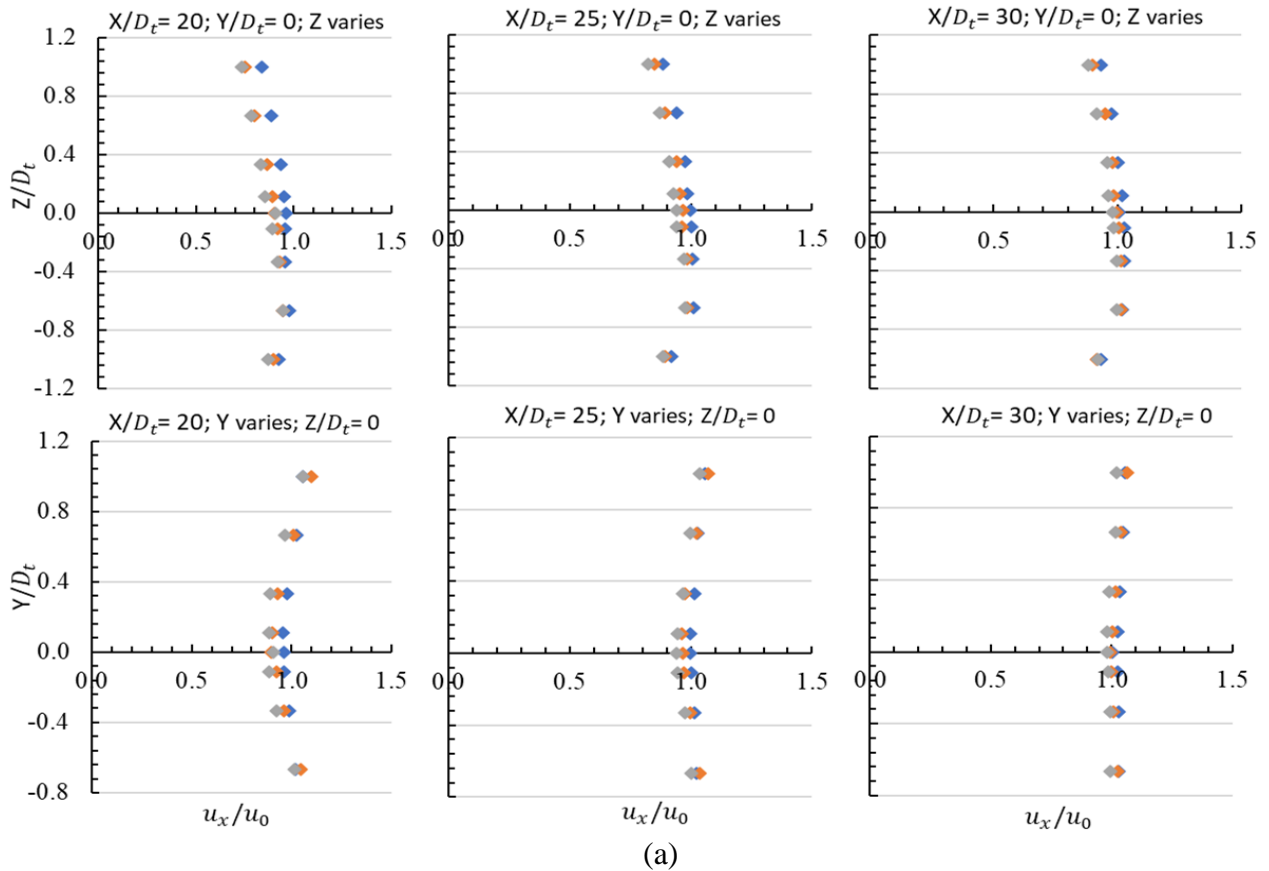


Figure 6.12. Streamwise vertical and lateral profiles (a) velocity ratio (b) turbulence intensity downstream of the second turbine at $x = 14D_t - 18D_t$.

for the case of bare turbine and at the surrounding region below the hub for the cases of ducted turbines. This implies that the flow is still not perfectly uniform there. Also, for all cases, the turbulence intensity decreases with the streamwise distance and the profiles at $X/D_t = 20$ and beyond are quite uniform. At $X/D_t = 30$, the variation in turbulence intensity is less than 2% over the entire depth (Fig.6.13b). For each case, the profiles are very similar to those of the corresponding case of isolated turbines.

The lateral profiles (Figs. 6.12 &– 6.13) are very similar to those of the corresponding isolated turbine (Figs. 6.7 & 6.8). Similar to the isolated cases, at $X/D_t = 4$ and beyond, the velocity profiles are symmetric around the centerline ($Y/D_t = 0$). For the bare turbine (Figs. 6.13a), the velocity ratio is greater than unity (i.e., accelerated) over the lateral width variation ($-0.7 \leq Y/D_t \leq 1$) from $X/D_t = 20$ and beyond. For duct Type C, the velocity ratio is accelerated at $X/D_t = 30$ over the width variation $|y| > 0.3$, while duct Type C Reversed is accelerated over the width variation $|y| > 0.7$ from $X/D_t = 20$ and beyond. For all devices and at $X/D_t = 30$, the variation in individual turbulence intensity over the entire lateral width is less than 1%.



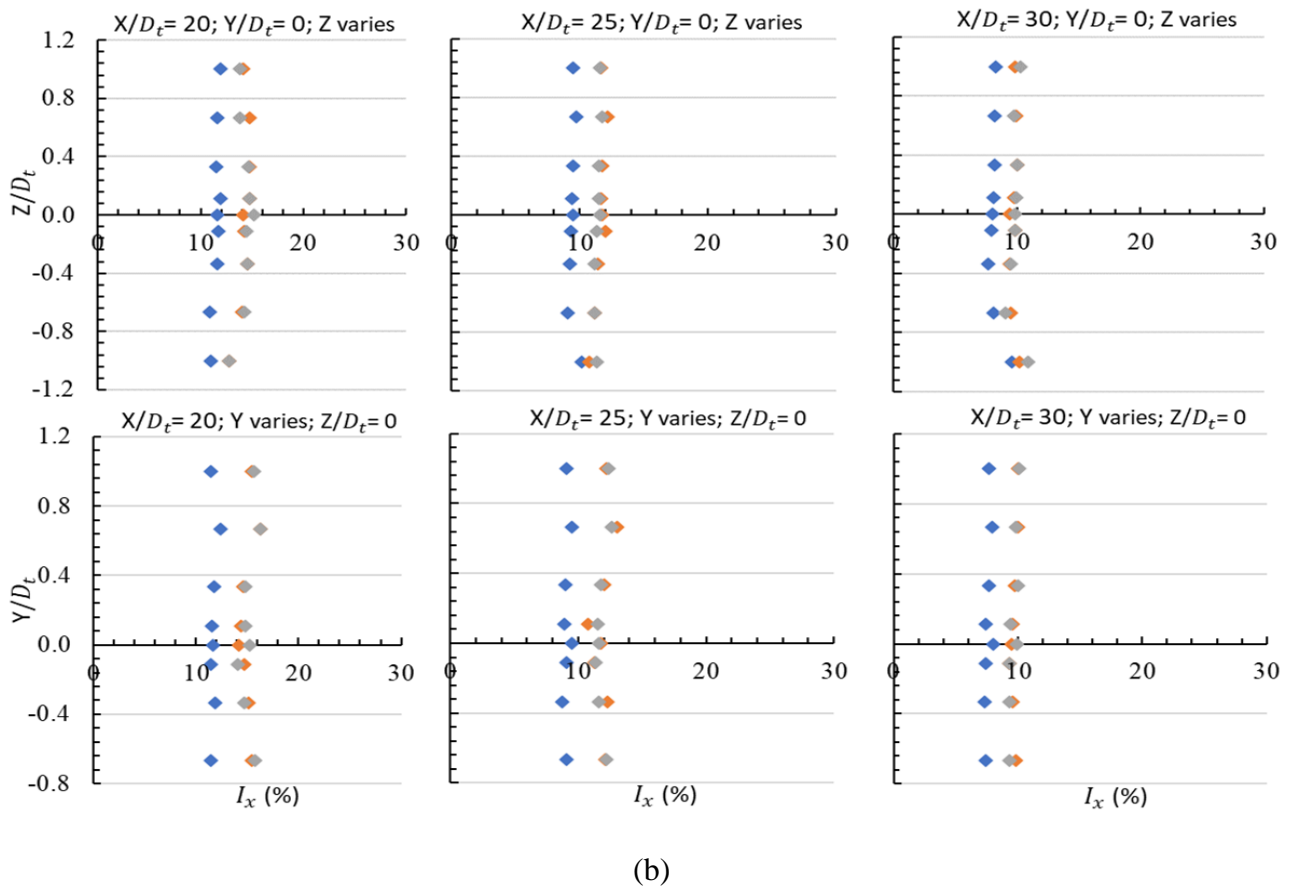


Figure 6.13. Streamwise vertical and lateral profiles (a) velocity ratio (b) turbulence intensity downstream of the second turbine at $x = 20D_t - 30D_t$.

CHAPTER SEVEN

Conclusions and Future Work

The overarching summary of the main conclusions drawn from the analyses presented in chapters 4 and 6 are outlined in section 7.1. Suggestions for future work are given in section 7.2. Section 7.3 highlighted the interesting contributions made by this thesis to shaping ongoing research in the actualization of a fuller picture of tidal farm efficiency.

7.1 Conclusions

There is growing concern over the threat posed by global climate change and as a result, has led to an increased interest in the research and development of renewable energy technologies. In order to diversify global energy contributions, marine renewable energies have been thrown into the mix as it offers one of the largest untapped sources of renewable energy. In recent years, marine renewable energies have gained tremendous interest with emerging technologies nearing the industrial stage. Among these untapped renewable energy sources is tidal current energy with the promise of regular and predictable production of electricity. Efforts to increase the mass flow through the turbine substantially along with the alignment of the wake flow in a bid to bringing tidal energy converters closer to a successful deployment of full-scale tidal farms remains a challenge to tidal developers. Decades of studies on the use of ducts around a turbine rotor has been identified to enhancing the performance of wind and tidal turbines due to the generation of a high suction region behind the duct through vortex formation. Based on research and development attained, two conventional types of ducts have been proposed for wind and tidal turbines: unidirectional ducts and bidirectional ducts. However, it is envisioned that the efficient and cost-effective deployment of full-scale tidal farms solely depends on the progress in finding optimum duct shape (or size), blade design, and turbine array layout. In recent times, a duct equipped with a flange (referred to as a wind-lens) has attracted extensive attention due to its promising narrative. Unlike the traditional early designs of ducted turbines that rely on increasing the area ratio between the inlet and duct exit diameters, it depends on creating a low backpressure region through a strong vortex formation behind its broad flange and hence, a substantial increase in the wind speed. Although wind-lens has demonstrated significant power

augmentation, a vast majority of investigations on wind-lens designs are mainly based on several existing typical shapes. Therefore, convergency towards the best wind-lens design profile has not yet been achieved. The flanged duct profile in the present study has a curved flange at the rear end and served to increase the pressure drop in the wake region thereby increasing the approaching velocity by converging the flow into the duct. It also has a flap at the front end to reduce the inlet loss and outlet loss in the forward flows and reverse flows respectively. It is expected that energy extraction from tidal currents is poised to make the quantum leap to full-scale tidal-farm deployment in the near future. This study carried out a thorough analysis of the hydrodynamics of flanged duct tidal turbines. The analysis was performed using data obtained from numerical and experimental modelling of flanged duct tidal turbines in isolation or within an array. At the outset of this research, this study is the first to ever place emphasis on the array of flanged duct turbines in bi-directional tidal flows. In the numerical simulation, several carefully designed flanged duct tidal turbines with different duct shapes (symmetric and asymmetric) for both uni-directional flow and bi-directional flow were investigated for power augmentation and hence propose an optimum design. This assessment employed a numerical actuator disk that provides an axial resistance to the flow, and thus models the extraction of linear momentum. Based on the proposed optimum flanged duct type (i.e., duct Type C) obtained from the numerical simulation, the physical modelling was carried out and focused on a low-budget small scale testing which is only achievable at laboratory facilities. The experiment was conducted in an open-channel recirculating water flume with a 1:200th scaled flanged duct tidal stream model. This model setup represents a turbine of diameter 20m in water depth of 44.4m. The experimental data sets were used to explore flanged duct performance and far wake characteristics of flanged duct turbines in isolation and multiple arrays for both forward and reverse flows. Raw data sets were obtained using a Prony brake and a side-looking ADV. Analysis was presented in terms of power performance, wake velocity ratios and turbulence intensities. In both numerical and physical modelling employed in this study, the main conclusions are drawn from the comparisons of the performance and interaction effects between flanged duct tidal turbines and the bare (non-duct) turbine in isolation or in an array and are summarised here.

In Numerical Simulation:

The maximum power delivered per rotor area by the asymmetric duct Type (C and Reversed C) is about 60% higher than that of a bare turbine while that of symmetric duct Type (D) is almost similar to the bare turbine. The significant improvement in the power output achieved by the asymmetric duct Type (C and Reversed C) was due to the curved flange at the rear end of the duct and arc flap at the duct inlet. The former feature served to generate an increased low backpressure region through a strong vortex formation while the latter ensured no inlet losses by streamlining flow into the rotor plane and along the duct walls. This inherent simultaneous action led to a significant increase in inflow swallowing and transmission capability of the duct entailing a larger low-pressure zone. The close peak power coefficients obtained by the best performing duct type (Type C) in both forward and reverse flows further revealed that a curved flange and inlet-flap type is preferred for a wind-lens profile. The performance of a flanged duct is significantly affected if there exists a separation inside the diffuser. Therefore, the incorporation of the inlet-arc flap and the shape of the inlet-arc flap and flange is a strong determinant of the nature of the flow inside and around the duct and downstream. The effect of the blockage ratio on the peak power coefficient showed that peak performance increases with the blockage ratio for all devices. The ratio of the peak power coefficient of ducted turbine over the peak power coefficient of bare turbine varies little with the blockage ratio, with duct Type D giving the least ratio. In general, although the actuator disk model was chosen in the present CFD simulation to allow for a fair and straightforward comparison of duct performance, the power extraction was over-predicted. Therefore, the performance reported here is the upper bound value corresponding to an ideal rotor (no energy loss) with an infinite number of blades. This assumption may not be accurate if the turbines are close together as interaction among turbines may exist due to the swirling motion of blades.

In Experiment:

Power Performance

For the single isolated devices, the power coefficient - *TSR* curve is relatively short spanning, with a *TSR* less than 4, typical for a tidal stream rotor solidity. The flanged duct turbine

exhibited a superior peak performance (power per rotor area) in the amount of 25% for duct Type C and 36% for duct Type C Reversed compared to the peak performance of the bare turbine. The peak power coefficient obtained for the flanged duct turbines is within the range of a 200 kW OpenHydro demonstrator device i.e., about 0.3 with a 2.5m/s rated flow speed. Computational results were in good agreement with the corresponding experimental data, albeit at increased magnitude. This implies that duct Type C may well perform if installed in both flood and ebb current flows. The normalized power performance curves further reveal that both results have a good qualitative correlation for all the devices.

For the two axially aligned devices, the investigations illustrated that the downstream turbine in the presence of an operating axially aligned upstream turbine performed poorly compared to the performance of the single isolated turbine. The underperformance of the downstream for each of the individual devices is least for the bare turbine (i.e., 20%) followed by duct Type C (i.e., 22%) and most for the duct Type C Reversed (i.e., 25%). However, the peak power coefficients of the downstream ducted turbines were still higher than that of the downstream bare turbine.

Wake Characterisation

For the isolated system, all devices showed that the velocity of incoming flow decreases while the corresponding streamwise turbulence intensity increases as the flow passes through the turbine. The decreasing range of wake velocities and the increasing range of turbulence intensities were both the largest for the ducted turbines and the smallest for the bare turbine. However, all devices show monotonic increasing and decreasing trends for the variations of wake velocities and turbulence intensities with increasing axial distance. Across the axial distance downstream, the bare turbine absorbed lesser energy from flow and exerted smaller effects on its wake than the ducted turbines. The wake velocity ratio reached 0.98 for the bare turbine, 0.93 for duct Type C and 0.91 for duct Type C Reversed and turbulence levels remain at approximately 12% for the bare turbine and 14% for the ducted turbines compared to approximately 10% inflow turbulence level. Full recovery of flow was detected at about 13 and 20 rotor diameters for bare and ducted turbines respectively. The turbulence intensities at those respective axial distances were slightly smaller than that at the inflow boundary. The velocity ratio profile in the bare rotor wake compares well with the published data from a recirculating

water flume/channel. The spread in data was identified to be due to the differences in the range of turbulence intensities, blockage ratio (thus, variations in the thrust) and turbine model. The rate of wake recovery for the ducted turbine could be more affected due to it is closer to the seabed and water surface (flow depth is less than 4 rotor diameters). This would constrain vertical expansion of the wake leading to a slower-moving region of flow on the underside of the wake thus wake flow persists farther downstream than the bare turbine. For the ducted turbines, the flow experiences a combination of duct and rotor wake effects. Therefore, the flow around the hub axis has the greatest wake effect with a significantly low velocity compared to that for the bare turbine. This was attributed to the additional flow losses induced by the presence of the duct and thus, a high turbulence intensity than that observed for the bare turbine. Across the depth of the test channel, the velocity recovers faster for the bare turbine than that for the duct turbines just as the turbulence intensity dissipates. Beyond 8 rotor diameters, the velocity deficit profile across the depth of the test channel is close to symmetric and returns to a fairly uniform deficit for all devices. Across the width of the test channel, the wake velocity ratio profile is symmetric about the hub center with a fast-moving flow bounding its far ends for all devices. This is akin to the axisymmetric wake profile in wind turbine wakes. Beyond 10 rotor diameters, the wake gradually expands with increasing downstream axial distance until it fairly approaches the inflow condition across the width of the test channel.

For the two axially aligned arrangements, the profile of each wake behind two turbine arrangements remains similar to that of an isolated turbine, but at a slower flow recovering rate than in the isolated turbine case. The wake profile approaches that of an isolated turbine as the axial distance downstream is increased. For the bare turbine, from 24 rotor diameters downstream and beyond, the velocity ratio of the downstream turbine is the same as that of the isolated turbine (correspondingly at 15 rotor diameters downstream and beyond). At these distances, the second downstream turbine operates as if it is in isolation. For the ducted turbines, unlike in the isolated case, the wake flow ratio persisted beyond 30 rotor diameters downstream considered for the two ducted turbine arrangement with the turbulence is slightly less than the upstream conditions. However, the peak power coefficients of the downstream ducted turbines are still higher than that of the downstream bare turbine. Therefore, the deployment of additional ducted turbines in a tidal farm may have an advantage. Although, the precise economic estimates of energy cost are unavailable at the present state of development. The results demonstrated that

several interdependent variables affect the rate of wake recovery and will have a significant impact on the spacing of marine current turbines within an array.

In general, we acknowledge that the small-scale experimental setting used in the present investigation cannot replicate the turbulent flow and complex environmental variability that exist at real tidal energy sites. More so, this study focused on the analysis of the hydrodynamic performance and far wake impact on flanged duct turbine in bi-directional tidal flows, while other important factors such as flow fluctuations due to waves, reliability, and maintenance cost were not considered. However, a comprehensive set of experimental data have been produced which will provide useful design information that will guide the course of future marine current turbine research and suitable data for validating theoretical and numerical methods.

7.2 Recommendations for Future Study

This research has investigated the hydrodynamics as well as the formation and nature of the wake region downstream of flanged duct tidal turbines. The originality of this study is that it is the first study to focus on the array of flanged duct turbines in bi-directional tidal flows, with the optimal duct shape determined by numerical simulations, and has provided opportunities for future work which will create new insights into the search for cleaner, cheaper solutions to the ever-increasing demand for energy as it offers hope in the development of tidal farms. Based on the results obtained from this experimental investigation, the following future investigations are suggested.

- Further physical measurements of duct turbine wake characteristics are required to confidently identify mixing and wake interaction on an array level. Also, considerations of the effects of the various realistic flow conditions that may be encountered at tidal sites are recommended to develop a fuller picture of tidal farm efficiency. These include:
 - Experiments conducted in a wider testing flume with additional measurements of rotor thrust and torque (utilising a dynamometer) and rate of rotation (via optical sensors) is recommended.

- Measurements using a PIV system would be interesting as they can provide further insight and visual investigation of complex flow fields on wake evolution and the location of vortex structures in the near and the far wake.
- The preliminary simulations presented in this thesis were modelled using the actuator disk model. For a more complete detailed CFD modelling which permits to consider the effects of swirl in the flow, based on real rotor geometry and blade aerodynamic coefficients and allow for a better comparison with the experimental results, it would be very interesting to carry out simulations using a 3D CFD-embedded blade element momentum model. This model is a computationally efficient method of calculating the power output based on previous studies. Additional CFD simulations to develop numerical models in a wide range of flow conditions using the present experimental data for calibrations would provide more insights into the actualization of tidal farms. An extension of the work of Garrett and Cummins (2007) for a bare turbine to include a ducted turbine would be an interesting 1D mathematical model to develop.
- The present study has identified an optimum flange duct profile that may well be deployed in both flood and ebb current flows. Further shape optimization is recommended using a combination of CFD calculation and a multi-objective genetic algorithm (GA) process through varying design parameters. This effective shape design optimization method has been used by Liu et al. (2016).

7.3 Contributions of Thesis

The main contributions of this thesis are:

Analysis of hydrodynamic of ducted turbines

Previous studies demonstrated that adding a duct over a turbine leads to significant power augmentation. A recent duct type of interest is the wind-lens profile but a vast majority of investigations on wind-lens designs are mainly based on several existing typical shapes. Therefore, the wind-lens design profile is still far from optimal. The present study focused on the

hydrodynamics of several wind-lens design profiles and demonstrates that a wind-lens equipped with a curved flange and inlet flap is preferred. Interestingly, the close peak power coefficients obtained by the best performing duct type (Type C) in both forward and reverse flows further revealed that the present wind-lens profile is suitable in both flood and ebb current flows.

Effect of blockage on ducted turbines

The advantage of blockage effect on the performance of tidal turbines has been studied extensively in the literature. The present report is the first analysis of blockage variation on asymmetric and symmetric ducted devices. The results provide evidence that ducted turbines generate higher power performance per rotor unit area instead of duct area. It also confirms the increase of peak power coefficients with blockage ratio and shows that the ratio of the peak power coefficient of ducted turbine over the peak power coefficient of bare turbine varies slightly with the blockage ratio.

Provision of useful design experimental data

Due to power augmentation associated with the ducted turbine, there exists an acute need for more experimental data to provide valuable information on the performance and wake characterisation of ducted tidal turbines. At present, there is limited availability of such experimental data. The originality of this study is that it is the first to experimentally explore duct performance and far wake characterisation of flanged duct turbines with an in-line arrangement. Thus, this study has provided a comprehensive set of experimental data to the research community that will guide the course of future marine current turbine research and suitable data for validating theoretical and numerical methods.

References

- Abe, K. I., & Ohya, Y. (2004). An investigation of flow fields around flanged diffusers using CFD. *Journal of Wind Engineering and Industrial Aerodynamics*, 92(3–4), 315–330. <https://doi.org/10.1016/j.jweia.2003.12.003>
- Abe, K., Nishida, M., Sakurai, A., Ohya, Y., Kihara, H., Wada, E., & Sato, K. (2005). Experimental and numerical investigations of flow fields behind a small wind turbine with a flanged diffuser. *Journal of Wind Engineering and Industrial Aerodynamics*, 93(12), 951–970. <https://doi.org/10.1016/j.jweia.2005.09.003>
- Abbott, I. H., & Doenhoff, A. E. (1959). Families of Wing Sections. *Theory of Wing Sections, Dover Publications, INC., New York*, 111-123.
- Adcock, T. A., & Draper, S. (2014). Power extraction from tidal channels—multiple tidal constituents, compound tides and overtides. *Renewable Energy*, 63, 797-806. <https://doi.org/10.1016/j.renene.2013.10.037>
- Al-Kayiem, H. H., & Bruun, H. H. (1991). Evaluation of a flying X hot-wire probe system. *Measurement Science and Technology*, 2(4), 374. <https://doi.org/10.1088/0957-0233/2/4/017>
- Allsop, S., Peyrard, C., Thies, P. R., Boulougouris, E., & Harrison, G. P. (2017). Hydrodynamic analysis of a ducted, open centre tidal stream turbine using blade element momentum theory. *Ocean Engineering*, 141, 531-542. <https://doi.org/10.1016/j.oceaneng.2017.06.040>
- Anderson Jr, John David. *Fundamentals of aerodynamics*. Tata McGraw-Hill Education, 2010.
- Apsley, D. D., & Leschziner, M. A. (2000). Advanced turbulence modelling of separated flow in a diffuser. *Flow, Turbulence and Combustion*, 63(1-4), 81. <https://doi.org/10.1023/A:1009930107544>
- Atlantis Resources Corporation. (2018). “Simec Atlantis Energy” Retrieved 11 December 2018 from <https://simecatlantis.com/services/turbines/>
- Badran, O. O., & Bruun, H. H. (2003, January). Turbulent flow over a NACA 4412 airfoil at angle of attack 15 degree. In *Fluids Engineering Division Summer Meeting* (Vol. 36975, pp. 137-141). <https://doi.org/10.1115/FEDSM2003-45610>
- Bahaj, A. S. (2013). Marine current energy conversion: the dawn of a new era in electricity production. *Phil Trans R Soc A371*: 20120500. <http://dx.doi.org/10.1098/rsta.2012.0500>
- Bahaj, A. S., Molland, A. F., Chaplin, J. R., & Batten, W. M. J. (2007a). Power and thrust measurements of marine current turbines under various hydrodynamic flow conditions in a cavitation tunnel and a towing tank. *Renewable energy*, 32(3), 407-426. <https://doi.org/10.1016/j.renene.2006.01.012>
- Bahaj, A. S., Myers, L. E., Thomson, M. D., & Jorge, N. (2007b, September). Characterising the wake of horizontal axis marine current turbines. In *Proceedings of the 7th European wave and tidal energy conference* (Vol. 9). University of Southampton Porto Portugal.

- Belloni, C. S. (2013). *Hydrodynamics of ducted and open-centre tidal turbines* (Doctoral dissertation, University of Oxford).
- Betz, A. (1920). Das Maximum der theoretisch möglichen Ausnutzung des Windes durch Windmotoren. *Zeitschrift für das gesamte Turbinenwesen*, 20.
- Betz, A. (1928). Windmills in the light of modern research, tech. rep., National Advisory Committee for Aeronautics, Washington, DC, p. 8.
- Blanco Ilzarbe, J. M., & Teixeira, J. A. (2009). Recent Patents on Tidal Power Extraction Devices. *Recent Patents on Engineering*, 3(3), 178-193. <https://doi.org/10.2174/187221209789117780>
- Bloomberg (2018a). Clean energy investment trends, 2Q 2018. Retrieve from <https://data.bloomberglp.com/bnef/sites/14/2018/07/BNEF-Clean-Energy-Investment-Trends-1H-2018.pdf>
- Bloomberg (2018b). Company Overview of Clean Current Power Systems Incorporated. Retrieved from <https://www.bloomberg.com/research/stocks/private/snapshots.asp?privcapId=45277781>
- Blue Energy International. (2018). Tidal Bridge Technology. Retrieve 11 December 2018 from <http://www.bluenergy.com/>
- Blunden, L. S., & Bahaj, A. S. (2007). Tidal energy resource assessment for tidal stream generators. *Proceedings of the Institution of Mechanical Engineers, Part A: Journal of Power and Energy*, 221(2), 137-146. <https://doi.org/10.1243/09576509JPE332>
- Borg, M. G., Xiao, Q., Allsop, S., Incecik, A., & Peyrard, C. (2020). A numerical performance analysis of a ducted, high-solidity tidal turbine. *Renewable Energy*, 159, 663-682. <https://doi.org/10.1109/oceanskobe.2018.8559233>
- Ceccotti, C., Spiga, A., Bartl, J., & Sætran, L. (2016). Effect of upstream turbine tip speed variations on downstream turbine performance. *Energy Procedia*, 94, 478-486. <https://doi.org/10.1016/j.egypro.2016.09.218>
- Celik, I. B., Ghia, U., Roache, P. J., & Freitas, C. J. (2008). Procedure for estimation and reporting of uncertainty due to discretization in CFD applications. *Journal of fluids Engineering-Transactions of the ASME*, 130(7). <https://doi.org/10.1115/1.2960953>
- Chamorro, L. P., Arndt, R. E. A., & Sotiropoulos, F. (2012). Reynolds number dependence of turbulence statistics in the wake of wind turbines. *Wind Energy*, 15(5), 733-742. <https://doi.org/10.1002/we.501>
- Chang, J. W. (2004). Near-wake characteristics of an oscillating NACA 4412 airfoil. *Journal of aircraft*, 41(5), 1240-1244. <https://doi.org/10.2514/1.6072>
- Chen, Y., Lin, B., Lin, J., & Wang, S. (2017). Experimental study of wake structure behind a horizontal axis tidal stream turbine. *Applied energy*, 196, 82-96. <https://doi.org/10.1016/j.apenergy.2017.03.126>

- Chen, Y., Lin, B., Sun, J., Guo, J., & Wu, W. (2019). Hydrodynamic effects of the ratio of rotor diameter to water depth: An experimental study. *Renewable Energy*, *136*, 331-341. <https://doi.org/10.1016/j.renene.2019.01.022>
- Clean Current Power Systems Incorporation (2013). “*Clean Energy*” Retrieved 11 December 2018 from <http://www.marinerenewables.ca/>; <http://www.cleancurrent.com>
- Cockrell, D. J., & Markland, E. (1963). A Review of Incompressible Diffuser Flow: A Reappraisal of an Article by GN Patterson entitled ‘Modern Diffuser Design’ which was published in this journal twenty-five years ago. *Aircraft Engineering and Aerospace Technology*. <https://doi.org/10.1108/eb033790>
- Consul, C. A., Willden, R. H. J., & McIntosh, S. C. (2013). Blockage effects on the hydrodynamic performance of a marine cross-flow turbine. *Philosophical Transactions of the Royal Society A: Mathematical, Physical and Engineering Sciences*, *371*(1985), 20120299. <https://doi.org/10.1098/rsta.2012.0299>
- Council, W. E. (2016). World energy resources 2016. *World Energy Council, London, UK*. Retrieve from <http://171.67.100.116/courses/2018/ph240/rogers2/docs/wec-2016.pdf>.
- Craig, R. G., Loadman, C., Clement, B., Rusello, P. J., & Siegel, E. (2011, March). Characterization and testing of a new bistatic profiling acoustic Doppler velocimeter: The Vectrino-II. In *2011 IEEE/OES 10th Current, Waves and Turbulence Measurements (CWTM)* (pp. 246-252). IEEE.
- Cresswell, N. W., Ingram, G. L., & Dominy, R. G. (2015). The impact of diffuser augmentation on a tidal stream turbine. *Ocean engineering*, *108*, 155-163. <https://doi.org/10.1016/j.oceaneng.2015.07.033>
- Davidson, P. (2015). *Turbulence: an introduction for scientists and engineers*. Oxford University Press
- Don P. (2009). Eu grant report by The Engineer. Retrieve from www.sdcommission.org.uk/data/files/publications/TidalPowerUK2-Tidal_technologies_overview.pdf.
- Duquette, M. M., Swanson, J., & Visser, K. D. (2003). Solidity and blade number effects on a fixed pitch, 50 W horizontal axis wind turbine. *Wind Engineering*, *27*(4), 299-316. <https://doi.org/10.1260/030952403322665271>
- Duquette, M. M., & Visser, K. D. (2003). Numerical implications of solidity and blade number on rotor performance of horizontal-axis wind turbines. *J. Sol. Energy Eng.*, *125*(4), 425-432. <https://doi.org/10.1115/1.1629751>
- Elemental Energy Technologies (2017). “*SeaUrchin Tidal Turbine*”. Retrieved 11 December 2018 from <https://www.rpctechnologies.com/renewableenergy>; <http://www.eettidal.com>
- El-Zahaby, A. M., Kabeel, A. E., Elsayed, S. S., & Obiaa, M. F. (2017). CFD analysis of flow fields for shrouded wind turbine’s diffuser model with different flange angles. *Alexandria Engineering Journal*, *56*(1), 171-179. <https://doi.org/10.1016/j.aej.2016.08.036>

- Engineering Business Ltd. (2005). Stingray tidal energy stream device - Phase 3, Report for DTI New and Renewable Energy Programme. Retrieve from https://tethys.pnnl.gov/sites/default/files/publications/Stingray_Tidal_Stream_Energy_Device.pdf
- Entec UK Ltd. (2007). Tidal technologies overview. Retrieve from http://www.sdcommission.org.uk/data/files/publications/TidalPowerUK2Tidal_technologies_overview.pdf
- Environmental Protection Department (2020). Greenhouse Gas Emissions in Hong Kong. Retrieve 21 December 2020 from <https://www.climateready.gov.hk/page.php?id=23&lang=1>.
- Eurobarometer, S. (2006). Energy Technologies: Knowledge, Perception, Measures.
- European Marine Energy Centre Ltd (2018a). Tidal developers. Retrieve 11 December 2018 from <http://www.emec.org.uk/marine-energy/tidal-developers/>
- European Marine Energy Centre Ltd (2018b). Tidal devices. Retrieve 12 December 2018 from <http://www.emec.org.uk/marine-energy/tidal-devices/>.
- European Marine Energy Centre Ltd (2018c). Atlantis resources corporation. Retrieve 11 December 2018 from <http://www.emec.org.uk/about-us/our-tidal-clients/atlantis-resources-corporation-2/>
- European Marine Energy Centre Ltd. (2018d). Retrieve 11 December 2018 from <http://www.emec.org.uk/>
- Fleming, C. F. (2011). Design and analysis of a bi-directional ducted tidal turbine. In *Proceedings of the 9th European Wave and Tidal Energy Conference, 2011*.
- Fleming, C. F., & Willden, R. H. (2016). Analysis of bi-directional ducted tidal turbine performance. *International journal of marine energy*, 16, 162-173. <https://doi.org/10.1016/j.ijome.2016.07.003>
- Frandsen, S., Trenka, A. R., & Maribo Pedersen, B. (1990). Recommended practices for wind turbine testing. 1. Power performance testing.
- Frau, J. P. (1993). Tidal energy: promising projects: La Rance, a successful industrial-scale experiment. *IEEE Transactions on Energy Conversion*, 8(3), 552-558. <https://doi.org/10.1109/60.257073>
- Frost, C., Morris, C. E., Mason-Jones, A., O'Doherty, D. M., & O'Doherty, T. (2015). The effect of tidal flow directionality on tidal turbine performance characteristics. *Renewable Energy*, 78, 609-620. <https://doi.org/10.1016/j.renene.2015.01.053>
- Funke, S. W., Kramer, S. C., & Piggott, M. D. (2016). Design optimisation and resource assessment for tidal-stream renewable energy farms using a new continuous turbine approach. *Renewable energy*, 99, 1046-1061. <https://doi.org/10.1016/j.renene.2016.07.039>

- Haque, M. N., Ali, M., & Ara, I. (2015). Experimental investigation on the performance of NACA 4412 aerofoil with curved leading-edge planform. *Procedia Engineering*, 105, 232-240. <https://doi.org/10.1016/j.proeng.2015.05.099>
- Hau, E. (2013). *Wind turbines: fundamentals, technologies, application, economics*. Springer Science & Business Media.
- Gaden, D. L., & Bibeau, E. L. (2010). A numerical investigation into the effect of diffusers on the performance of hydrokinetic turbines using a validated momentum source turbine model. *Renewable Energy*, 35(6), 1152-1158. <https://doi.org/10.1016/j.renene.2009.11.023>
- Garrett, C., & Cummins, P. (2007). The efficiency of a turbine in a tidal channel. *Journal of fluid mechanics*, 588, 243. <https://doi.org/10.1017/S0022112007007781>
- Geuzaine, C & Remacle, J.F. (2009). *Gmsh: a three-dimensional finite element mesh generator with built-in pre- and post-processing facilities*. *International Journal for Numerical Methods in Engineering* 79(11), pp. 1309-1331. <https://doi.org/10.1002/nme.2579>
- Gilbert, B. L., Oman, R. A., & Foreman, K. M. (1978). Fluid dynamics of diffuser-augmented wind turbines. *Journal of Energy*, 2(6), 368-374. <https://doi.org/10.2514/3.47988>
- Gilbert, B. L., & Foreman, K. M. (1979). Experimental demonstration of the diffuser-augmented wind turbine concept. *Journal of Energy*, 3(4), 235-240. <https://doi.org/10.2514/3.48002>
- Göltenbott, U., Ohya, Y., Yoshida, S., & Jamieson, P. (2017). Aerodynamic interaction of diffuser augmented wind turbines in multi-rotor systems. *Renewable Energy*, 112, 25-34. <https://doi.org/10.1016/j.renene.2017.05.014>
- Gorlov, A. M. (1995). *U.S. Patent No. 5,451,137*. Washington, DC: U.S. Patent and Trademark Office.
- Greenshields, C. J., & OpenFOAM, R. (2016). User Guide version 4.0. *OpenFOAM Foundation Ltd*.
- Guinard Energies (2017). “MEGAWATTBlue technology”. Retrieved 11 December 2018 from <https://www.guinard-energies.bzh/en/guinard-energies-2/>
- Guo, B., Wang, D., Zhou, X., Shi, W., & Jing, F. (2020). Performance evaluation of a tidal current turbine with bidirectional symmetrical foils. *Water*, 12(1), 22. <https://doi.org/10.3390/w12010022>
- Hansen, M. O. L., Sørensen, N. N., & Flay, R. G. J. (2000). Effect of placing a diffuser around a wind turbine. *Wind Energy: An International Journal for Progress and Applications in Wind Power Conversion Technology*, 3(4), 207-213. <https://doi.org/10.1002/we.37>
- Haque, M. N., Ali, M., & Ara, I. (2015). Experimental investigation on the performance of NACA 4412 aerofoil with curved leading edge planform. *Procedia Engineering*, 105, 232-240. <https://doi.org/10.1016/j.proeng.2015.05.099>
- Harrison, M. E., Batten, W. M. J., Myers, L. E., & Bahaj, A. S. (2010). Comparison between CFD simulations and experiments for predicting the far wake of horizontal axis tidal

- turbines. *IET Renewable Power Generation*, 4(6), 613-627. <https://doi.org/10.1049/iet-rpg.2009.0193>
- Hellsten, A. (1998). Some improvements in Menter's k-omega SST turbulence model. In *29th AIAA, Fluid Dynamics Conference* (p. 2554). <https://doi.org/10.2514/6.1998-2554>
- Houlsby, G. T., Draper, S., & Oldfield, M. L. G. (2008). Application of linear momentum actuator disc theory to open channel flow IEA. (2018). World energy outlook. Retrieved 11 December 2018 from <https://www.iea.org/reports/renewables-2018#>
- HydroHelix Energies (2014). "MHK Technologies/HydroHelix". Retrieved 11 December 2018 from https://openei.org/wiki/MHK_Technologies/Hydro_Helix; <https://hydrohelix.fr/>
- Igra, O. (1976). Shrouds for aerogenerators. *AIAA Journal*, 14(10), 1481-1483.
- Igra, O. (1981). Research and development for shrouded wind turbines. *Energy Conversion and Management*, 21(1), 13-48. [https://doi.org/10.1016/0196-8904\(81\)90005-4](https://doi.org/10.1016/0196-8904(81)90005-4)
- IPCC (2014). *Climate Change 2014: Mitigation of Climate Change. Contribution of Working Group III to the Fifth Assessment Report of the Intergovernmental Panel on Climate Change*, [Edenhofer, O., R. Pichs-Madruga, Y. Sokona, E. Farahani, S. Kadner, K. Seyboth, A. Adler, I. Baum, S. Brunner, P. Eickemeier, B. Kriemann, J. Savolainen, S. Schlömer, C. von Stechow, T. Zwickel and J.C. Minx (eds.)]. Cambridge University Press, Cambridge, United Kingdom and New York, NY, USA.
- Jamieson, P. (2008). Generalized limits for energy extraction in a linear constant velocity flow field. *Wind Energy: An International Journal for Progress and Applications in Wind Power Conversion Technology*, 11(5), 445-457. <https://doi.org/10.1002/we.268>
- Javaherchi, T., Stelzenmuller, N., & Aliseda, A. (2013, April). Experimental and numerical analysis of the doe reference model 1 horizontal axis hydrokinetic turbine. In *Proceedings. 1st Marine Energy Technology Symposium METS2013, Washington, DC*.
- Kardous, M., Chaker, R., Aloui, F., & Nasrallah, S. B. (2013). On the dependence of an empty flanged diffuser performance on flange height: Numerical simulations and PIV visualizations. *Renewable energy*, 56, 123-128. <https://doi.org/10.1016/j.renene.2012.09.061>
- Kofoed, J. P., Pecher, A., Margheritini, L., Holmes, B., McCombes, T., Johnstone, C., ... & Meyers, L. E. (2010). EquiMar: Equitable Testing and Evaluation of Marine Energy Extraction Devices in Terms of Performance, Cost and Environmental Impact: Deliverable D4. 2 Data Analysis & Presentation to Quantify Uncertainty.
- Kolekar, N., & Banerjee, A. (2015). Performance characterization and placement of a marine hydrokinetic turbine in a tidal channel under boundary proximity and blockage effects. *Applied Energy*, 148, 121-133. <https://doi.org/10.1016/j.apenergy.2015.03.052>
- Lawn, C. J. (2003). Optimization of the power output from ducted turbines. *Proceedings of the Institution of Mechanical Engineers, Part A: Journal of Power and Energy*, 217(1), 107-117. <https://doi.org/10.1243/095765003321148754>

- Lee, S. H., Lee, S. H., Jang, K., Lee, J., & Hur, N. (2010). A numerical study for the optimal arrangement of ocean current turbine generators in the ocean current power parks. *Current Applied Physics*, 10(2), S137-S141. <https://doi.org/10.1016/j.cap.2009.11.018>
- Lilley, G. M., & Rainbird, W. J. (1956). A preliminary report on the design and performance of ducted windmills Magagna, D., Monfardini, R., & Uihlein, A. (2016). JRC ocean energy status report 2016 edition. *Publications Office of the European Union: Luxembourg*.
- Limacher, E. J., da Silva, P. O., Barbosa, P. E., & Vaz, J. R. (2020). Large exit flanges in diffuser-augmented turbines lead to sub-optimal performance. *Journal of Wind Engineering and Industrial Aerodynamics*, 204, 104228. <https://doi.org/10.1016/j.jweia.2020.104228>
- Lin, J., Sun, J., Liu, L., Chen, Y., & Lin, B. (2015). Refined representation of turbines using a 3D SWE model for predicting distributions of velocity deficit and tidal energy density. *International journal of energy research*, 39(13), 1828-1842. <https://doi.org/10.1002/er.3333>
- Liu, J., Song, M., Chen, K., Wu, B., & Zhang, X. (2016). An optimization methodology for wind lens profile using computational fluid dynamics simulation. *energy*, 109, 602-611. <https://doi.org/10.1016/j.energy.2016.04.131>
- Liu, P., Bose, N., Frost, R., Macfarlane, G., Lilienthal, T., Penesis, I., ... & Thomas, G. (2014). Model testing of a series of bi-directional tidal turbine rotors. *Energy*, 67, 397-410. <https://doi.org/10.1016/j.energy.2013.12.058>
- Liu, Q., Gómez, F., Perez, J. M., & Theofilis, V. (2016). Instability and sensitivity analysis of flows using OpenFOAM®. *Chinese Journal of Aeronautics*, 29(2), 316-325. <https://doi.org/10.1016/j.cja.2016.02.012>
- Lunar Energy Tidal Power (2006). “*Lunar Energy Limited*”. Retrieve 12 December 2018 from <http://www.reuk.co.uk/wordpress/tidal/lunar-energy-tidal-power/>; <http://www.lunarenergy.co.uk>
- Luquet, R., Bellevre, D., Fréchou, D., Perdon, P., & Guinard, P. (2013). Design and model testing of an optimized ducted marine current turbine. *International journal of marine energy*, 2, 61-80. <https://doi.org/10.1016/j.ijome.2013.05.009>
- Lysenko, D. A., Ertesvåg, I. S., & Rian, K. E. (2013). Modeling of turbulent separated flows using OpenFOAM. *Computers & Fluids*, 80, 408-422. <https://doi.org/10.1016/j.compfluid.2012.01.015>
- Magagna, D., Monfardini, R., & Uihlein, A. (2016). JRC ocean energy status report 2016 edition. *Publications Office of the European Union: Luxembourg*.
- Maganga, F., Germain, G., King, J., Pinon, G., & Rivoalen, E. (2010). Experimental characterisation of flow effects on marine current turbine behaviour and on its wake properties. *IET Renewable Power Generation*, 4(6), 498-509. <https://doi.org/10.1049/iet-rpg.2009.0205>

- Malki, R., Masters, I., Williams, A. J., & Croft, T. N. (2014). Planning tidal stream turbine array layouts using a coupled blade element momentum–computational fluid dynamics model. *Renewable Energy*, 63, 46-54. <https://doi.org/10.1016/j.renene.2013.08.039>
- Mansour, K., & Meskinkhoda, P. (2014). Computational analysis of flow fields around flanged diffusers. *Journal of Wind Engineering and Industrial Aerodynamics*, 124, 109-120. <https://doi.org/10.1016/j.jweia.2013.10.012>
- Marine Renewables Canada (2018). State of the Sector Report, June 2018. Retrieve from <https://tethys.pnnl.gov/sites/default/files/publications/MRC-State-of-the-Sector-2018.pdf>
- McDonald, A. T., & Fox, R. W. (1966). An experimental investigation of incompressible flow in conical diffusers. *International Journal of Mechanical Sciences*, 8(2), 125-139. [https://doi.org/10.1016/0020-7403\(66\)90071-3](https://doi.org/10.1016/0020-7403(66)90071-3)
- McIntosh, S. C., Fleming, C. F., & Willden, R. H. (2011). Embedded RANS-BEM tidal turbine design. In *Proceedings of the 9th European wave and tidal energy conference, Southampton*
- Meher-Homji, C. B. (2000). The Historical Evolution of Turbomachinery. In *Proceedings of the 29th Turbomachinery Symposium*. Texas A&M University. Turbomachinery Laboratories. <https://doi.org/10.21423/R1X948>
- Menter, F. R. (1994). Two-equation eddy-viscosity turbulence models for engineering applications. *AIAA journal*, 32(8), 1598-1605. <https://doi.org/10.2514/3.12149>
- Menter, F. R., Kuntz, M., & Langtry, R. (2003). Ten years of industrial experience with the SST turbulence model. *Turbulence, heat and mass transfer*, 4(1), 625-632.
- Meyers, L. E., & Bahaj, A. S. (2010). Experimental analysis of the flow field around horizontal axis tidal turbines by use of scale mesh disk rotor simulator. *Ocean Eng*, 37(218), e27. <https://doi.org/10.1016/j.oceaneng.2009.11.004>
- Mitigation, C. C. (2011). IPCC special report on renewable energy sources and climate change mitigation. *Renewable Energy*, 20(11).
- Munch, C., Vonlanthen, M., Gomes, J., Luquet, R., Guinard, P., & Avellan, F. (2009, October). Design and performance assessment of a tidal ducted turbine. In *Proceedings of the third IAHR International Meeting of the Workgroup on Cavitation and Dynamic Problems in Hydraulic Machinery and Systems, Brno, Czech Republic* (pp. 571-581).
- Mycek, P., Gaurier, B., Germain, G., Pinon, G., & Rivoalen, E. (2014). Experimental study of the turbulence intensity effects on marine current turbines behaviour. Part I: One single turbine. *Renewable Energy*, 66, 729-746. <https://doi.org/10.1016/j.renene.2013.12.036>
- Myers, L., & Bahaj, A. S. (2009, September). Near wake properties of horizontal axis marine current turbines. In *Proceedings of the 8th European wave and tidal energy conference* (pp. 558-565). Uppsala, Sweden
- Myers, L. E., & Bahaj, A. S. (2010). Experimental analysis of the flow field around horizontal axis tidal turbines by use of scale mesh disk rotor simulators. *Ocean engineering*, 37(2-3), 218-227. <https://doi.org/10.1016/j.oceaneng.2009.11.004>

- Myers, L. E., & Bahaj, A. S. (2012). An experimental investigation simulating flow effects in first generation marine current energy converter arrays. *Renewable Energy*, 37(1), 28-36. <https://doi.org/10.1016/j.renene.2011.03.043>
- Myers, L., Bahaj, A. S., Germain, G., & Giles, J. (2008a, January). Flow boundary interaction effects for marine current energy conversion devices. In *World Renewable Energy Congress X, Glasgow, Juillet 2008*.
- Myers, L. E., Bahaj, A. S., Rawlinson-Smith, R. I., & Thomson, M. (2008b, January). The effect of boundary proximity upon the wake structure of horizontal axis marine current turbines. In *International Conference on Offshore Mechanics and Arctic Engineering* (Vol. 48234, pp. 709-719). <https://doi.org/10.1115/OMAE2008-57667>
- Nakayama, A. (1985). Characteristics of the flow around conventional and supercritical airfoils. *J. Fluid Mech*, 160, 155-179. <https://doi.org/10.1017/S0022112085003433>
- Nash, S., Olbert, A. I., & Hartnett, M. (2015). Towards a low-cost modelling system for optimising the layout of tidal turbine arrays. *Energies*, 8(12), 13521-13539. <https://doi.org/10.3390/en81212380>
- Nedyalkov, I., & Wosnik, M. (2014, August). Performance of bi-directional blades for tidal current turbines. In *Fluids Engineering Division Summer Meeting* (Vol. 46230, p. V01CT16A013). American Society of Mechanical Engineers. <https://doi.org/10.1115/FEDSM2014-21716>
- Nieto, F., Hargreaves, D. M., Owen, J. S., & Hernández, S. (2015). On the applicability of 2D URANS and SST k- ω turbulence model to the fluid-structure interaction of rectangular cylinders. *Engineering Applications of Computational Fluid Mechanics*, 9(1), 157-173. <https://doi.org/10.1080/19942060.2015.1004817>
- Nishino, T., & Willden, R. H. (2012a). The efficiency of an array of tidal turbines partially blocking a wide channel. *Journal of Fluid Mechanics*, 708, 596. <https://doi.org/10.1017/jfm.2012.349>
- Nishino, T., & Willden, R. H. (2012b). Effects of 3-D channel blockage and turbulent wake mixing on the limit of power extraction by tidal turbines. *International Journal of Heat and Fluid Flow*, 37, 123-135. <https://doi.org/10.1016/j.ijheatfluidflow.2012.05.002>
- Ocean Renewable Power Company (2018). TidGen Power System. Retrieve 11 December 2018 from http://www.orpc.co/orpcpowersystem_tidgenpowersystem.aspx
- Ohya, Y., Karasudani, T., Sakurai, A., Abe, K. I., & Inoue, M. (2008). Development of a shrouded wind turbine with a flanged diffuser. *Journal of wind engineering and industrial aerodynamics*, 96(5), 524-539. <https://doi.org/10.1016/j.jweia.2008.01.006>
- Ohya, Y., Uchida, T., Karasudani, T., Hasegawa, M., & Kume, H. (2012). Numerical studies of flow around a wind turbine equipped with a flanged-diffuser shroud using an actuator-disk model. *Wind Engineering*, 36(4), 455-472. <https://doi.org/10.1260/0309-524X.36.4.455>

- Okulov, V. L., & Van Kuik, G. A. (2012). The Betz–Joukowsky limit: on the contribution to rotor aerodynamics by the British, German, and Russian scientific schools. *Wind Energy*, 15(2), 335-344. <https://doi.org/10.1002/we.464>
- OpenHydro Ltd (2018). “*Open Hydro*” Retrieved 12 December 2018 from <http://www.emec.org.uk/about-us/our-tidal-clients/open-hydro/>; www.openhydro.com/
- Park, Y. M., Chang, B. H., & Cho, T. H. (2007). Numerical simulation of wind turbine scale effects by using CFD. In *45th AIAA aerospace sciences meeting and exhibit* (p. 216). <https://doi.org/10.2514/6.2007-216>
- Phillips, D. G. (2003). *An investigation on diffuser augmented wind turbine design* (Doctoral dissertation, ResearchSpace@ Auckland).
- Phillips, D. G., Flay, R. G. J., & Nash, T. A. (1999). Aerodynamic analysis and monitoring of the Vortec 7 diffuser-augmented wind turbine. *Transactions of the Institution of Professional Engineers New Zealand: Electrical/Mechanical/Chemical Engineering Section*, 26(1), 13.
- Phillips, D. G., Richards, P. J., & Flay, R. G. J. (2008). Diffuser development for a diffuser augmented wind turbine using computational fluid dynamics. *Department of Mechanical, Engineering, the University of Auckland, New Zealand*.
- Pinkerton, R. M. (1938). *The variation with Reynolds number of pressure distribution over an airfoil section*. US Government Printing Office.
- Polagye, B., Copping, A., Kirkendall, K., Boehlert, G., Walker, S., Wainstein, M., & Van Cleve, B. (2010). Environmental effects of tidal energy development: a scientific workshop. *University of Washington, Seattle, Seattle, WA, USA, NMFS F/SPO-116, NOAA*.
- Ponte di Archimede S.p.A. (2018). The Kobold Turbine. Retrieve 11 December 2018 from <http://www.seapowerscrl.com/ocean-and-river-system/kobold/>
- Rahman, A., Venugopal, V., & Thiebot, J. (2018). On the Accuracy of Three-Dimensional Actuator Disc Approach in Modelling a Large-Scale Tidal Turbine in a Simple Channel. *Energies*, 11(8), 2151. <https://doi.org/10.3390/en11082151>
- Rancourt, D., Tabesh, A., & Fréchette, L. G. (2007). Evaluation of centimeter-scale micro windmills: aerodynamics and electromagnetic power generation. *Proc. PowerMEMS, 20079*, 93-96.
- REN21, R. (2018). *Global Status Report, REN21 Secretariat, Paris*. France. Tech. Rep.
- Robertson, E., Choudhury, V., Bhushan, S., & Walters, D. K. (2015). Validation of OpenFOAM numerical methods and turbulence models for incompressible bluff body flows. *Computers & Fluids*, 123, 122-145. <https://doi.org/10.1016/j.compfluid.2015.09.010>
- Rourke, F. O., Boyle, F., & Reynolds, A. (2010). Tidal energy update 2009. *Applied energy*, 87(2), 398-409. <https://doi.org/10.1016/j.apenergy.2009.08.014>

- Ross, H., & Polagye, B. (2020). An experimental assessment of analytical blockage corrections for turbines. *Renewable Energy*, 152, 1328-1341. <https://doi.org/10.1016/j.renene.2020.01.135>
- Sakaguchi, D., & Kyojuka, Y. (2018). Design of shrouded tidal current turbine by multi-objective optimization. In *International Conference of grand renewable energy 2018 Proceeding, Japan*.
- Sanderse, B. (2009). Aerodynamics of wind turbine wakes-literature review.
- Senior, J., Wiemann, P., & Muller, G. (2008). The rotary hydraulic pressure machine for very low head hydropower sites. *Proc. Hydroenergia*
- Setoguchi, T., Shiomi, N., & Kaneko, K. (2004). Development of two-way diffuser for fluid energy conversion system. *Renewable Energy*, 29(10), 1757-1771. <https://doi.org/10.1016/j.renene.2004.02.007>
- Shaaban, S., & Hafiz, A. A. (2012). Effect of duct geometry on Wells turbine performance. *Energy conversion and management*, 61, 51-58. <https://doi.org/10.1016/j.enconman.2012.03.023>
- Shives, M. R. (2011). *Hydrodynamic modeling, optimization and performance assessment for ducted and non-ducted tidal turbines* (Doctoral dissertation). <http://hdl.handle.net/1828/3801>
- Shives, M., & Crawford, C. (2010, September). Overall efficiency of ducted tidal current turbines. In *OCEANS 2010 MTS/IEEE SEATTLE* (pp. 1-6). IEEE. <https://doi.org/10.1109/OCEANS.2010.5664426>
- Shives, M., & Crawford, C. (2011). Developing an empirical model for ducted tidal turbine performance using numerical simulation results. *Proceedings of the Institution of Mechanical Engineers, Part A: Journal of Power and Energy*, 226(1), 112-125. <https://doi.org/10.1177/0957650911417958>
- Sivasegaram, S. (1986). Power Augmentation in Wind Rotors: A Review. *Wind Engineering*, 10(3), 163-179. <http://www.jstor.org/stable/43749280>
- Su, X., Zhang, H., Zhao, G., Cao, Y., & Zhao, Y. (2018). Numerical and experimental investigations on the hydrodynamic performance of a tidal current turbine. *Journal of Offshore Mechanics and Arctic Engineering*, 140(2). <https://doi.org/10.1115/1.4038249>
- Sun, H., & Kyojuka, Y. (2012). Experimental validation and numerical simulation evaluation of a shrouded tidal current turbine. *Journal of the Japan Society of Naval Architects and Ocean Engineers*, 16, 25-32. <https://doi.org/10.2534/jjasnaoe.16.25>
- Sun, D., Owen, J. S., & Wright, N. G. (2009). Application of the k- ω turbulence model for a wind-induced vibration study of 2D bluff bodies. *Journal of Wind Engineering and Industrial Aerodynamics*, 97(2), 77-87. <https://doi.org/10.1016/j.jweia.2008.08.002>
- Stallard, T., Collings, R., Feng, T., & Whelan, J. (2013). Interactions between tidal turbine wakes: experimental study of a group of three-bladed rotors. *Philosophical Transactions*

- of the Royal Society A: *Mathematical, Physical and Engineering Sciences*, 371(1985), 20120159. <https://doi.org/10.1098/rsta.2012.0159>
- Stringer, R. M., Zang, J., & Hillis, A. J. (2014). Unsteady RANS computations of flow around a circular cylinder for a wide range of Reynolds numbers. *Ocean Engineering*, 87, 1-9. <https://doi.org/10.1016/j.oceaneng.2014.04.017>
- Tangler, J. (2000). *The evolution of rotor and blade design* (No. NREL/CP-500-28410). National Renewable Energy Lab., Golden, CO (US).
- Taylor, B. N., & Kuyatt, C. E. (1994). Guidelines for evaluating and expressing the uncertainty of NIST measurement results.
- Tedds, S. C., Owen, I., & Poole, R. J. (2014). Near-wake characteristics of a model horizontal axis tidal stream turbine. *Renewable Energy*, 63, 222-235. <https://doi.org/10.1016/j.renene.2013.09.011>
- Thomas, R. E., Schindfessel, L., McLelland, S. J., Creëlle, S., & De Mulder, T. (2017). Bias in mean velocities and noise in variances and covariances measured using a multistatic acoustic profiler: The Nortek Vectrino Profiler. *Measurement science and technology*, 28(7), 075302. <https://doi.org/10.1088/1361-6501/aa7273>
- Turnock, S. R., Phillips, A. B., Banks, J., & Nicholls-Lee, R. (2011). Modelling tidal current turbine wakes using a coupled RANS-BEMT approach as a tool for analyzing power capture of arrays of turbines. *Ocean Engineering*, 38(11-12), 1300-1307. <https://doi.org/10.1016/j.oceaneng.2011.05.018>
- UEK Corporation (2014). “*Underwater Electric Kite Turbine*”. Retrieved 12 December 2018 from https://openei.org/wiki/MHK_Technologies/Underwater_Electric_Kite_Turbine; <http://www.uekus.com>
- UNFCCC, O. (2020). Paris Agreement-Status of Ratification. Retrieved on, December 21, 2020.
- Van Bussel, G. (1998). Power augmentation principles for wind turbines. *Delft University of Technology*.
- Van Bussel, G. J. (2007). The science of making more torque from wind: Diffuser experiments and theory revisited. In *Journal of Physics: Conference Series*, 75 (1). IOP.
- Vardar, A., & Alibas, I. (2008). Research on wind turbine rotor models using NACA profiles. *Renewable Energy*, 33(7), 1721-1732. <https://doi.org/10.1016/j.renene.2007.07.009>
- Vennell, R., Funke, S. W., Draper, S., Stevens, C., & Divett, T. (2015). Designing large arrays of tidal turbines: A synthesis and review. *Renewable and Sustainable Energy Reviews*, 41, 454-472. <https://doi.org/10.1016/j.rser.2014.08.022>
- Voith Hydropower (2018). Tidal current power stations. Retrieve 11 December 2018 from <http://www.voith.com/en/products-services/hydro-power/ocean-energies/tidal-current-power-stations-591.html>
- Vries, O. D. (1979). *Fluid dynamic aspects of wind energy conversion*. Advisory Group for Aerospace Research and Development NEUILLY-SUR-SEINE (France).

- Wadcock, A. J. (1978). *Flying-hot-wire study of two-dimensional turbulent separation of an NACA 4412 airfoil at maximum lift* (Doctoral dissertation, California Institute of Technology).
- Watson, S., Moro, A., Reis, V., Baniotopoulos, C., Barth, S., Bartoli, G., ... & Wiser, R. (2019). Future emerging technologies in the wind power sector: A European perspective. *Renewable and Sustainable Energy Reviews*, *113*, 109270. <https://doi.org/10.1016/j.rser.2019.109270>
- Wendt, J. F., ed. (2009). *Computational Fluid Dynamics*. 3rd ed., Springer-Verlag Berlin Heidelberg.
- Wenehenubun, F., Saputra, A., & Sutanto, H. (2015). An experimental study on the performance of Savonius wind turbines related with the number of blades. *Energy procedia*, *68*, 297-304. <https://doi.org/10.1016/j.egypro.2015.03.259>
- Whelan, J. I., Graham, J. M. R., & Peiró, J. (2009). A free-surface and blockage correction for tidal turbines. *Journal of Fluid Mechanics*, *624*, 281. <https://doi.org/10.1017/S002211200900591>
- Wilcox, D. C. (1998). *Turbulence modeling for CFD* (Vol. 2, pp. 103-217). La Canada, CA: DCW industries.
- World Energy Council (2016). World energy resources. Marine energy 2016. Retrieved From https://www.worldenergy.org/wpcontent/uploads/2017/03/WEResources_Marine_2016.pdf
- Yigit, C. (2020). Effect of Air-Ducted Blade Design on Horizontal Axis Wind Turbine Performance. *Energies*, *13*(14), 3618. <https://doi.org/10.3390/en13143618>
- Zang, W., Zheng, Y., Zhang, Y., Zhang, J., & Fernandez-Rodriguez, E. (2019). Experiments on the mean and integral characteristics of tidal turbine wake in the linear waves propagating with the current. *Ocean Engineering*, *173*, 1-11. <https://doi.org/10.1016/j.oceaneng.2018.12.048>